Universität Bonn

Physikalisches Institut

Diamond and Silicon Pixel Detectors in High Radiation Environments

Jieh-Wen Tsung

Diamond pixel detector is a promising candidate for tracking of collider experiments because of the good radiation tolerance of diamond. The diamond pixel detector must withstand the radiation damage from 10^{16} particles per cm^2, which is the expected total fluence in High Luminosity Large Hadron Collider. The performance of diamond and silicon pixel detectors are evaluated in this research in terms of the signal-to-noise ratio (SNR). Single-crystal diamond pixel detectors with the most recent readout chip ATLAS FE-I4 are produced and characterized. Based on the results of the measurement, the SNR of diamond pixel detector is evaluated as a function of radiation fluence, and compared to that of planar-silicon ones. The deterioration of signal due to radiation damage is formulated using the mean free path of charge carriers in the sensor. The noise from the pixel readout circuit is simulated and calculated with leakage current and input capacitance to the amplifier as important parameters. The measured SNR shows good agreement with the calculated and simulated results, proving that the performance of diamond pixel detectors can exceed the silicon ones if the particle fluence is more than 10^{15} particles per cm^2.

Physikalisches Institut der
Universität Bonn
Nußallee 12
D-53115 Bonn

BONN-IR-2012-05
Oct 2012
ISSN-0172-8741

Universität Bonn

Physikalisches Institut

Diamond and Silicon Pixel Detectors in High Radiation Environments

Jieh-Wen Tsung

Dieser Forschungsbericht wurde als Dissertation von der Mathematisch-Naturwissenschaftlichen Fakultät der Universität Bonn angenommen und ist auf der ULB Bonn `http://hss.ulb.uni-bonn.de/diss_online` elektronisch publiziert.

1. Gutachter:	Prof. Dr. Norbert Wermes
2. Gutachterin:	Prof. Dr. Andreas Zilges
Angenommen am:	15.08.2012
Tag der Promotion:	12.10.2012

Contents

Chapter 1

Introduction

The goal of this thesis is to evaluate the radiation tolerance of diamond and silicon (Si) pixel detectors which are designed for tracking in Large Hadron Collider (LHC) experiments.

LHC is the largest particle accelerator in the world. The accelerator of LHC is designed to collide two proton beams, each of them with 7 TeV of energy, giving a total center of mass energy of 14 TeV, which is the highest colliding energy that can be reached so far. The high colliding energy helps the scientists to explore the fundamental physical interactions in the early universe after the Big Bang.

The Standard Model of particle physics is so far the successful theory to describe the fundamental interactions. In the scope of Standard Model, the matter is constructed by leptons and quarks, and there are four kinds of fundamental forces: electromagnetic force, strong force, weak force, and gravity. Since the mid 1970s, the discovery of quarks and massive Z and W bosons for weak interaction confirmed the prediction of the Standard Model. However, there are still open questions of the Standard Model, such as the origin of mass, the dark matter, and the dark energy observed in the universe. Moreover, physicists are still searching for the "Grand Unification" – they believe that there is only one building block and one force for everything. To achieve the Grand Unification, physics beyond the Standard Model, such as supersymmetry and string theory have been proposed. All of these theories predict new interactions or free parameters that need to be measured by the LHC experiments.

ATLAS (A Toroidal LHC Apparatus) is one of the general purpose detectors for the LHC experiments. The detector records the tracks and measures the energy of the particles scattered from the collision, so the particles can be identified and the interaction can be reconstructed. The innermost sub-detector is the pixel detector to reconstruct the vertex of particle production or decay. The pixel detectors are in few centimeters vicinity to the beam pipe, so they must have strong radiation tolerance to withstand the damage by the radiation. Moreover, the luminosity of LHC is expected to increase by a factor of 10 in the 2020s, which is called the High Luminosity Large Hadron Collider (HL-LHC). Therefore, the pixel detectors with higher radiation-hardness are in demand.

New sensor materials and pixel readout techniques were imposed for the coming luminosity upgrade. While the data rate can be handled by microelectronics, sensors with higher radiation tolerance are also required. Diamond is a promising choice instead of the well-understood planar-Si sensors, mainly because of its higher displacement energy of the atoms in the lattice, and other properties that benefit the pixel readout technique, such as negligible leakage current and small capacitance which results in low electronic noise, long radiation length that leads to small material budget, high carrier mobility for fast signal collection, and extraordinary thermal conductivity leading to easier cooling for the detector system. The applicability of diamond pixel detector for particle detection and its performance after harsh radiation damage are very

interesting for the collider experiments of the next generation.

The performance of diamond pixel detector must be compared to the Si one. The Si pixel detector has large signal and noise level which is similar to the diamond one before irradiation. However, the noise of Si pixel increases with respect to the irradiation, while the diamond has the advantage that its noise is unaffected by the radiation damage. For both diamond and Si, the signal decreases versus the radiation damage, and the change of the signal charge must be measured using the same operational conditions and then compared to each other. For a fair comparison, the Signal-to-Noise Ratio (SNR) is chosen to be the figure-of-merit.

The goal of this thesis is to determine the SNR of diamond and Si pixel detectors in the HL-LHC environment. This is done by characterizing the pixel detector modules before and after irradiation, and evaluating the development of signal and noise with respect to the radiation damage based on the experimental results. This thesis starts from a brief introduction of LHC and the ATLAS experiment, see chapter 2. The basic concepts of production and operation of hybrid pixel detector are summarized in chapter 3, and the properties of diamond and Si are also compared in this chapter. The process of this research is shown graphically in the flowchart, fig. 1.1. The experimental bases of the entire research is explained in chapter 4. The diamond pixel detectors were produced and characterized before and after irradiation. The experimental methods and results are explained in detail in this chapter. The results of the characterization provide the references for the latter calculation and simulations. For the signal part, the generation of signals by the particle which passes through matter is described in chapter 5. Then the deterioration of signals with respect to the radiation damage is measured using diamond pad detectors, formulated for further predictions, and compared to that of Si, as shown in chapter 6. For the noise part, the noise of a pixel readout electronics were either analytically calculated or simulated. Also, the important parameters for noise modeling, such as input capacitance to the amplifier and leakage current were determined by measurements and calculation. These studies are presented in chapter 7. Applying the investigations on signal and noise, the SNR of diamond and Si pixel detectors are estimated as a function of radiation fluence, and the result is shown in chapter 8. Also, the efficiency and fake probability of pixel detectors in high radiation environments are evaluated based on the previous results. Finally, chapter 9 summarizes the important achievement of this research and the outlook for further investigations.

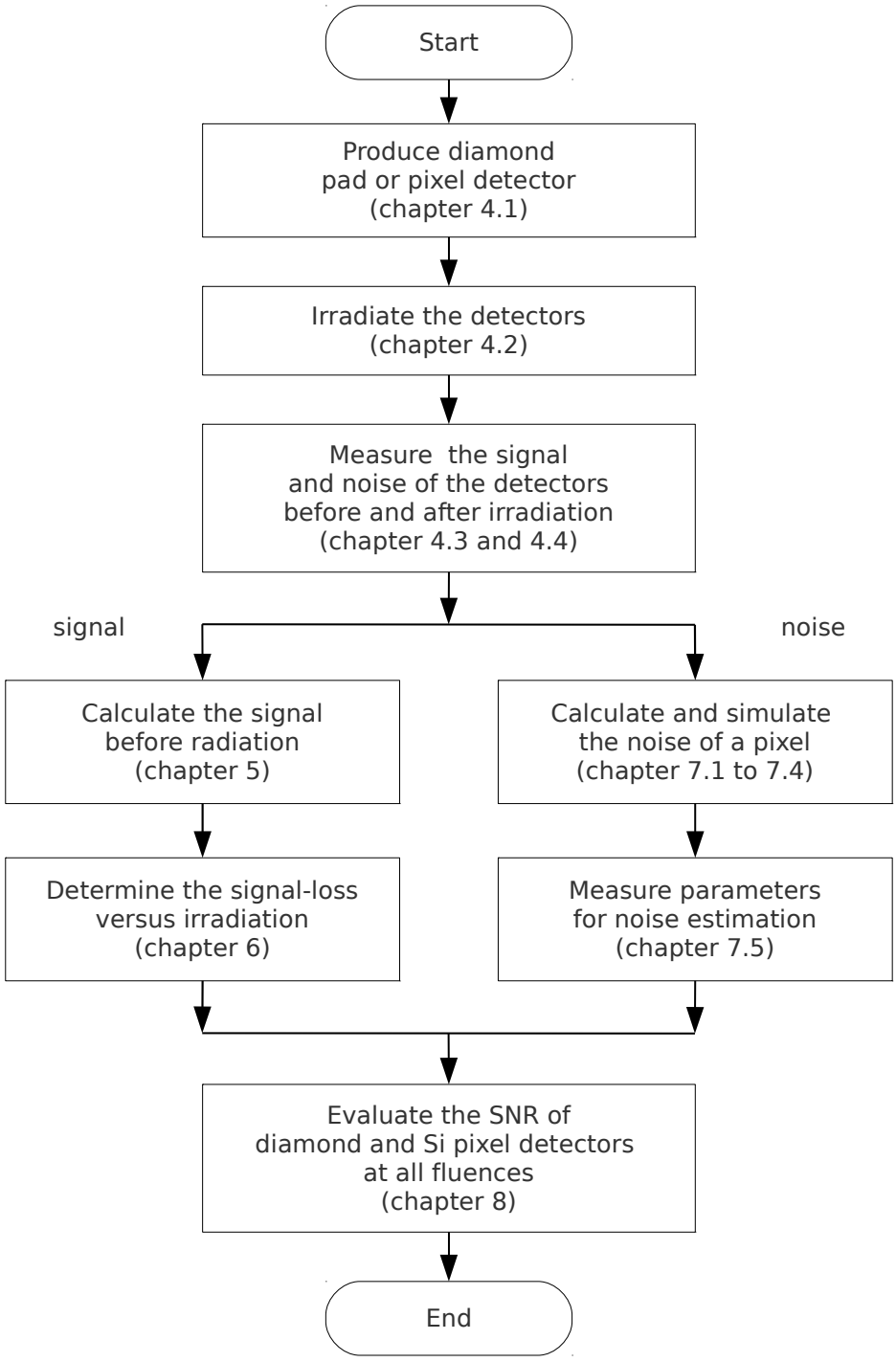

Figure 1.1: Flowchart of this thesis, showing the topics and the process of our investigation.

Chapter 2

The Large Hadron Collider and the ATLAS detector

2.1 Large Hadron Collider

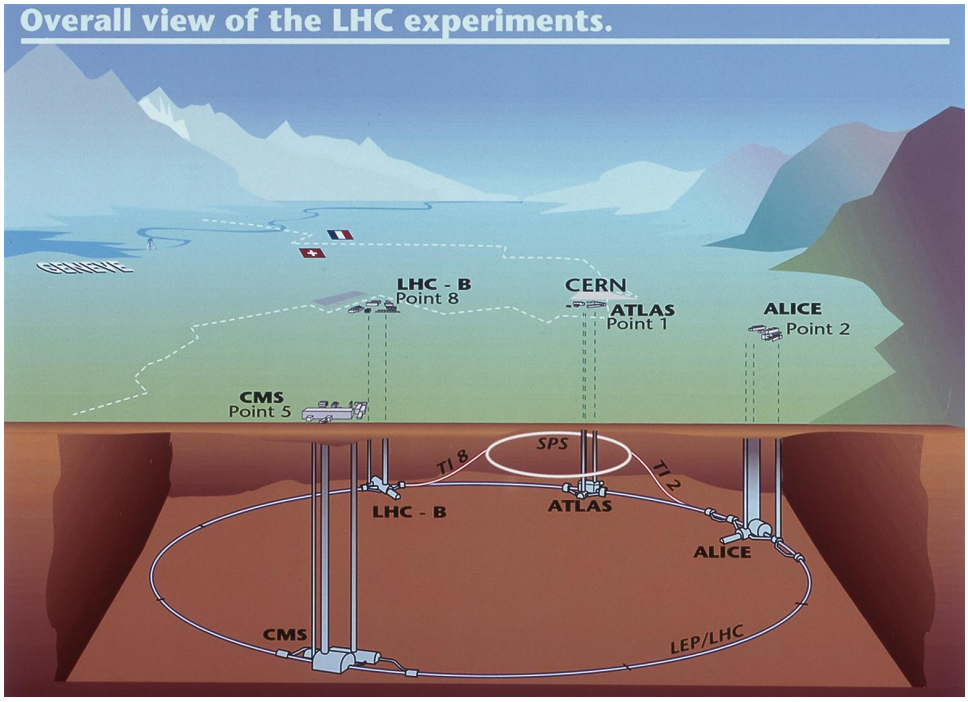

Figure 2.1: Sketch of the LHC ring, the position of the experiments and the surrounding countryside. The four big LHC experiments are indicated. The location of the injection lines and the SPS are also shown [1].

The Large Hadron Collider (LHC) [2] is a proton-proton collider at the European Organization for Nuclear Research in Geneva, Switzerland. The two proton beams are accelerated in opposite directions in a underground circular tunnel of 27 km circumference, about 100 m deep below the surface (see fig. 2.1). It has been operated since November 2009, and up to November, 2011, 5.57 fb^{-1} of collisions have been delivered by LHC.

The purpose of LHC experiments is to explore the physics in the TeV range, such as the Higgs boson of the standard model to explain the origin of mass, physics beyond the Standard Model such as supersymmetry which allows unification of the weak interactions, the strong interactions and electromagnetism at high energy, or the evidence of extra space-time dimen-

sions.

The proton bunches are accelerated in two separate vacuum pipes in opposite directions, guided by superconducting magnets with 8 T of magnetic field strength, and then they are brought to collide at the four collision points. Bunch Crossing happens every 25 ns. The target energy of the protons is 7 TeV, so the maximum center of mass energy is 14 TeV. The design peak luminosity of the LHC is 10^{34} cm^{-2} s^{-1}. During the life time of LHC, the expected integrated luminosity is from 80 fb^{-1} to 120 fb^{-1} per year [2].

The detectors record the track, and measure the momenta and the energy of the particles from the collision. From these information, the particle types can be identified, and the interactions during the collision can be reconstructed. Two detectors among the four, ATLAS [3] and CMS [4], are general purpose detectors designed for physics within and beyond the standard model. LHCb [5] focuses on the physics of b-quarks to investigate CP-violation. ALICE [6] is for heavy ion collision experiments, since LHC is also able to accelerate lead ions to 574 TeV.

2.2 ATLAS

The purpose of ATLAS is to measure the path, the momentum, and the energy of the particles to identify them, as illustrated in fig. 2.3. Based on these measurements the interaction during th proton-proton collision can be reconstrcted. Fig. 2.2 shows the sub-detectors in ATLAS. The most crucial detectors: trackers, calorimeters, muon detectors, and trigger systems will be briefly introduced below.

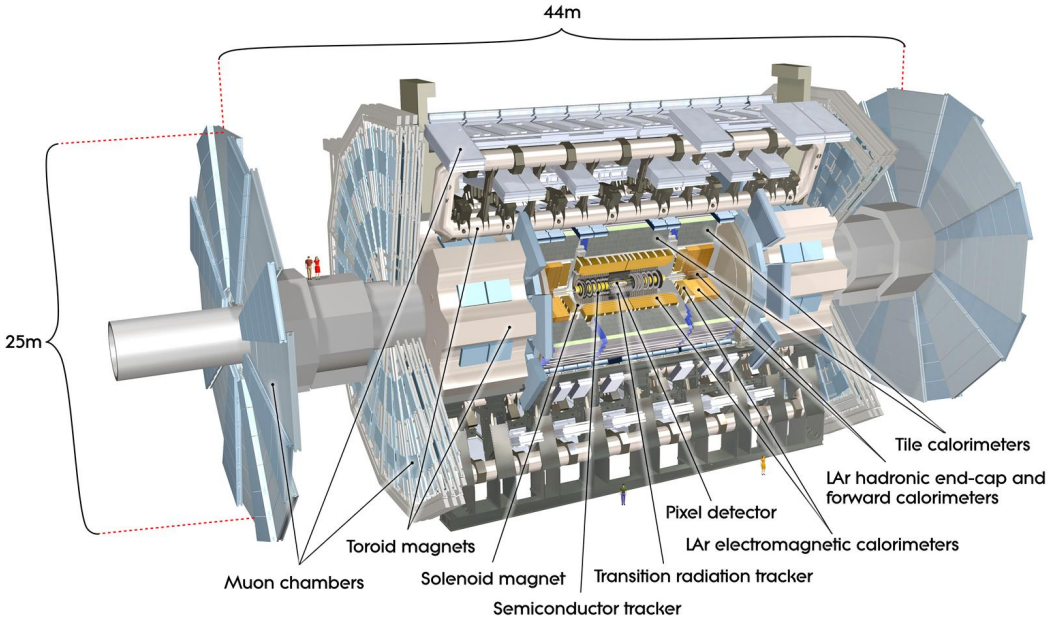

Figure 2.2: ATLAS general purpose detector, a cross section of ATLAS barrel part [1].

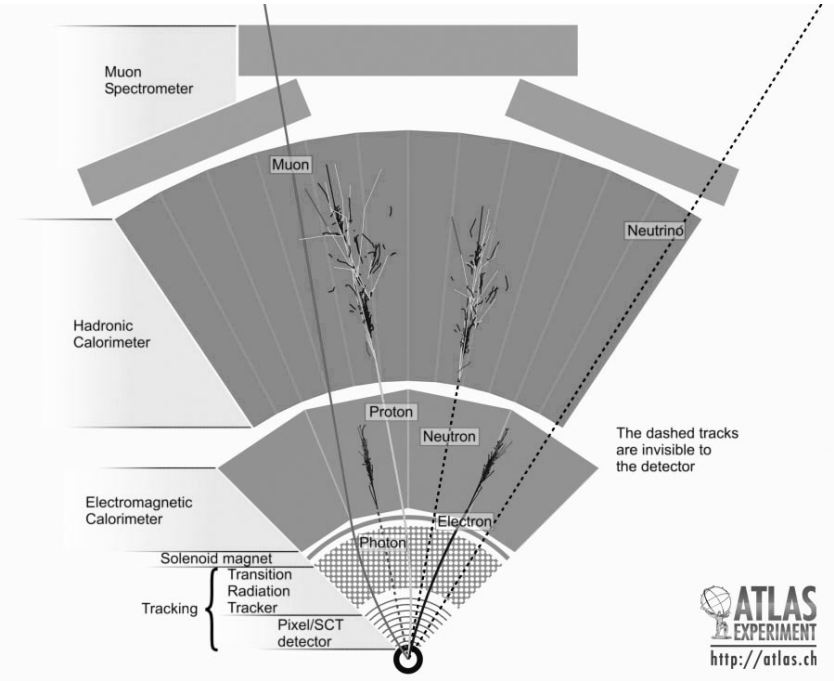

Figure 2.3: A cross section of the ATLAS detector and the signals generated by various types of particles [1].

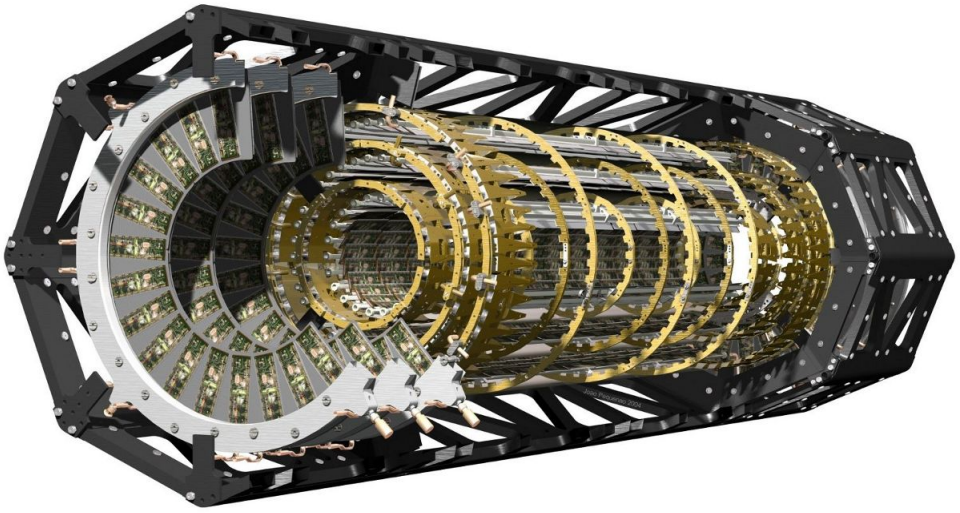

Figure 2.4: A 3D schematic of ATLAS pixel detector, shows barrels and discs [1].

Pixel detectors

The pixel detector [7] is the inner most detector of ATLAS, which is closest to the interaction point. The main mission of the pixel detector is to provide high granularity, high precision set of measurements of tracks to reconstruct the impact parameter and vertices of particle production or decay.

The structure of the ATLAS pixel detector is shown in fig. 2.4. It is composed of three barrel layers covering the interaction area at radii of 50.5 mm, 88.5 mm and 122.5 mm, and three disks at each end cap, covering the forward regions. The basic building block of the pixel detector is the hybrid pixel module made of bump-bonded sensor and front-end readout chip. The sensor is radiation tolerant silicon in 250 μm thickness. The pitch of the pixel readout is 50 μm in the ϕ-direction, and 400 μm in the z-direction. The resolution of the impact parameter in the ϕ-direction is better than 15 μm, and in the longitudinal z-direction better than 1 mm, allowing primary vertex reconstruction of charged tracks [8] [9]. The pixel detector has over 80 million readout channels, which is about 50% of the total number of the readout channels in the entire ATLAS experiment.

Because of the short distance from the beam pipe, the radiation hardness is the most important issue of pixel detector developments. At the position of the innermost barrel layer of the pixel detector, the total particle fluence is in the order of 10^{15} n_{eq} cm^{-2} in 5 years of LHC operation [10] (see section 6.1.2 for the definition of the unit n_{eq} cm^{-2}). The performance of radiation-damaged pixel detectors is the major topic of this research. Therefore, the design and operation principles of hybrid pixel detector is introduced in detail in chapter 3.

Tracker

The tracker measures the positions of charged particles, reconstruct tracks and interaction vertices, and measures the momenta of charged tracks. The ATLAS tracker has three parts: the pixel detector, the silicon strip tracker (SCT) [11] [12], and the transition radiation tracker (TRT) [13], from center to the outside, respectively. A 2 T magnetic field is applied along the beam axis to bend the trajectories of charged particles, so the transverse momenta are measured from the curvature of the tracks.

High granularity of the trackers is required to perform precise measurements. This is fulfilled by using semiconductor pixel and strip detectors at the innermost radii, straw-tube tracking detectors with transition radiation measurements at the outer part. The whole inner detectors begins a few centimeters from the beam axis, extends to a radius of 1.15 m and the length is 7 m, providing tracking coverage over $|\eta|<2.5$[1].

The design of the SCT is similar to the pixel detector, but the readout channels are strips with 80 μm pitch along the ϕ direction at the barrel. It has 4 barrel layers, and 9 layers at each end cap. The pixel detector and SCT together provide at least 7 measurements per track.

The TRT measures both tracking points and transition radiation, which is emitted by the particle when it passes the border between different dielectrics. TRT provides additional 36 tracking points, and the transition radiation assists in the particle identification, e.g. distinguish between electron and pion tracks.

[1] The pseudo rapidity is defined as $-\ln(\tan(\frac{\theta}{2}))$, where θ is the angle between the beam axis and the particle trajectory. $\theta = 90°$ corresponds to $\eta = 0$. $\theta = 0°$ to $\eta = \infty$. $\theta = 10°$ equal to $\eta = 2.44$.

Calorimeters

The calorimeters measure the energy of the particles by absorbing the energy and sampling the shape of the resulting particle shower (see fig. 2.3). They are divided into two sub-detectors in ATLAS: the electromagnetic calorimeter (ECAL) [14], where the energy of the photons and electrons is absorbed via electromagnetic interactions, and hadronic calorimeter (HCAL) [15], where the remaining particles such as massive or neutral hadrons lose energy in very dense material by either the electromagnetic, the strong force, or nuclear interactions. Only muons and weakly interacting particles like neutrinos can pass the calorimeters.

The ECAL uses lead and stainless steel as absorbers, and the liquid argon is the active material to record the signals from ionization of the shower particles. The special design is the accordion (zigzag) structure, allowing readout at the edges and providing more absorber/sample transitions in all directions. The whole electromagnetic calorimeter is embedded in a cryostat to keep the argon in the liquid state.

The HCAL is after the ECAL, and heavy materials such as lead, copper and tungsten are used as the absorber to stop the massive, energetic hadrons. The active layer to record the signal is scintillator in the barrel region, and liquid argon is used for the forward regions.

Muon spectrometer

Muons present in the final states of many interesting physical interactions, e.g. weak interaction of Standard Model and Higgs decay channels. They can penetrate the calorimeters and reach the outermost part of ATLAS, so the clear signature of muon is every helpful in selection of interesting events. The muon spectrometer is the outermost sub-detector of ATLAS, designed to measure the trajectory and momentum of muon in high precision.

The muon spectrometer [16] is extremely large in ATLAS, extending from a radius of 4.25 m around the calorimeters out to the full radius of the detector (11 m). The huge size is required to accurately measure the momentum of muons. The principle of detection is similar to the trackers: the muon trajectory is bent by the magnetic field, and the curvature is used to measure its momentum.

The muons are detected in the barrel section by monitored drift tubes. In the high occupancy forward directions cathode strip chambers are used. The muon signals at the forward region also contribute to the trigger of data recording, so the system is optimized for fast readout.

Trigger system

The proton-proton collisions in ATLAS produces enormous amount of data. The frequency of bunch crossing is 40 MHz, and in each bunch crossing about 20 inelastic proton-proton collisions can occur, producing around 1.5 megabytes of data in the cache of the detector [17]. This amount of data is far too high to be permanently stored, and has to be selected by a trigger decision in a very short time ($\sim$ 2.5 μs), and then be transmitted out of the detector.

The trigger system [18] selects the data in 2 stages. The first stage is in the hardware, using parts of the calorimeters and the muon system to search for distinct useful signals, such as energetic leptons, jets, and large missing or transverse energy. Then the data are passed to the second stage. The second selection trigger is a package of optimized software algorithms running on a computer farm using the information from the full ATLAS detector. Finally,

the event filter will do sophisticated analysis of the data and decides whether an event gets permanently stored.

All the decision is done within 4 seconds. The final rate is in the order of hundred megabytes per second, equal to three petabytes per year.

2.3 Upgrade

To detect the physical interactions in the collider experiments, the number of events should be large enough to be significant, and the statistical error can be reduced, too. The average number of events $\langle N \rangle$ is given by the product of the cross section of the interaction σ and the integrated luminosity $\mathcal{L}(t)$ over the observation time T:

$$\langle N \rangle = \sigma \int_0^T \mathcal{L}(t) dt \tag{2.1}$$

If the measured event is Gaussian distributed, the statistical error of the measurement is $1/\sqrt{N}$, which means that four times of the observation time is required to half the error, if the luminosity remains the same. To speed the rate of the detections up, $\langle N \rangle$ has to be increased by either increasing the interaction cross section, or by increasing the luminosity. The cross section can be increased by higher collision energy. However, this choice requires higher magnetic field for the proton accelerators, which is extremely costly. Therefore, the feasible option at the moment is to increase the luminosity.

The High luminosity Large Hadron Collider (HL-LHC) is the project to upgrade the current LHC by luminosity. Two phases of upgrades are planned: The Phase I upgrade takes place around 2017. The expected peak luminosity will be increased to 3.0×10^{34} cm^{-2} s^{-1}, and the total integrated luminosity is expected to be 550 fb^{-1} [19] [20]. Before the Phase I upgrade, in 2013 or 2014, a fourth layer will be inserted to the present pixel detector between the beam pipe and the current innermost layer, which is called the Insertable B-layer (IBL) [20]. Simulations for IBL show that the pions from the proton-proton collision dominate the radiation background at the inner detector region. Beyond 10 cm from the collision point, the neutrons from the back splash of the calorimeters become important, too [20] [21]. For the IBL, which is 3.1 cm away from the beam pipe, the 1 MeV neutron equivalent fluence is 3.3×10^{15} n_{eq} cm^{-2} at $|\eta| = 2.5$ [20] when the total integrated luminosity is 550 fb^{-1}. Additionally, the systematic errors from the event generator of the simulation and the uncertainty on the Si damage factors must be considered. 60% safety factor was chosen for the design of IBL [20], which means that the pixel detectors for IBL must withstand a total fluence of 5.0×10^{15} n_{eq} cm^{-2}.

In the 2020s during the phase II upgrade, the triplet magnets of the LHC will be replaced [22] to achieve the peak luminosity of 10^{35} cm^{-2} s^{-1} [23], which is 10 times of the luminosity of the current LHC. The goal is to reach the integrated luminosity of 3000 fb^{-1} in 10 to 12 years [22]. Since the collision energy is the same, the composition of the radiation is unchanged, but the total fluence of the particles is proportional to the integrated luminosity. Therefore, the total fluence is expected to be 2 to 3×10^{16} n_{eq} cm^{-2} in 10 to 12 years of HL-LHC operation if the a detector is 3.1 cm away from the interaction point at $|\eta| = 2.5$.

The main challenges from the HL-LHC environment are the increasing radiation damage and the higher particle density. To remain or even improve the the performance of the pixel

detector, several changes to the current design were purposed, and research and development are on-going. Three types of promising sensor technologies are currently under investigation : planar-Si, 3D-Si with active edges, and diamond. All of them must be radiation-harder than the current planar-Si sensor of ATLAS pixel modules to survive form the more intense particle fluence. New pixel readout technology with smaller pixel size (for higher point resolution) and faster readout rate must be developed to sufficiently measure the particle from the HL-LHC. Apart from the pixel detector modules, for the current IBL design, the material budget were minimized by using new lightweight mechanical support materials, and CO_2 based cooling system were purposed [24].

This research focuses on the pixel detector modules for HL-LHC. The performance of the diamond and planar-Si pixel detectors after 10 years of radiation damage in HL-LHC is the major interest of this thesis.

Chapter 3

Hybrid Pixel Detector

The ATLAS pixel detector is a hybrid pixel detector, composed of a semiconductor sensor and a pixel readout chip. The sensor and the readout chip are produced separately, and then they are bonded together by metal bump-bonds (see fig. 3.1). The signal generated in the sensor is collected and amplified by the pixel readout circuit. In this chapter the operation principle of the sensor and the design of the pixel readout circuit are reviewed.

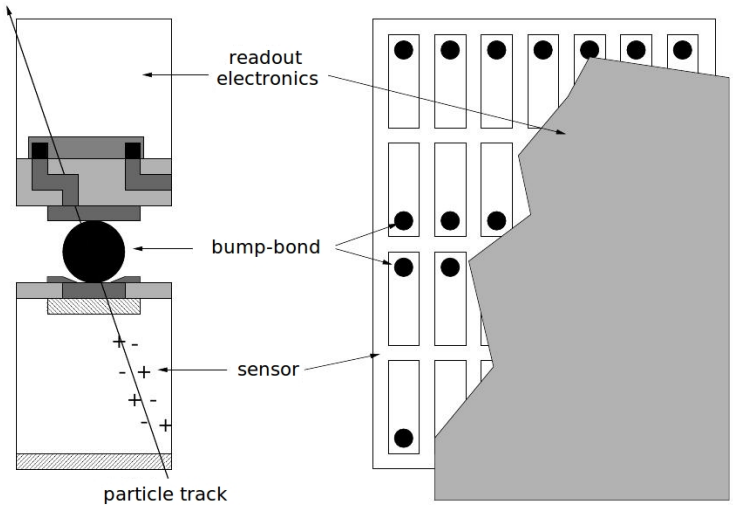

Figure 3.1: Hybrid pixel detector [25]. The schematic diagram on the left is the cross section of sensor and pixel readout chip bump-bonded by solder bump. On the right side is the view from the readout chip, showing the pixel metallization and bumps on the sensor.

3.1 Sensor

Sensor concepts

The charged particle is detected by ionizing the atoms of the sensor material, and the generated charge carriers become the electronic signals to detect.

The sensor is a few hundred micrometers of semiconductor with electrodes, biased by high voltage (as illustrated in fig. 3.2). The electron and hole pairs created by the penetrating particle move in opposite directions in the electric field, and induce the signal current i_{sig} on the readout electrodes:

$$i_{sig} = q\vec{v} \cdot \vec{E}_W \tag{3.1}$$

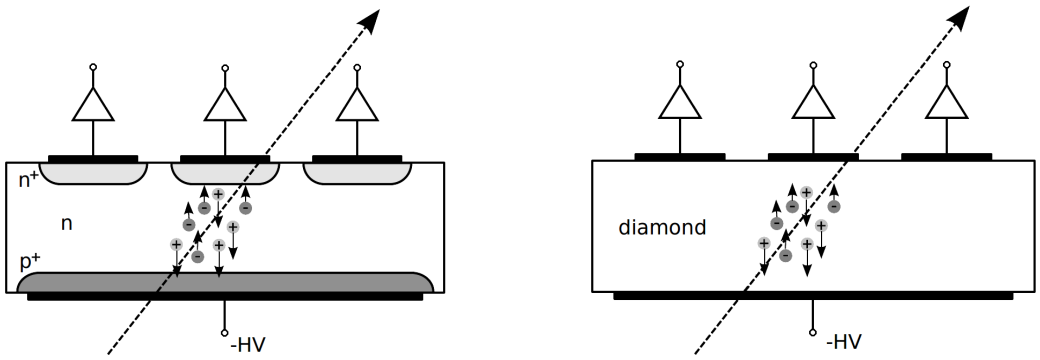

(a) (b)

Figure 3.2: Schematic diagrams of (a) planar Si n-in-n sensor and (b) diamond sensor. The traversing particle leaves energy in the sensor by ionization, generating electron and hole pairs. The charge carriers move in the applied electric field. The moving charges induce currents on the electrode, which are further processed.

where q is the charge. $\vec{v}$ is the velocity of the charge carrier. $\vec{E}_W$ is the weighing field. Velocity $\vec{v}$ is proportional to the electric field $\vec{E}$ and the mobility μ when the electric field strength is small, following the relation $\vec{v} = \mu\vec{E}$. When $|\vec{E}|$ is large, the drift velocity $|\vec{v}|$ saturates and becomes approximately a constant in any field strength. The weighting field $\vec{E}_W$ is a geometrical parameter, describing the coupling of an electrode to the movement of the charge. It is obtained by applying unit potential to the considered electrode and zero potential to the others. To calculate the induced charge on the electrode by the drifting charge carriers q in time interval $[t_1, t_2]$ from position $\vec{x}_1$ to $\vec{x}_2$, one has to integrate eq.(3.1) over the time of the charge collection:

$$Q_{induced} = \int_{t_1}^{t_2} i(t)dt = q\left[\phi_W(\vec{x}_2) - \phi_W(\vec{x}_1)\right] \tag{3.2}$$

where ϕ_W is the weighting potential obtained by the integration of the weighting field over the space. The induced charge $Q_{induced}$ must be equal to q, if the charge collection time is long enough, and no charges are lost due to the crystal defect or field structure in the sensor bulk.

Intrinsic semiconductors or insulators do not have space charge in the bulk, so the electric field strength inside the sensor is constant through the bulk as a parallel plate capacitor:

$$\left|\vec{E}(x)\right| = \frac{U_{bias}}{d} \tag{3.3}$$

However, beside the ionization by particles, charge carriers can be generated by thermal excitation as well. Due to the large band gap of diamond, the thermal charge carriers are negligible compared to the signals, even if operated at room temperature. On the other hand, in case of typical semiconductors like Si and Germanium (Ge), due to the smaller band gap the charge carriers can be generated or recombine at the room temperature. A thermal equilibrium is reached between the excitation and recombination, and the free carrier concentration at the thermal equilibrium state is called the intrinsic carrier concentration (n_i). The n_i at room tem-

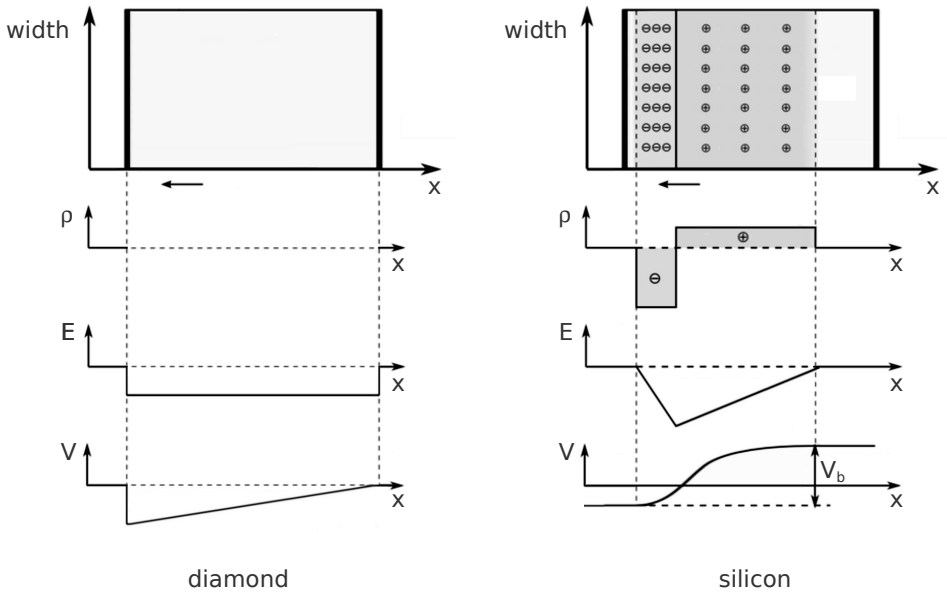

Figure 3.3: The space charge density (ρ), electric field (E) and potential (V) at biased diamond and silicon sensors

perature dominate over the carries produced by the radiation, so doping and reverse biasing must be applied to Si sensors to deplete the region of the junction. Also, Si detectors must be operated in low temperature after irradiation, to keep the leakage current low.

The space charge in the depletion zone alters the electric field. The concentration of the space charges is constant over the depletion zone, so the electric field strength rises linearly along the direction of the field, as shown in fig. 3.3 on the right. If the sensor is fully depleted, the electric field strength as a function of position x is given by

$$E(x) = \frac{2U_{bias}}{d^2} \cdot (x - d) \tag{3.4}$$

The Si sensor is a lightly-doped n-bulk with a highly doped p-implant, so the depletion zone can extend over the full bulk. The required voltage for full depletion depends quadratically on the thickness d and linearly on the effective doping concentration N_{eff} of the bulk:

$$U_{dep} \approx \frac{e}{2\varepsilon_0\varepsilon_r} N_{eff} d^2 \tag{3.5}$$

At lower biasing the sensor is only partially depleted and no electric field is present in the undepleted zone to separate the charge carriers. They will recombine and the signals are lost. Therefore, the sensor is usually over-depleted, which means that the voltage is higher than U_{dep} and the excess voltage adds up to eq.(3.5).

Table 3.1: Properties of diamond and Si

symbol	property	diamond	Si	unit	reference
ρ	density	3.35	2.33	$g\,cm^{-3}$	
$E_{e/h}$	energy to create an electron-hole pair	13.1	3.61	eV	[28] [29]
ϵ_r	relative permittivity	11.9	5.7	none	
κ	thermal conductivity	>1800	1.48	$W\,cm^{-1}\,K^{-1}$	
X_0	radiation length	12.1	9.4	cm	[30]
E_g	band gap	5.48	1.12	eV	
PKA	minimum displacement energy	43	25	eV	[26] [27]
μ_e	electron mobility	4500(1800)	1450	$cm^2\,V^{-1}\,s$	[31] [32] [33]
μ_h	hole mobility	3800(1000)	505	$cm^2\,V^{-1}\,s$	[31] [32] [33]
V_{sat}	saturation voltage	0.8	1.0	$V\,\mu m^{-1}$	[31] [34]
$v_{sat,e}$	electron saturation velocity	$\sim 10^7$	$\sim 10^7$	$cm\,s^{-1}$	[31] [34]
$v_{sat,h}$	hole saturation velocity	$5.6{\cdot}10^6$	$7.5{\cdot}10^6$	$cm\,s^{-1}$	[31] [34]

3.2 Comparison of diamond and silicon

The properties of diamond and silicon (Si) relevant to the pixel detector design are summarized in Table 3.1.

Diamond is a very promising material for a vertex detector, mainly because of its large band gap leading to negligible leakage current, and small relative permittivity giving small capacitance. Both properties lead to small electronic noise. Another interesting property is the strong valance bonds between carbon atoms in diamond, so the energy to displace an atom from the lattice is higher for diamond (43 eV [26]) than for Si (25 eV [27]). This property implies that diamond is radiation harder than Si, which is also very attractive for vertex detector design. Furthermore, there are good properties of diamond that benefit the pixel detector from the system point of view: The long radiation length means that the material budget is low. Due to the extremely high thermal conductivity, the cooling for diamond pixel detector can be simpler than for Si ones. The carrier mobilities are large, so the signal collection in diamond is fast.

However, the energy to create an electron and hole pair in diamond is 3.6 times that of the energy in Si, so the signal in diamond is smaller than in Si at least before the irradiation. After the sensor is damaged by radiation, the signal deteriorates because of trapping of the charge carrier, and the noise increases because of the generation of leakage current. To estimate the performance of diamond and Si detectors, the signal-to-noise ratio (SNR) should be compared with respect to the radiation damage. The detailed comparison of signal, radiation damage, and noise is presented in the following chapter 5, chapter 6, and chapter 7, respectively.

3.3 Pixel readout chip

The front-end readout chip converts the signal from the sensor into digital hits, and buffer the digitized signal until the ATLAS trigger is issued. The most recent ATLAS pixel readout chip is the FE-I4 [35][36], which will be applied in the IBL (see section 2.3). FE-I4 is produced using 130 nm feature size bulk CMOS process. It has 26 880 hybrid pixels arranged in 80 columns with 250 µm pitch by 336 rows with 50 µm pitch. The readout circuit contains a charge sensitive amplifier (CSA), a discriminator, and a digital readout interface. A picture of the readout chip is shown in fig. 3.4.

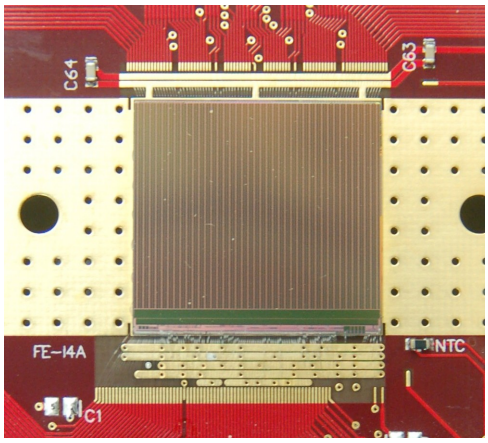

Figure 3.4: Picture of FE-I4 chip

The signal from the sensor is fed into the input of the CSA via the bump-bonded sensor-chip connection. The analogue circuit diagram is shown in fig. 3.5.

The first stage of the analogue circuit is a charge sensitive amplifier (CSA) with a 17 fF feedback capacitor C_{f1}. The signal current is collected by the C_{f1}, and the output voltage v_{out} is proportional to the input charge Q by the relation $v_{out} = -Q/C_{f1}$. The C_{f1} is discharged by an adjustable constant current source. For a signal from a 200 µm sensor, 15k electron-hole pairs are expected, the discharge current is set to 19 nA, so the output voltage v_{out} returns to base line in about 125 ns. A leakage current compensation circuit is attached at the input of the CSA, which filters the DC signal from the sensor leakage current.

The first stage pre-amplifier is followed by a AC-coupled second stage amplifier. The second stage amplifier has a broad bandwidth, providing further amplification of the signal without any shaping. Finally, the amplified signal is passed to a discriminator. The threshold is adjustable in the range of 1000 to 6000 to distinguish real hits from noise.

Fig. 3.6 shows the output signal of the analog circuit. Because of the constant current discharge, the time between the leading and trailing edge while the signal is above the threshold, the time-over-threshold (ToT), is proportional to the pulse height of v_{out} and therefore proportional to the number of the input signal charge. For a hit, the position of the pixel, the bunch crossing at which the signal cross the threshold, and the TOT is recorded.

The FE-I4 column pairs are divided into 2 by 2 pixel regions. Each region contains four identical analog front ends, connected to one shared memory and logic block (digital region), see fig. 3.7. The digital region can store up to five regional hits. For each regional hit, a counter

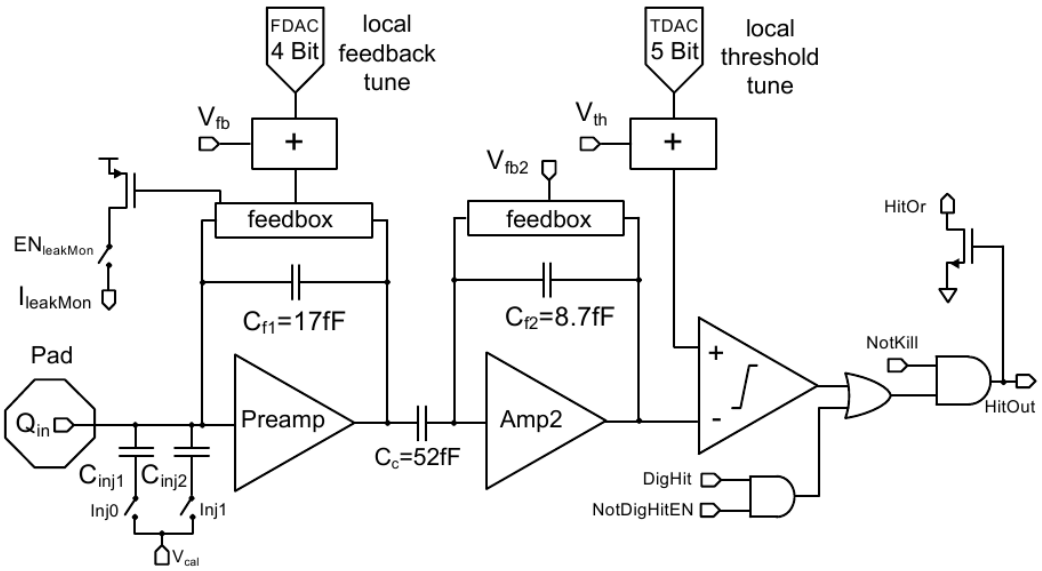

Figure 3.5: Schematic diagram of the FE-I4 pixel cell readout circuitry [37]. From the left to the right, the components are the bump pad connected to the sensor, the first and second stage amplifier, and the discriminator, respectively. The FDAC and TDAC are digital-to-analogue converters to set the feedback current and threshold up, respectively.

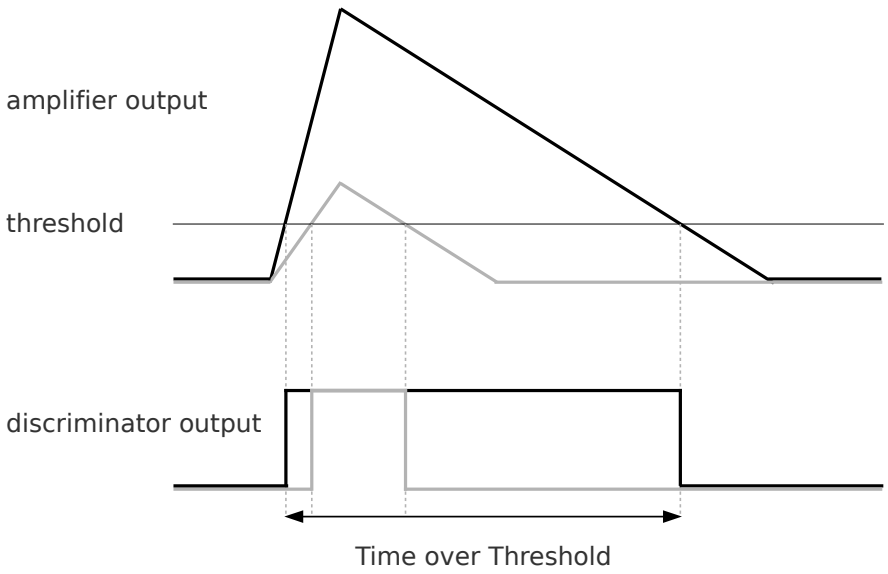

Figure 3.6: Signal processing of the pixel readout. The signal at the output of the charge sensitive amplifier is shown on the top. The pulse height is proportional to the umber of input charge, and the voltage decreases linearly due to the constant current discharge. The corresponding Time-over-Threshold (ToT) signal at the output of the discriminator is shown on the bottom. The black line is the signal of large charge input. The gray line is for small charge input.

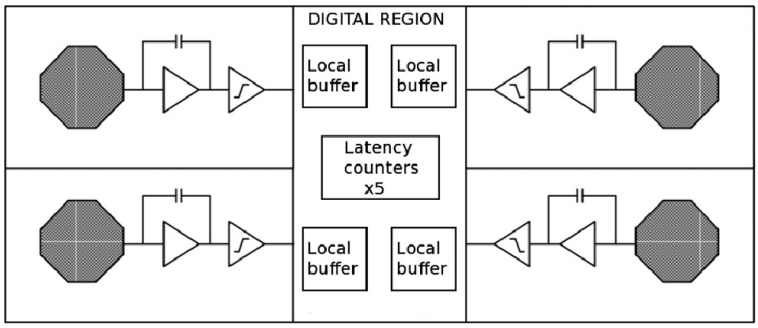

Figure 3.7: Diagram of a digital region. Four analogue sections are connected to a central digital region [36].

keeps track of the time elapsed since it was produced in units of bunch crossings (25 ns). When an external trigger arrives, the trigger selects all regions for which one of the five time counters matches the trigger. On the other hand, if no trigger is received, the region-hit is erased.

To test the pixel amplifier and the discriminator, each pixel cells contains a charge injection circuit, which is composed of injection capacitors C_{low} = 1.9 fF and C_{high} = 5.7 fF. A variable voltage pulse V_{CAL} is applied on the injection capacitor, and the amount of the injected charge is equal to $Q_{inj} = C_{low/high} \cdot V_{CAL}$. The exact value of the C_{low} and C_{high} is measured during the wafer production. The dispersion of the number is within 10% [38]. The charge injection circuit is used to measure threshold, noise, and the ToT-calibration for the pixels.

3.4 Sensor-chip interconnection

The pixel electrodes on the sensor are connected to the readout chip using Sn/Ag bumping and flip-chipping technology [39][40] provided by Fraunhofer-Institut für Zuverlässigkeit und Mikrointegration (IZM), Berlin, Germany.

The bumps are deposited on the pixel chip in several steps. Firstly, the under bump metallization (UBM) is sputtered on the pixel pads on the chip. The UBM consists of several metal layers that prevent diffusion of the solder material and improve its adhesion and wettability. Then the bumps are grown in a galvanic process on top of the UBM. In our case the bumps are grown on the chip. The sensor has only the UBM metallization. Subsequently, the chips are heated up, so that the molten bumps shrink into a spherical shape by the surface tension. Finally, the chip and the sensor are mated by flip-chipping. The bump pads of the two parts are brought on top of each other. The bump-bonds melt during the heat up, and then the two parts are self aligned by the surface tension of the molten bumps, so the bonds are formed.

Fig. 3.8 shows a picture of the bumps.

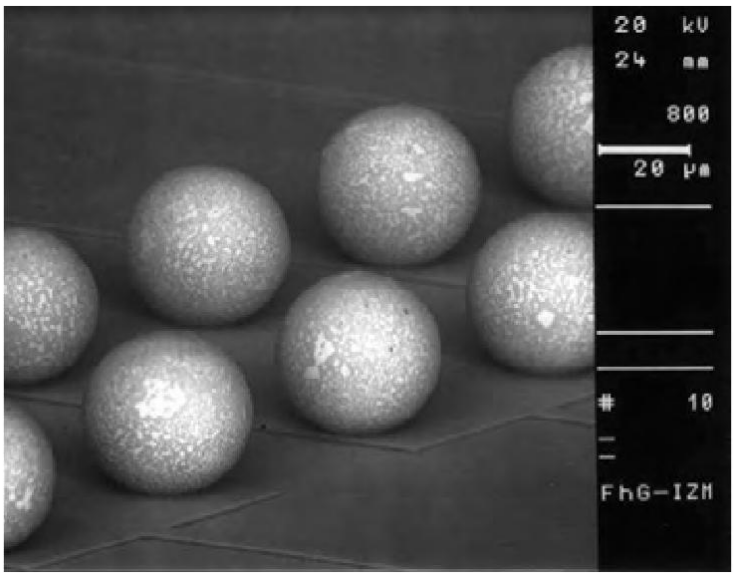

Figure 3.8: Picture of the Sn/Ag bumps [40].

Chapter 4

Diamond Pixel Detector Modules

The signal-to-noise ratio (SNR) of the diamond pixel detector must be evaluated and compared to that of the silicon (Si) ones. To characterize the diamond sensor before and after irradiation, and to measure the noise of the real device, two single crystal diamonds made by Chemical Vapor Deposition process (sCVD diamonds) have been bump-bonded to the FE-I4 pixel readout chip for the measurements. One of them is unirradiated, the other one irradiated using 25 MeV protons. In this chapter, the experimental methods for the SNR characterization are introduced. Section 4.1 is a brief review for the fabrication of artificial diamonds, and the production of diamond pixel modules. Process of irradiation of the pixel modules is described in section 4.2. Then the methods to measure signal and noise of a diamond pixel module are explained in section 4.3. Results and discussion of the SNR measurements are presented in section 4.4.

The measurements here provide the references for further calculation and simulations in the following chapter 5 for signal, chapter 6 for radiation damage, and chapter 7 for noise from the pixel readout.

4.1 Production of diamond pixel detectors

Fabrication of artificial diamonds

Synthetic diamonds are produced by the chemical vapor deposition (CVD) process in the industry [41]. Typically, methane (CH_4) and hydrogen (H_2) gases are fed into a chamber with 700-1000°C deposition temperature and gas pressures in the range 30-300 Torr. The gases are energized by microwave to form a plasma, then the carbon atoms in the gas deposit on a substrate in crystalline form.

The single-crystal CVD diamonds (sCVD diamond) starts from a single seed at the beginning of the growth process, so the crystal is continuous and uniform. However the growth of sCVD diamond is slow, and only small sized diamond are available. The poly-crystal diamond (pCVD diamond) starts from parallel formation of multiple seeds, and in the growth process further growth is dominated by some of the seeds, resulting in a grain structure as shown in fig. 4.1. Big sized wafers (~10 cm) are only available for pCVD diamonds. The coarse surface of the grown diamond need to be grained, and the diamond must be thinned to the desired thickness from the low-quality substrate side.

The defects and impurities in the crystal cause trapping and recombination centers, so the average life time of the charge carriers is shortened. The grain boundaries in the pCVD diamonds act as bulk defects, therefore pCVD diamond has similar charge collection features like sCVD diamond after irradiation. So far the maximum effective charge collection distance in

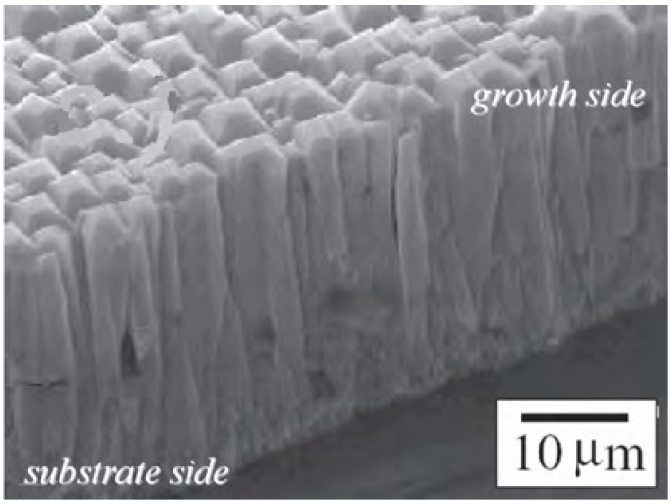

Figure 4.1: Grain structure of pCVD diamond [42]

pCVD diamond wafer is 275 µm [43]. In case of sCVD diamod, the collection distances are in the range of centimeters [31].

The sCVD diamonds used in the following characterization are fabricated, thinned to the desired thickness, and cut to the required shape using laser by the manufacture "Diamond Device Limited". Both diamonds have surface area of 4.8 mm × 4.8 mm. The diamond DDL7 is 507 µm thick, and the other diamond DDL4 is 542 µm thick.

Metalization and connection to the pixel readout chip

The diamonds are polished, cleaned by organic solvents[1] and O_2-plasma to remove the chemical residue on the surface, e.g. graphite due to laser cutting, any compound with O, H, or N which become surface defect. Metal is sputtered on the surface of the diamond to produce the electrodes for biasing and pixel readout. This metallization process is done by the Institut zuer Zuverlaesigkeit und Microintegration (IZM) in Berlin, Germany, using the Argon Re-sputtering Technique.

For the back plane, 230 nm of Ti-Tungsten (TiW) is sputtered on the diamond, and 200 nm of gold subsequently on the top of the TiW. For the pixel side, 200 nm of TiW is first sputtered, secondly 300 nm of copper (Cu) on the TiW. Then a lithography mask with a pixel structure is made on the metal, and the TiW/Cu between the pixels are removed by wet etching. After sputtering of metals, the diamond is annealed in 450°C for 4 minutes, so the surface defect caused by the sputtering can recover. Finally the diamond pixel sensor is bump-bonded to FE-I4 readout chip as described in section 3.4.

The picture of the metalized diamond is shown in fig. 4.2(a), and the sCVD diamond bump-bonded to FE-I4 pixel readout chip is shown in fig. 4.2(b).

[1] H_2N_2:NH_4OH = 1:1, Acetone, and Methanol

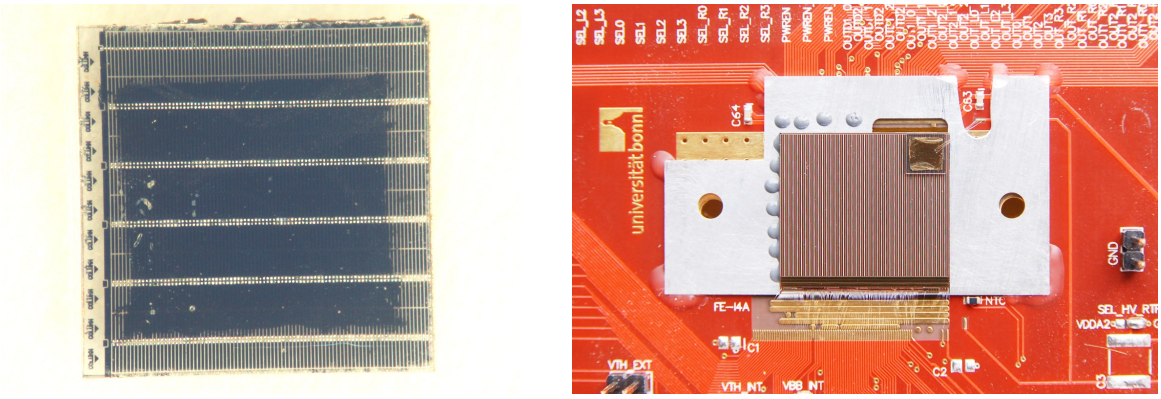

(a) (b)

Figure 4.2: (a) sCVD diamond sensor with pixel metalization (b) The sCVD diamond diamond pixel detector, wire-bonded to a printed circuit board for data readout.

4.2 Proton irradiation

One of the sCVD diamond (the DDL4) is irradiated by 25 MeV protons to measure the signal after radiation damage. Beside the sCVD diamond DDL4 with the pixel readout, two pCVD diamonds with pad readout were irradiated to study the signal loss as a function of the proton fluence. The results are reported in detail in section 6.2. The irradiation facility and the process are explained below. The setup of the irradiation facility is shown in fig. 4.3.

The 25 MeV proton beam is offered by the Compact Compact Cyclotron at the Karlsruhe Irradiation Center. The H^- is accelerated in the cyclotron, and its two electrons are stripped by a foil, so the proton beam is obtained. The energy of the proton at the extraction is 25.3 MeV [44]. The diamonds is held in a thermally and electrically insulated box, that is 50 cm away from the exit window of the beam. The diameter of the proton beam is 4 to 8 mm, so the box is mounted on a controlled XY-stage to scan the diamonds.

To cool the diamonds while irradiated, cold nitrogen gas is flushed through the insulated box, and the ambient temperature was -80°C. ^{58}Ni foil is attached pn the surface of the diamond to measure the proton fluence by the activity of isotope ^{57}Ni from the nuclear interaction between protons and ^{58}Ni, and thus the protons lose energy in the Kapton and ^{58}Ni foils before hitting the diamond. Simulation shows that the energy of the proton at the target is (22.9±0.2) MeV, and the uncertainty on the total fluence is 13.75% [44].

After the irradiation, the irradiated diamonds are stored in a fridge with ambient temperature -80°C for 2 to 3 weeks until the nuclear activation at the metals decays. Then the irradiated diamond detectors can be tested directly in room temperature without annealing.

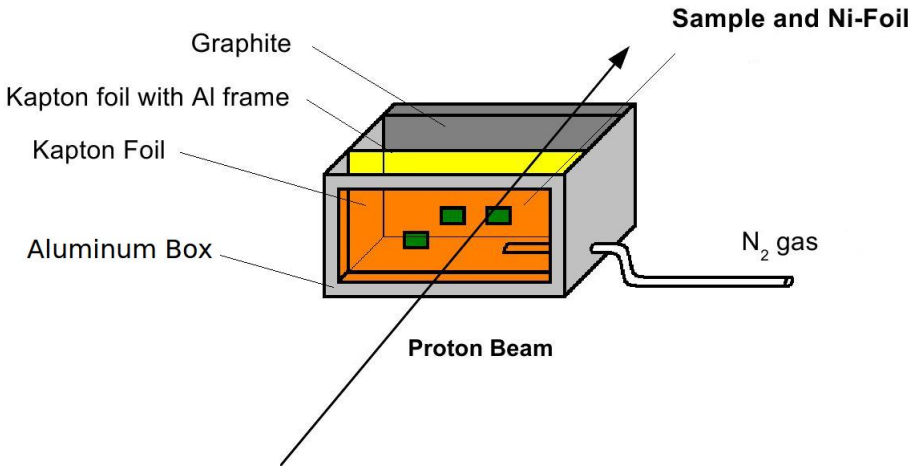

Figure 4.3: 25 MeV proton irradiation setup at the Karlsruhe Irradiation Center. The samples are fixed on a Kapton foil supported by an aluminum frame, and the frame is inserted into an aluminum container for cooling. The container is an aluminum box with the size 21 cm × 21 cm × 48 cm with an window opened for the proton beam. The window is covered by Kapton foil. -80°C nitrogen gas (N_2) is fed into the aluminum box to keep the samples cool during the irradiation. The box is mounted on a stage, which can move in vertically and horizontally, so the proton beam can scan the samples. Nickel foil (^{58}Ni) is attached at the back of the irradiated samples, so that the total irradiation fluence can be measured by the activity of ^{57}Ni which is produced by the process ^{58}Ni + p $\rightarrow$ ^{57}Ni + other products.

4.3 Methods of characterization

The USBpix test system

The USBpix test system can operate the characterization tests and read the data from the FE-I4 pixel readout chip. The hardware consists of a multi-purpose FPGA[2] card (Multi-IO board) and a adapter card for the single FE-I4 chip, see fig. 4.4. The hardware has been developed at the University of Bonn, Germany.

The Multi-IO Board generates the signal to control the FE chip and provides the external trigger interface. It is connected to the computer through the USB port. The essential part of the Multi-IO Board is the FPGA in which the operation procedure of tests are implemented in the hardware, and a SRAM[3] buffer which stores the data from the pixel front-end chip temporarily. The pixel front-end readout chip is connected to the Multi-IO Board via an adapter card. The adapter card converts the signals from the Multi-IO Board into the form which can be read by the computer, and adjusts the delays of the signal propagation.

The software for the USBpix system is based on the ATLAS PixLib package, that is a collection of C++ classes that were originally developed to control the ATLAS Pixel detector RODs[4] . The hardware specific layer of this package has been adapted to access the pixel chips via the adapter card and the Multi-IO Board. The user interface software is the ATLAS standard read-

[2]Field Programmable Gate Array
[3]Static Random Access Memory
[4]Read Out Drivers

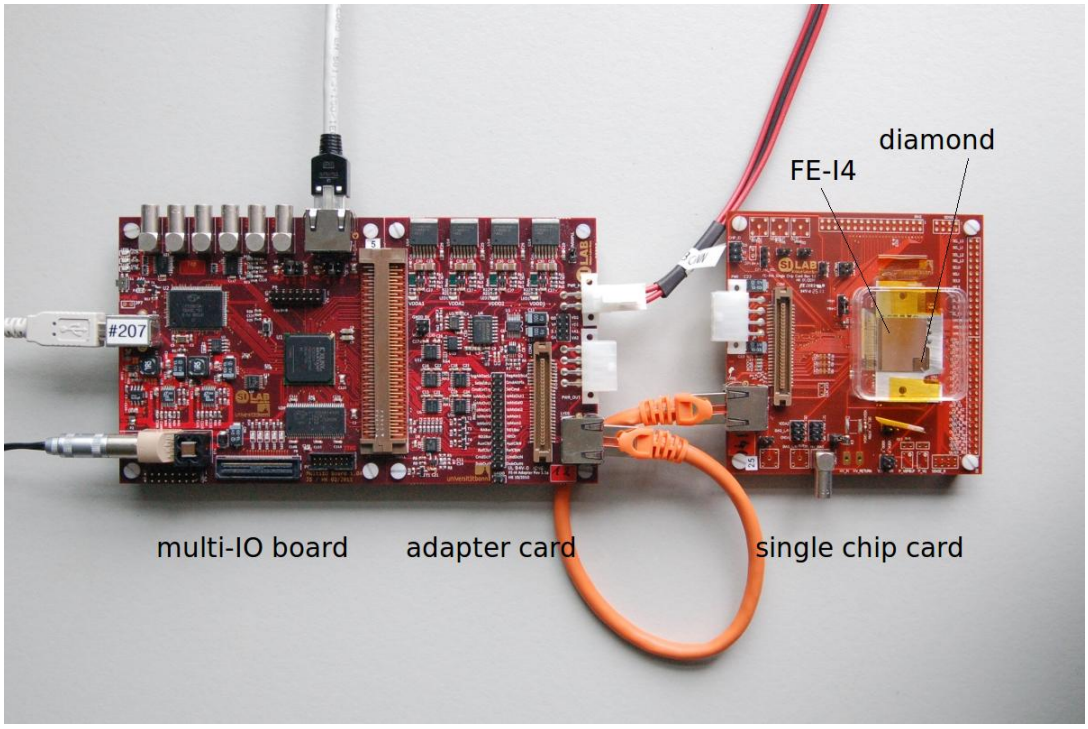

Figure 4.4: Picture of USBpix test system

out software "STcontrol". The software provides automate procedures to configure the chip, and to adjust the test parameters to characterize the pixel detector.

Threshold scan and noise measurement

The hits detected by the pixel must exceed the threshold of the discriminator to be recorded. The thresholds are firstly set by a global DAC[5] for the entire chip, and the fine-tuning is done by individual pixel threshold DACs (TDACs) to compensate the pixel-to-pixel variations and to achieve uniform thresholds for the whole chip.

The threshold of a pixel is measured by the fraction of detected hits as a function of the injected charge. Ideally, the discriminator response is a step function, which means that if the injected charge is lower than the threshold, the output signal is 0; if the injected charge is higher than the threshold, the discriminator output shows a hit. Practically, the electronic noise of the pixel readout circuit introduce fluctuations on the signal voltages, and the amplitude of the fluctuation is Gaussianly distributed. Therefore, the possibility of hits to exceed the threshold can be described by the convolution of a step function and a Gaussian distribution, which turns into the complementary error function (erfc):

$$P(Q_{inj}) = \frac{1}{2} erfc\left(\frac{Q_{thre} - Q_{inj}}{\sqrt{2} \cdot \sigma_{noise}}\right) = \frac{1}{\sqrt{\pi}} \int_0^{\infty} \exp\left(\frac{Q_{thre} - Q_{inj}}{\sqrt{2} \cdot \sigma_{noise}}\right) dQ \tag{4.1}$$

where Q_{thre} is the threshold, Q_{inj} is the injected charge, and σ_{noise} is the sigma of the Gaussian

[5] Digital to Analogue Converter

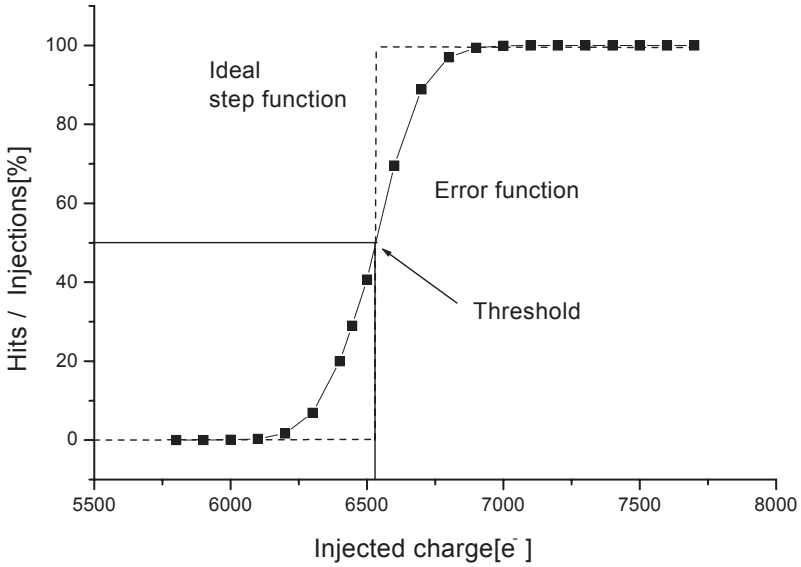

Figure 4.5: Complementary error function (S-curve) for threshold and noise measurement. The threshold is the half-height of the error function. The noise is the sigma from the fit.

distribution. The result of such a measurement is shown in fig. 4.5. The threshold is the Q_{inj} corresponding to 50% of the total number of injections, and the electronic noise of a pixel is the σ_{noise} of the error function. Using this so-called "S-curve" method, the threshold and the noise of a single pixel are measured simultaneously.

The thresholds of all the pixels on a chip must be as uniform as possible. Usually the GDAC value which roughly corresponds to the desired threshold is set first, and then the TDAC has to be tuned to minize the threshold dispersion. This is done by repeating the S-curve threshold scans on a pixel with several discrete TDAC settings, and the TDAC which gives the desired threshold is extrapolated. The desired threshold is 2000 electrons, and the threshold dispersion after the TDAC adjustment can be reduced to 30 electrons. For the irradiated diamond, the threshold is lowered to 1200e to cope with the small signal after irradiation. The typical threshold and noise distributions are shown in fig. 4.6, and the threshold and noise of the used diamond pixel detectors are summarized in Table 4.1.

ToT adjustment and calibration

Time-over-Threshold (ToT) is the unit of a signal in FE-I4. 1 ToT corresponds to 25ns. The ToT is supposed to be proportional to the signal charge as explained in section 3.3. To get an evenly distributed ToT response for all pixels, the feedback current has to be adjusted using a similar method to the threshold tuning. The feedback current is first set by global DAC "IF", and the pixel-to-pixel variation is minimized using FDACs of each individual pixel.

The FE-I4 is not designed for spectrum characterization, so it has only 4-bit resolution to record the signal, namely, there are only 16 bins for the spectrum of the signals. Only the 1st to

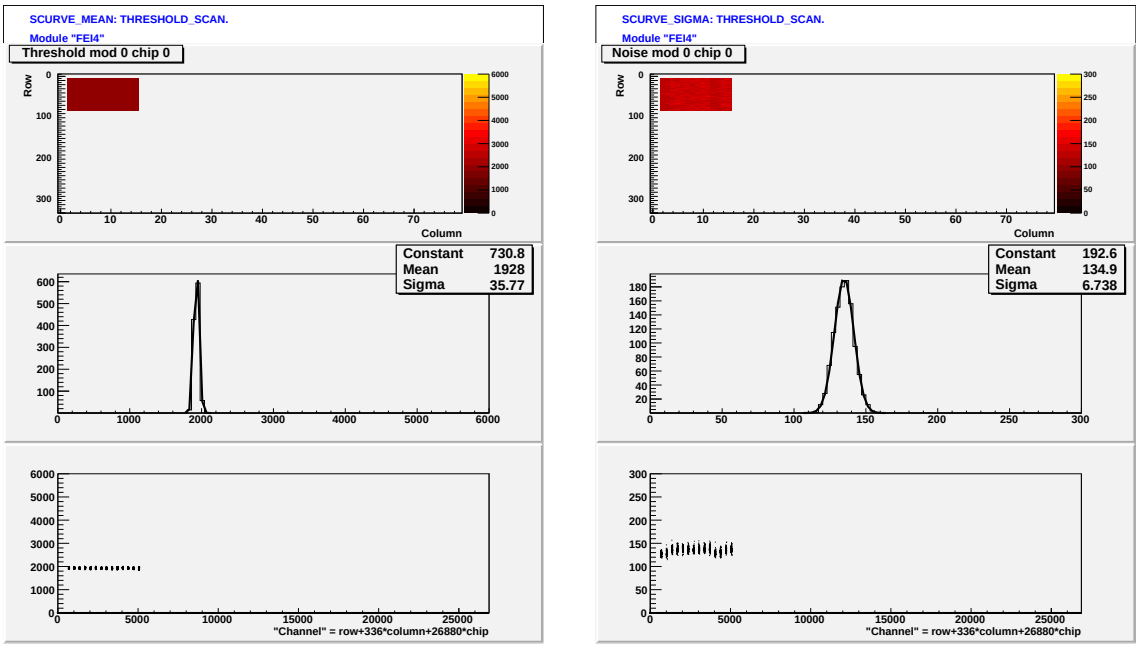

(a) (b)

Figure 4.6: The maps (top), histograms (middle), and scatter plots (bottom) of (a) the threshold and (b) the noise of the tested sCVD diamond pixel module DDL4 after tuning,showing the typical threshold and noise distribution of the pixel detector. The 4.8 mm × 4.8 mm × 507 μm diamond is bump-bonded to the pixels from column 1 to 15 and row 10 to 90. The other pixels which are not bump-bonded are masked during the threshold scan and tuning. The histograms are fit by Gaussian distribution, showing that the threshold is (1928 ± 36) electrons, and the noise is (135 ± 7) electrons.

Table 4.1: Threshold and noise of the tested diamond pixel modules. The target threshold is 2000 electrons. Two threshold configuration were prepared for the irradiated diamond DDL4. The lower one is to cope with the small signal after irradiation.

diamond	DDL7	DDL4
irradiation	0	5×10^{15} p/cm^2
target threshold	2003±30	1928±36
noise	134±11	135±7
lower threshold for irradiated diamond		1196±50
noise		161±12

the 13th bin are for ToT records, the 14th to 16th bin are for codes of status messages. Thus the output of FE-I4 is rather binary digital hits. The number of deposited charge is always given by the center of the coarse segmentation (the ToT bin). In this case, the uncertainty of the ToT is given by:

$$\sigma_{ToT} = \frac{1\ ToT}{\sqrt{12}} = 0.29\ ToT \tag{4.2}$$

The standard configuration of the feedback current of FE-I4 with a 200 µm planar Si sensor is that 15k electrons signal charge give 5 ToT, which is equal to 125 ns.

The ToT values have to be calibrated by injecting known number of charges (Q_{inj}). In theory the relation between the Q_{inj} and the ToT value must be linear. However, due to the change of the DC operating point of the feedback current source versus the signal pulse height, nonlinearities has been observed in the real measurement, especially for signals smaller than 5ke [37].

At the moment of writing this thesis, the automate ToT calibration for each single pixel on the entire ship is still not available in STcontrol. Calibration for at least 15 columns × 100 rows of single pixels per module by hand is technically not feasible in the short time-constrain. Therefore, the calibration is done for all pixels together, and the pixel-to-pixel variation is considered as uncertainty of the calibration. The results for DDL7 and DDL4 are shown in fig. 4.7. The error bar on the charge is the 10% uncertainty of C_{inj}, and the error bar on ToT is the pixel-to-pixel variation. The ToT-to-charge relation can be discribed by the function

$$ToT(Q_{in}) = P_1 - \frac{P_0}{Q_{in} + P_2} \tag{4.3}$$

Hence the calibration for low charges which nearby the threshold and the charges which are higher than the maximum $C_{inj} \cdot V_{CAL}$ can be extrapolated from the fit function. Note that the low and high charge ranges must be fit separately. The fit lines are shown in fig. 4.7. In the following measurements, the ToT numbers are converted into the mean of the corresponding injected charges by a look-up-table extracted from fig. 4.7.

To cross check the ToT-to-charge calibration, the γ-ray radioactive sources are applied to generate signals on the pixel detectors(see section 5.2). In the photon effect regime, the energy of the γ-ray is completely absorbed by the sensor material, so the energy-loss spectrum is a discrete line with a Gaussian distributed smearing due to the electronic noise. While the energy of the photon is high enough and enters the Compton effect regime, the energy loss spectrum is a continuum. The resolution of signal charge in FE-I4 is not high enough to analyze the spectrum of Compton effect. Therefore, the X-ray source tests focus on the photon effect peaks in the spectrum. The applied sources and their essential properties related to the source tests are summarized in Table 4.2. The ToT response produced by the γ-ray sources is plotted in fig. 4.7(a), showing that the γ-ray measurements agree with the calibration by the injection capacitance.

Besides the ToT-to-charge calibration, γ-ray sources can also be applied to test the bump-bond connections and the performance of the individual pixels. The pixels with broken bump-bonds and the dead pixels are directly visible because of their low count rate if the sensor is homogeneously illuminated.

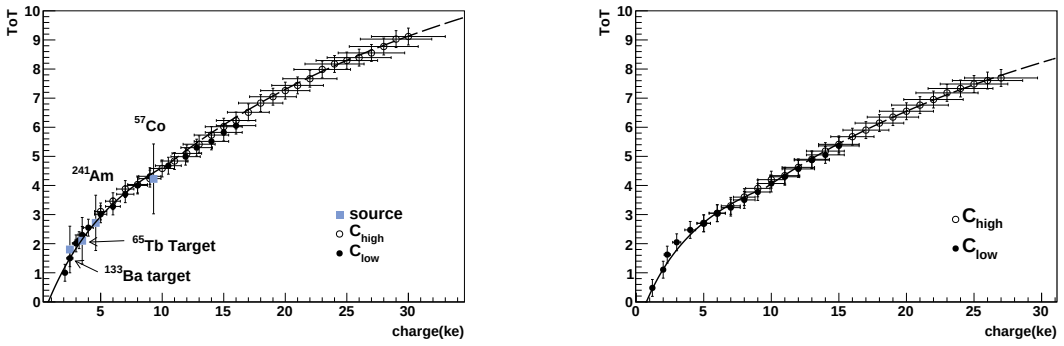

(a) (b)

Figure 4.7: ToT-to-charge calibration for the two tested diamond pixel detectors. (a) DDL7 the unirradiated diamond (b) DDL4 the irradiated diamond, the fluence is 5×10^{15} p/cm^2 by the 25 MeV protons. C_{high} and C_{low} are the injection capacitance in FE-I4, the capacitances are 5.7 fF and 1.9 fF, respectively. The x-axis is the injected charge. The uncertainties of the charge is from the 10% variation of C_{high} or C_{low}. The y-axis is the ToT response at the output, with the error bars showing the pixel-to-pixel variation. The lines are fit by eq. 4.3 to guide the eye. In (a) the squared marker show the ToT response of γ-ray source test.

^{90}Sr Source Test

The β-ray from strontium (^{90}Sr) is used to generate signal in diamond. ^{90}Sr undergoes β^- decay:

$$^{90}Sr \rightarrow ^{90} Y + e^- + \bar{\nu}_e \tag{4.4}$$

The maximum kinetic energy ($T_{e,max}$) of the electron is 0.546 MeV. Then ^{90}Y (yttrium) decays again:

$$^{90}Y \rightarrow ^{90} Zr + e^- + \bar{\nu}_e \tag{4.5}$$

The $T_{e,max}$ of the electron is 2.28 MeV, and the ^{90}Zr is stable. The ^{90}Sr/Y is almost a perfect pure beta source, because the photon emission from the decay of ^{90}Y is so weak that it can be ignored. The energy spectrum of the β-ray electron is a continuum [45](see fig. 4.8). Since the $\beta\gamma$ of those electrons at the high energy end of the spectrum is very close to the $\beta\gamma$ of a minimum ionizing particle (MIP, see chapter 5.1.1), ^{90}Sr is commonly used in the laboratory to test the performance of the detector.

The electrons from the ^{90}Sr is first collimated by a Acrylic collimator wrapped with brass. Acrylic is chosen to be the first layer of the collimator due to its relatively low atomic number (Z), so that it can stop the electrons and eliminating the generation of X-rays from bremsstrahlung, which can become the background. According to the continuous slowing down approximation (CSDA) range calculation by NIST ESTAR calculator [46], 2.28 MeV electrons can be fully stopped in 2 cm of Acrylic, so the diameter of the Acrylic layer is 2 cm. Then the 1.5 cm thick brass wrap can dump the rest x-ray from bremsstrahlung for further protection. With all the designs, the electron beam is clean, narrow, and perpendicular to the sensor surface.

To select the particle at the high energy end of the β-decay spectrum and to ensure that the electrons penetrate the diamond pixel detector completely, a scintillator is placed behind the

Table 4.2: The γ-ray sources used for ToT-to-charge calibration. ^{133}Ba and ^{65}Tb are the target illuminated by the ^{241}Am source. The emitted florescence X-rays are used in the experiments. The table summarizes the energies of the γ-rays, the intensity of a certain γ-ray. P_{PE} and P_{CE} mean the possibility for photoelectric effect and Compton effect in diamond, respectively. "signal of PE peak" means the number of electron and hole pairs generated by the full absorption of γ-rays via the photoelectric effect.

source	energy	intensity	P_{PE}	P_{CE}	signal of PE peak
^{133}Ba target	32.0keV	73%	25%	75%	2.4ke
	37.0keV	16%	25%	75%	2.8ke
^{65}Tb target	44.0keV	75%	5%	95%	3.4ke
	51.0keV	19%	5%	95%	3.9ke
^{241}Am	13.9keV	37%	60%	40%	1.1ke
	26.0keV	2%	25%	75%	2.0ke
	59.9keV	36%	13%	87%	4.6ke
^{57}Co	14.0keV	3%	97%	3%	1.1ke
	122.0keV	86%	~ 0%	~ 100%	9.3ke
	136.0keV	11%	~ 0%	~ 100%	10.4ke

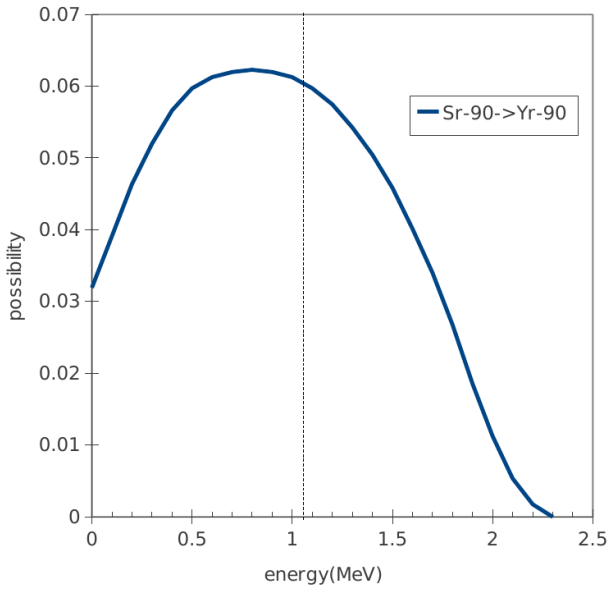

Figure 4.8: Energy spectrum of β-rays from ^{90}Sr [45]. The line is the cut off energy. Only the electrons with kinetic energy larger than 1.24 MeV can trigger the signal measurement.

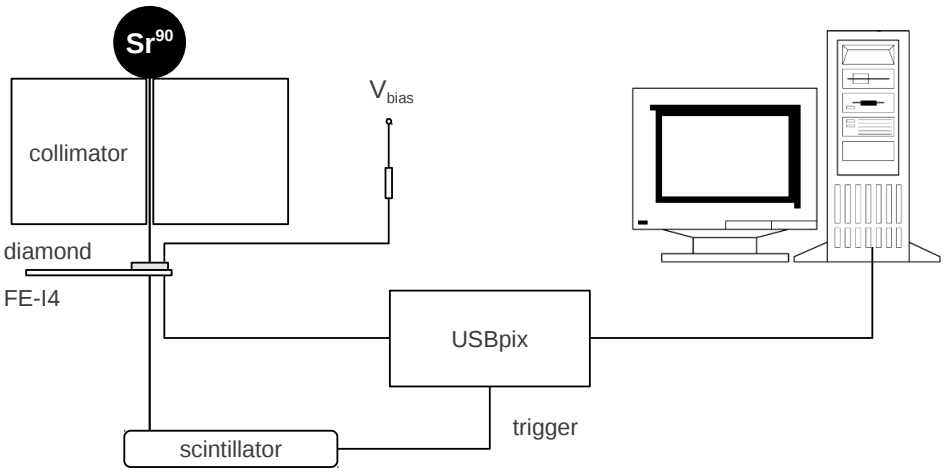

Figure 4.9: Source test setup

diamond pixel detector, and the signal of the scintillator is transmitted to the USBpix system to trigger the data-taking in FE-I4. The CSDA calculator [46] shows that the minimum energy of the electron to penetrate all the material between the source and scintillator is 1.24 MeV, corresponding to the $\beta\gamma = 2.43$. While the USBpix is triggered by the scintillator signal, a 16 bunch-crossing acceptance window is opened, and the positions and the ToT values of the hits appeared in the acceptance window are recorded, and then sent to the computer.

The ToT of the hit is converted into charges, and then the hits are clustered according to their positions. The seed is the hit with maximum ToT in the triggered acceptance window, and the charges of the seed and its neighboring pixels are added up.

The signal spectrum is measured for unirradiated and irradiated diamond pixel detectors. Note that during the illumination by the ^{90}Sr source, the charge carriers can fill the traps, so that the charge collection can increase versus time until saturation is reached. This effect has been observed in irradiated and pCVD diamond, which is called pumping [47]. Therefore, The irradiated diamond must be illuminated by the ^{90}Sr source for 12 hours before measuring the signal spectrum.

4.4 Results

The hit map of the pixel detector shows the unconnected pixel and the noisy pixels, see fig. 4.10. The unconnected and the noisy pixels are masked during the ^{90}Sr source test. Additionally, the charge collection at the rim of of the diamond is not efficient because the back plane metallization does not cover the rim to avoid discharge at the edges, so pixels under the rim without metallization are masked, too. Therefore, the active area for signal collection is the 3mm x 3mm area at the center of the diamond. For the studies of signal spectrum, only the data taken from the fiducial regions in which all the pixels function properly are accepted, in order to exclude the artificial charge loss due to the masked pixels.

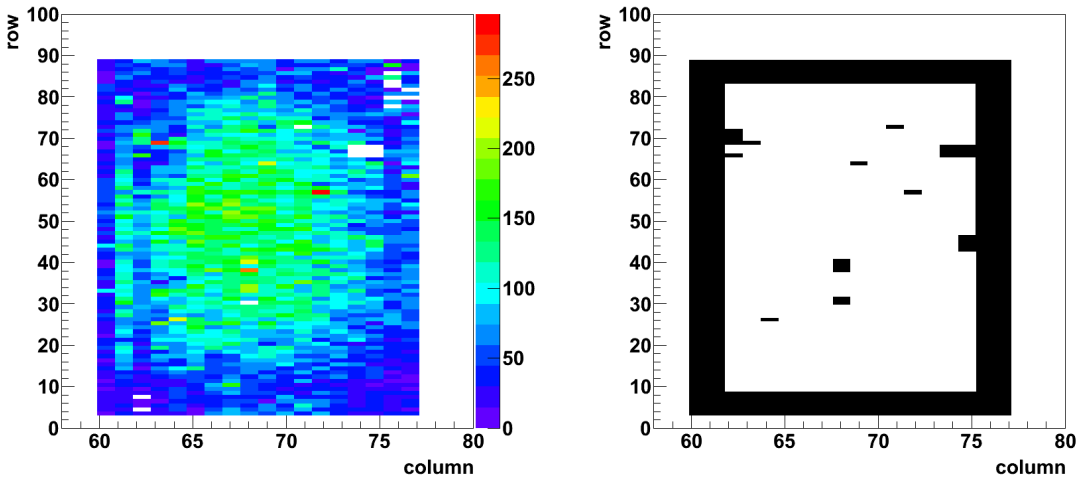

(a) (b)

Figure 4.10: (a) Hit map of a sCVD diamond pixel detector illuminated by the ^{90}Sr source. The pixels with particularly large counts are the noisy pixels. White ones with 0 counts means the pixel is not connected to the sensor. The noisy pixels, dead pixels, and pixels under the rim without metallization are masked during the scans. (b) Map of the the masked pixels.

Fig. 4.11 and fig. 4.12 shows the signal spectra of unirradiated and irradiated diamonds. Fig. 4.11 shows the spectra of n-pixel clusters seperately, where n is from 1 to 5. The signal of unirradiated diamond has larger cluster size because of the large number of signal charge. In case of either unirradiated or irradiated diamonds, the most probable value (MPV) of signals does not depend on the cluster size, indicating that the cluster of pixels is purely due to the charge sharing, namely, cross talk or noisy pixels are not presented. The bins 11ke and 15ke in the fig. 4.11(b) are discrete because the binning of the spectrum is smaller than the resolution of large ToT. Its is a compromised choice to resolve the distribution of small signals (mind the non-linear ToT-to-charge relation).

The signal spectra of all the clustered events are fit to the convolution of a Landau distribution folded with a Gaussian distributions to locate the MPV, as shown in fig. 4.12. According to the fits, the MPV of the 507 μm thick unirradiated diamond is 17200 electrons, and the MPV of the 542 μm diamond irradiated by 5×10^{15} p/cm^2 of 25 MeV protons is 4848 electrons. The uncertainty of the signal from the fit is rather negligible, so the main source of uncertainty is the 10% uncertainty from the charge calibration.

The MPV with respect to the bias voltage on the diamonds is shown in fig. 4.13. For the unirradiated diamond, the full charge collection is achieved at 150V. For the irradiated diamond, the MPV is smaller than the threshold 1200e while the bias is less than 400V, showing the tail of the truncated charge distribution, and 1000e is the middle of the first bin of the signal spectrum. When the bias is larger than 500V, the MPV grows with the increasing bias and reach to the maximum at 800V.

The measured data required for the SNR calculation are summarized in Table 4.3. The signal

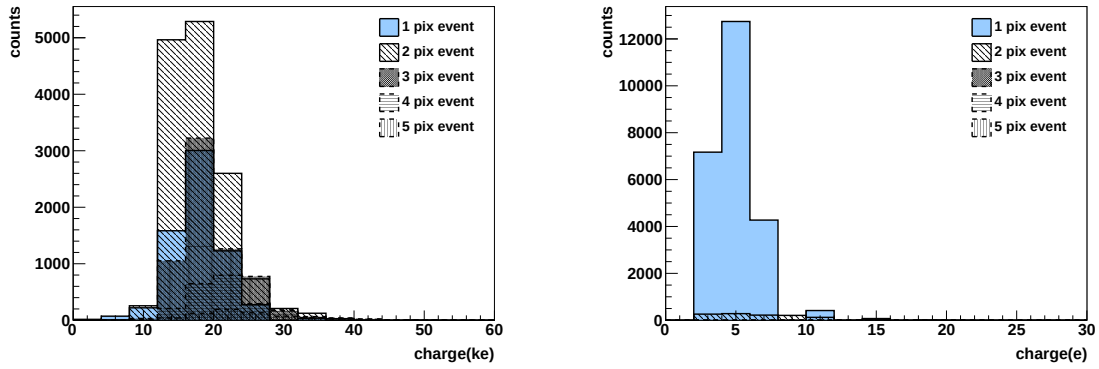

(a) (b)

Figure 4.11: Signal spectra of externally triggered ^{90}Sr source test separated by the contribution of one-, two-, tree-, four-, and five-pixel clusters. (a) Signal spectra of unirradiated diamond pixel detector DDL7, biased with 300 V. (b) Signal spectra of the diamond pixel detector DDL4, irradiated by 25 MeV protons. The fluence of irradiation is 5×10^{15} p/cm^2. The diamond is biased with 900 V.

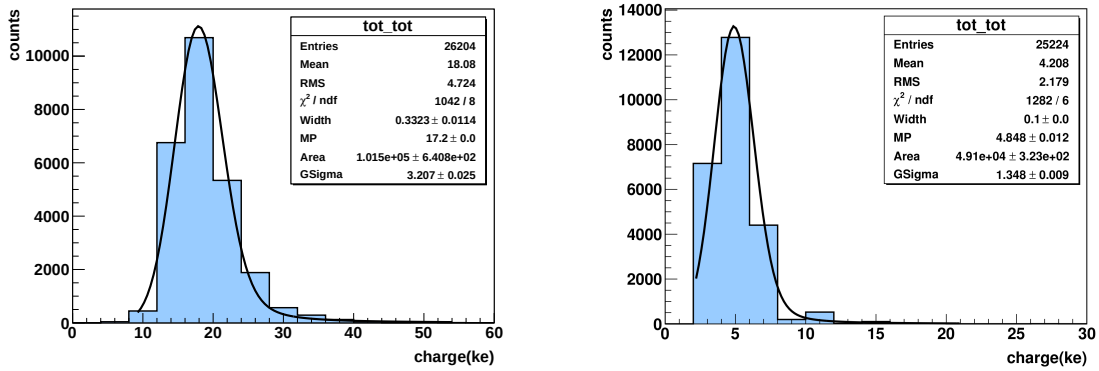

(a) (b)

Figure 4.12: Signal spectrum of externally triggered ^{90}Sr source test with Landau-Gaussian convolution fit to locate the MPV. (a) Fit for the signal spectrum of unirradiated diamond, DDL7, which is biased with 300 V. (b) Fit for the signal spectrum of the diamond DDL4, irradiated by 25 MeV protons with a fluence of 5×10^{15} p/cm^2, which is biased with 900 V. "Width" is the full-width-half-maximum of the landau distribution. "MP" is the most probable value. "Area" is the area under the Landau-Gaussian curve. "GSigma" is the sigma of the Gaussian distribution.

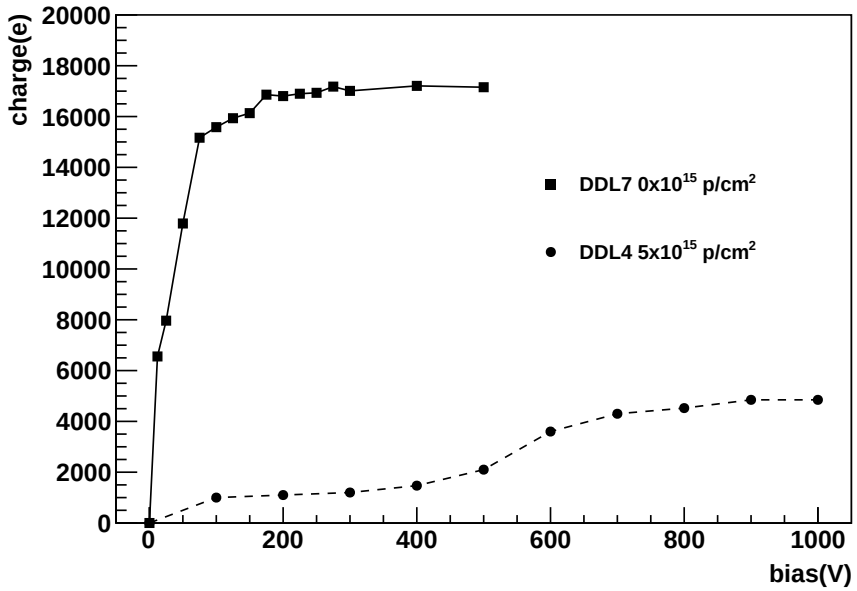

Figure 4.13: Most probable value of the signal spectra with respect to bias voltage on the unirradiated diamond (DDL7) and irradiated diamond (DDL4). The square and circle markers are for DDL7 and DDL4, respectively. The lines are to guide the eye. The uncertainty of the MPV is 10% from the uncertainty of charge calibration.

is the MPV determined in fig. 4.12 the the 10% uncertainty from the calibration. The noise of a signal pixel is measured by the threshold scan, see Table 4.1. However the uncertainty of the noise is not only the pixel-to-pixel variation but also the 10% uncertainty from the injection capacitance. The two uncertainties are added up in quadrature. These measurement results will be compared to the estimation by models and simulations in chapter 8.

Table 4.3: Measured signals, noise, and SNR for the unirradiated (DDL7) and the irradiated diamond (DDL4).

diamond	DDL7	DDL4
thickness	507 μm	542 μm
irradiation	0	5×10^{15} p/cm^2
MPV	(17200±1720) e	(4848±485) e
noise	(135±17) e	(135±15) e
SNR for 100 μm of sensors	25.15±4.02	6.62±0.98

Chapter 5

Signal

The particle passes through the sensor, deposits energy by ionization, creating electron and hole pairs the movement of which induces a signal on the electrode. In this chapter, the theory of the energy loss by radiation in matter is reviewed, and then are applied to estimate the signal generated in diamond and silicon. The energy loss by heavy charged particles is introduced in section 5.1, by photons in 5.2.

5.1 Energy loss by heavy charged particles

Charged particles passing through matter lose energy due to collisions with atoms. For particles whose ratio between momentum and mass ($\beta\gamma = p/mc$) is between 0.1 and 500, the energy loss is mainly by ionization and a small fraction of atomic and collective excitation. If $\beta\gamma$ is larger than 500, radiative processes like bremstrahlung and cherenkov radiation take place (see fig. 5.1). In addition, particles produced in the LHC experiments usually have $\beta\gamma$ between 0.1 and 500. The ionization energy loss by heavy charged particles, e.g. muons, pions, protons, and kaons, is discussed in detail below.

5.1.1 Average energy loss

The average energy loss of particles traversing matter was first derived by Bethe [48], based on the scattering of a heavy charged particle off a bounded electron and the subsequent atomic excitations. The expression is the Bethe-Bloch formula [30]:

$$-\left\langle \frac{dE}{dx} \right\rangle = Kz^2 \frac{Z}{A}\frac{1}{\beta^2}\left[\frac{1}{2}\ln\frac{2m_e c^2\beta^2\gamma^2 T_{max}}{I^2} - \beta^2 - \frac{\delta(\beta\gamma)}{2}\right] \tag{5.1}$$

Note that $-\langle dE/dx\rangle$ is the stopping power, that is defined as the energy loss ($-\Delta E$) per material distance ($x = d\cdot\rho$), where d is the path length and ρ is the density of the material. The other variables used in eq.(5.1) are listed in Table 5.1. T_{max} is the maximum amount of energy that can be transfered from the incident particle to an electron:

$$T_{max} = \frac{2m_e c^2\beta^2\gamma^2}{1 + 2\gamma m_e/M + (m_e/M)^2} \tag{5.2}$$

The stopping power versus $\beta\gamma$ of the passing particle is shown in fig. 5.1. Experiment shows that the stopping power is nearly identical for various material types [30], and the average energy loss ($-\langle dE/dx\rangle \cdot d\cdot\rho$) is proportional to the density of the material. As a function of

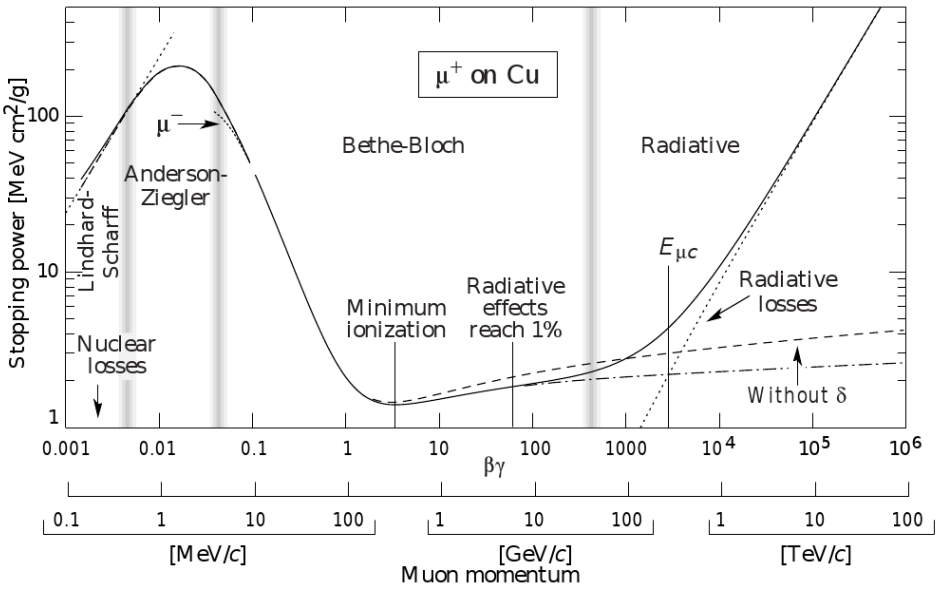

Figure 5.1: Stopping power of the charged particles as a function of $\beta\gamma$. It was measured by the energy loss of a muon in copper [30].

Table 5.1: Variables used in the equations of energy loss

variable	definition	units or value
K/A	$4\pi N_A r_e^2 m_e c^2$	0.307 MeVcm^{2}g^{-1}
N_A	Avogadro's number	6.022×10^{23} mol^{-1}
r_e	classical electron radius $e^2/4\pi\varepsilon_0 m_e c^2$	2.817 fm
$m_e c^2$	electron mass $\times c^2$	0.511 MeV
M	mass of incident particle	
z	number of charge of the incident particle	
Z	atomic number of absorber	
A	atomic mass of absorber	gmol^{-1}
I	mean excitation energy	eV
T_{max}	maximum energy transfer	keV
T_{cut}	restricted energy deposition	keV
$\hbar\omega_p$	plasma energy ($\sqrt{4\pi N_e r_e^3}\ m_e c^2/\alpha$)	$\sqrt{\rho\langle Z/A\rangle}\times$ 28.816 eV (ρ in g cm^{-3})
α	fine structure constant	1/137.036
N_e	electron density	$(r_e)^{-3}$
d	thickness of the detector	µm
ρ	density	g cm^{-3}

Table 5.2: Parameters for the density corrections of diamond and silicon. The diamond data was derived from [49]. The Si data is taken from the reference [50].

parameter	parameterization	Diamond	Si
C	$-2\ln(I/\hbar\nu_p) - 1$	-2.50	-4.44
a	$(-C - 4.606X_0)/(X_1 - X_0)^m$	0.269	0.149
m	for I < 100eV, $a \approx 3.0$	3.0	3.25
X_0	for C < 3.681, $X_0 = 0.2$	0.2	0.2
X_1	for I < 100eV, $X_1 = 2.0$; for I > 100eV, $X_1 = 3.0$	2.0	2.87

$\beta\gamma = p/m$ where p is the momentum and m is the mass of the particle, $-\langle dE/dx\rangle \cdot d \cdot \rho$ is almost independent of the material traversed.

When the $\beta\gamma$ increases from 0.1 up to 3.5, the $-\langle dE/dx\rangle$ decreases with respect to $1/\beta^2$. The $1/\beta^2$ dependence is from the electromagnetic force between the particle and a bounded electron, which reflects the fact that heavy particle with higher speed traverses the matter in a shorter time, leading to smaller $-\langle dE/dx\rangle$.

$-\langle dE/dx\rangle$ reaches a minimum around 1.5 MeV cm^2 g^{-1} where the $\beta\gamma$ is between 3 and 4. All the particles having $\beta\gamma$ more than 3 are called the minimum ionizing particle (MIP). A MIP can be considered as the worst case of signal production, so the energy depoistion by a MIP is an indicator of the detector performance.

After the MIP point, the $-\langle dE/dx\rangle$ grows with $\ln\beta^2\gamma^2$ (the relativistic rise), because of the transverse extension of electric field of the charged particle when its energy is at the relativistic regime, leading to more energy loss. However, the atoms of the material are polarized by the extending electric field at the same time, so the screening effect inhibits the extension of the electric field, and suppresses the logarithmic rise. To correct for the suppression, the *Density Correction*, $\delta(\beta\gamma)$, is introduced to the eq.(5.1).

Density correction At very high energies, the following approximation can be applied for density corrections:

$$\frac{\delta(\beta\gamma)}{2} \to \ln\left(\frac{\hbar\omega}{I}\right) + \ln(\beta\gamma) - \frac{1}{2} \tag{5.3}$$

Then $-\langle dE/dx\rangle$ grows with $\ln(\beta\gamma)$ in stead of $\ln\beta^2\gamma^2$, and the mean excitation energy I is replaced by the plasma energy, $\hbar\omega_p$. Since $\hbar\omega_p$ is proportional to the square root of electron density ($\sqrt{N_e}$), the correction is larger for the material with higher density, which represents nature of the screening by polarized electron clouds.

The concrete theoretical derivation for $\delta(\beta\gamma)$ had never been done. Sternheimer and Peierls summarized the measurements on density effects for condensed matter and gases, and obtained a general parameterization for all kinds of materials [49]:

$$\delta(\beta\gamma) = \begin{cases} 2(\ln 10)X - C & \text{if } X \geq X_1; \\ 2(\ln 10)X - C + a(X_1 - X)^m & \text{if } X_0 \leq X < X_1; \\ 0 & \text{if } X < X_0; \end{cases} \tag{5.4}$$

Where X is defined as $\log(\beta\gamma)$. The parameters X_0, X_1, a and m for diamond ans Si are

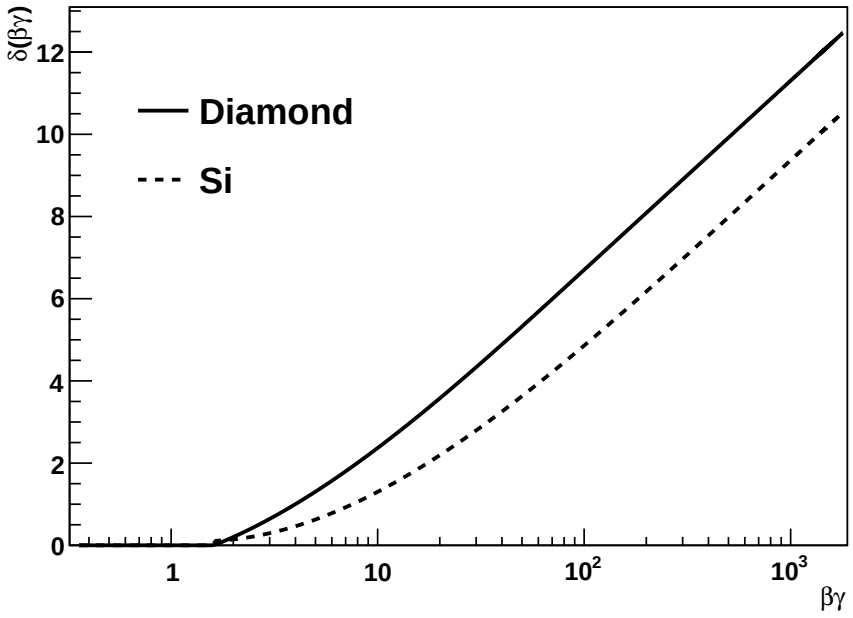

Figure 5.2: Density correction δ with respect to the $\beta\gamma$ of the particle for diamond (solid line) and Si (dashed line).

summarized in Table 5.2. The parameters for diamond are calculated using the recipe given in [49], which is based on the atomic number, density and plasma energy of the material. The parameters for Si were carefully investigated and given in [50]. Using the parameters, the $\delta(\beta\gamma)$ of diamond and Si are shown in fig. 5.2. The $\delta(\beta\gamma)$ for diamond is larger than for Si, because of its larger density, as expected.

Restricted energy loss The derivation of the Bethe-Bloch formula (eq.(5.1)) assumes that the absorber material is infinitely thick, and the energy loss from the charged particle is completely absorbed. In reality, the sensor of the pixel detector is a few hundred μm thick. As the particle collides with the electron, the secondary electrons that carry a portion of the energy loss can drift or defuse (the number of portion depends on the scattering angle), leaving the sensor before their energy is completely absorbed. Therefore, the actual *energy deposition*, which is finally detected, is less than the energy loss expected by eq.(5.1). To correct for the discrepancy between *energy loss* and *energy deposition*, the Bethe-Bloch formula is further modified to the *restricted energy loss rate*:

$$-\left\langle \frac{dE}{dx} \right\rangle_{res} = Kz^2 \frac{Z}{A} \frac{1}{\beta^2} \left[\frac{1}{2} \ln \frac{2m_e c^2 \beta^2 \gamma^2 T_{cut}}{I^2} - \frac{\beta^2}{2} \left(1 + \frac{T_{cut}}{T_{max}} \right) - \frac{\delta}{2} \right] \tag{5.5}$$

where T_{cut} is the maximum energy transfer that can be deposited in the thin sensor. The range of T_{cut} is $T \leq T_{cut} \leq T_{max}$. The secondary electrons with kinetic energy larger than T_{cut} leaks out of the sensor before all the energy are deposited.

T_{cut} depends on the density and the thickness of the sensor. In principle T_{cut} is higher for material with higher density since the energy loss per path length is $-\langle dE/dx \rangle_{res} \cdot \rho$. Thicker

Table 5.3: Comparison of measured and calculated energy loss in diamond. MPV is the most probable value. $-\langle dE/dx\rangle_{res} \cdot x$ is the restricted energy loss. The measurement of the 395 μm thick diamond using pixel readout and 120 GeV pion beam is from [51]. For the 507 μm thick diamond, the pad readout is used and the measurement is done using the β-ray from the ^{90}Sr radioactive source.

sensor	diamond 395 µm	diamond 507 µm
particle	120 GeV pion	β-ray from ^{90}Sr
MPV measurement [keV]	171.6	225.3
MPV calculation [keV]	171.0	225.7
$-\langle dE/dx\rangle_{res} \cdot x$ measurement [keV]	195.190	253.6
$-\langle dE/dx\rangle_{res} \cdot x$ calculation [keV]	195.110	255.1
Matched T_{cut} [keV]	120	137

Table 5.4: Comparison of measured and calculated energy loss in diamond. MPV is the most probable value. $-\langle dE/dx\rangle_{res} \cdot x$ is the restricted energy loss. The data are from the publication by J.F.Bak et al. in [52].

sensor	Si 100 µm	Si 174 µm	Si 290 µm
particle	2 GeV pion	2 GeV pion	2 GeV pion
MPV measurement [keV]	25.50	45.00	78.33
MPV calculation [keV]	24.91	44.77	77.23
$-\langle dE/dx\rangle_{res}$ measurement [keV]	28.31	49.34	84.11
$-\langle dE/dx\rangle_{res}$ calculation [keV]	28.27	49.40	83.24
Matched T_{cut} [keV]	15	18	20

sensors have higher T_{cut}, too, because the secondary electrons require higher kinetic energy to penetrate the sensor before leaving it.

In practical measurements the average energy loss depends on the noise of the measurement and the systematic error of the analysis method, e.g. charge loss in pixel detectors due to charge sharing. The energy loss spectrum is not symmetric (see fig. 5.4), such that uncertainties alter the average energy loss, too. In this thesis T_{cut} is extrapolated by matching the calculation to the measured energy loss, see Table 5.3 and Table 5.4. For example, the energy loss in 395 µm sCVD diamond was measured by Mathes [51], giving the T_{cut} =120 keV, therefore the T_{cut} of 200 µm diamond is assumed to be 60 keV. The energy loss spectrum of 200 µm Si was measured by Bak [52], and according to the spectrum the T_{cut} has to be 20 keV to give the same $-\langle dE/dx\rangle_{res}$. The critical parameters for the $-\langle dE/dx\rangle_{res}$ (eq.(5.5)) calculation is summarized in Table 5.5.

Fig. 5.3(a) and fig. 5.3(b) shows the calculated average energy loss $-\langle dE/dx\rangle$ and restricted energy loss rate $-\langle dE/dx\rangle_{res}$ in 200μm of diamond and Si as a function of the $\beta\gamma$ of the incident particle, respectively. The amount of $-\langle dE/dx\rangle_{res}$ lost by MIP in diamond and Si are compared to the experimental results in Table 5.3 and Table 5.4, respectively. The measured and calculated energy loss show good agreement to each other.

The influence of the critical parameters are discussed below:

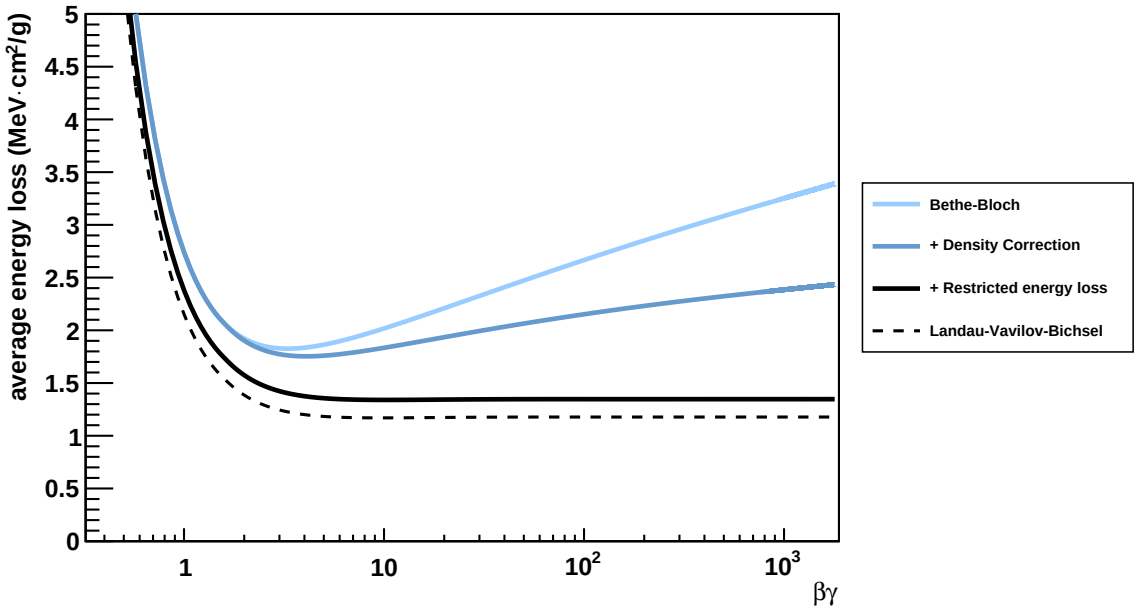

(a)

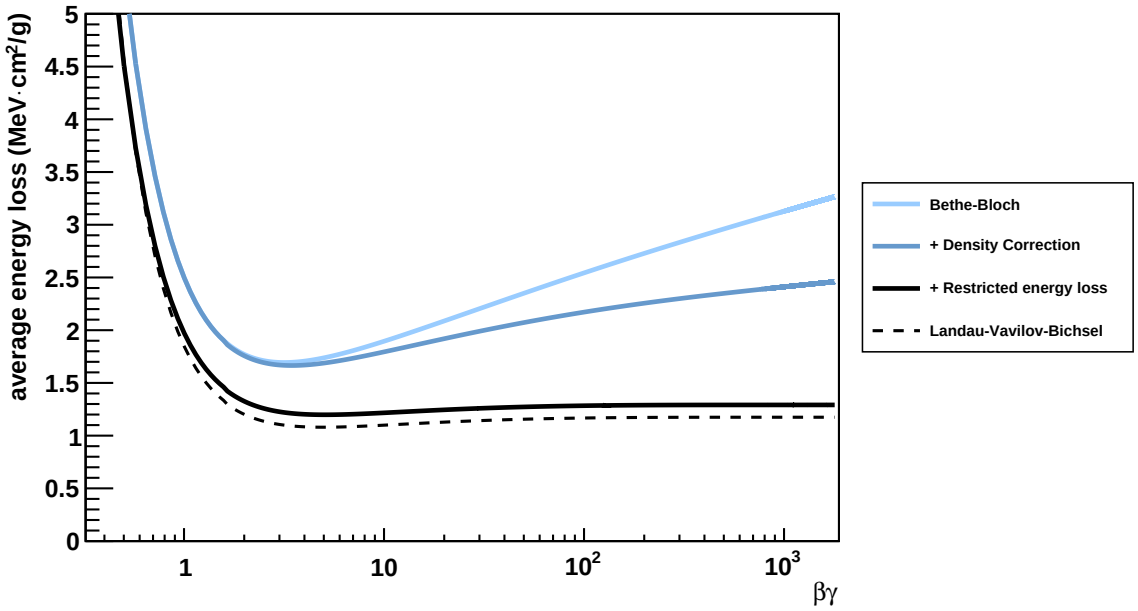

(b)

Figure 5.3: Energy loss in sensors with 200 µm of thickness. (a) diamond. (b) Si. The "Bethe-Bloch" curve is calculated by eq.(5.1) without density correction. "+ Density Correction" means eq.(5.1) with $\delta(\beta\gamma)$ calculated by eq.(5.4). "+Restricted energy loss" is calculated by eq.(5.5), with T_{cut} = 60 keV for 200 µm of diamond. "Landau-Vavilov-Bichsel" is the most probable value of the energy loss spectrum calculated by eq.(5.9).

Table 5.5: Parameters for restricted energy loss rate (eq.(5.5)). T_{cut} for 200 μm are extracted by matching the calculation to the measured data listed in Table 5.3 and Table 5.4.

parameter	definition	diamond	Si
I	mean excitation energy	81 eV	174 eV
T_{cut}	restricted energy deposition cut	60 keV	20 keV
δ	density correction at $\beta\gamma = 100$	3.2	2.2
δ	density correction at $\beta\gamma = 7.16$	1.84	0.95
ρ	density	3.53 g cm^{-3}	2.33 g cm^{-3}

excitation energy Comparing the Bethe-Bloch calculations without density correction for diamond and Si, the curves shows that the $-\langle dE/dx\rangle$ is larger in diamond than in Si. The reason is that the mean excitation energy I is smaller in diamond (81 eV) than in Si (174 eV).

density correction The density of diamond (3.53 g cm^{-3}) is larger than that of Si (2.33 g cm^{-3}), so the density correction $\delta(\beta\gamma)$ in diamond is higher than in Si for high $\beta\gamma$ particles. The influence from the excitation energy I and the density correction δ cancel out, and finally the $-\langle dE/dx\rangle$ in diamond and Si are similar.

restricted energy loss High T_{cut} for diamond means that diamond can preserve more energy loss inside the sensor. For the $\beta\gamma > 100$, the $-\langle dE/dx\rangle_{res}$ of diamond is 1.18 MeVcm^2/g, slightly higher than the $-\langle dE/dx\rangle_{res}$ of silicon 1.17 MeVcm^2/g.

summary The actual energy deposition per unit length is given by the result of calculation $\langle dE/dx\rangle_{res}$ multiplied by the density of the material. The energy deposit in diamond per unit path length is larger than in silicon mainly due to the larger density. The ratio for a 1 GeV incident pion ($\beta\gamma$=7.2) is

$$\frac{\left\langle \frac{dE}{dx} \right\rangle_{diamond}}{\left\langle \frac{dE}{dx} \right\rangle_{Si}} = \frac{472 \frac{eV}{\mu m}}{281 \frac{eV}{\mu m}} \approx 1.68 \tag{5.6}$$

5.1.2 Energy loss spectrum

Heavy charged particles passing through matter lose their energy in small steps by continuous single collisions with atoms. The energy loss fluctuates, so the total energy loss to the material is an energy spectrum. There are two types of fluctuations: the fluctuations of the number of collisions, which follows the Poisson statistic, and the fluctuations of the energy loss of a single collision, for which the ionization and collective excitations must be taken into account.

The energy loss distribution in thin detectors was first derived by Landau [53], so the spectrum is called the Landau distribution. The Landau distributions of Si sensors with various thicknesses are illustrated in fig. 5.4 [30]. The energy loss spectrum is asymmetric, and conventionally, is characterized by the most probable value (MPV) and the full width of half

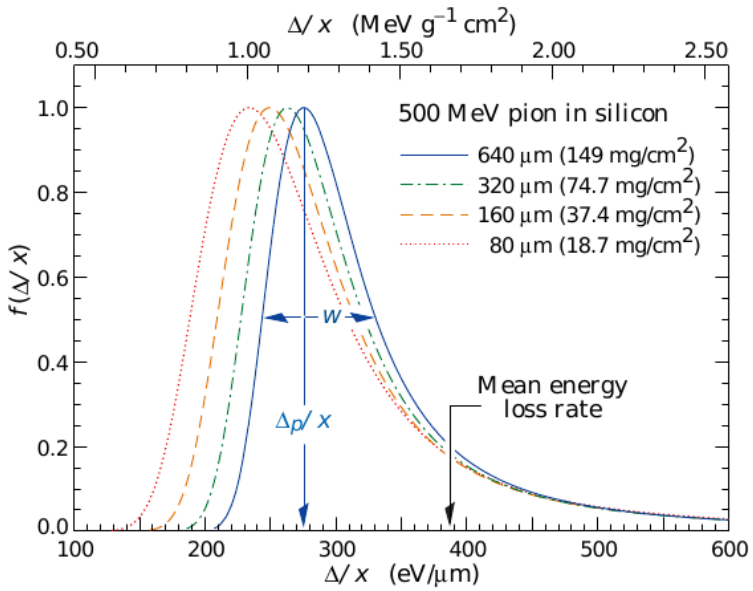

Figure 5.4: Landau distribution of Si sensors with various thicknesses, simulated for 500 MeV traversing pion, showing that the energy loss distribution is more symmetric for thicker sensors [30].

maximum (FWHM). The high energy tail of the Landau distribution is from the δ-electrons with large deflection angle and low velocity which deposit large amount of energy. The MPV and FWHM of the Landau distribution strongly depend on the thickness of the absorber. Thin sensors tends to give lower MPV and wider energy spectrum.

Further corrections of the energy loss spectrum in thin silicon detectors were made by Bichsel [54]. "Thin sensor" means that the thickness of the detector (d) must be small compared to the range of the particles. The criterion of thickness is defined by the Vavilov parameter:

$$\kappa = \xi / T_{max} \tag{5.7}$$

where T_{max} is the maximum energy transfer defined in eq.(5.2), ξ is the Landau parameter:

$$\xi = \frac{K}{2}\frac{Z}{A}\frac{d}{\beta^2} \tag{5.8}$$

Where d is the material length $x \cdot \rho$. For thin sensors with $\kappa < 0.6$, the MPV of the energy loss spectrum (Δ_p) is calculated by the following Landau-Vavilov-Bichsel formula:

$$\Delta_p = \xi \left[\ln \frac{2m_e c^2 \beta^2 \gamma^2}{I} + \ln \frac{\xi}{I} + j - \beta^2 - \delta(\beta\gamma) \right] \tag{5.9}$$

with j=0.2 and $\delta(\beta\gamma)$ given in eq.(5.4). The FWHM ω depends on the absorber thickness. $\omega = 4\xi$ is an upper limit estimation [54].

The Δ_p for 200 μm thick diamond and Si as a function of $\beta\gamma$ of the incident particle are plotted in fig. 5.3(a) and fig. 5.3(b), respectively, in comparison with the stopping power. The calculated numbers are compared to the real measurement in Table 5.3 and Table 5.4, showing that the calculation and measurements agree with each other.

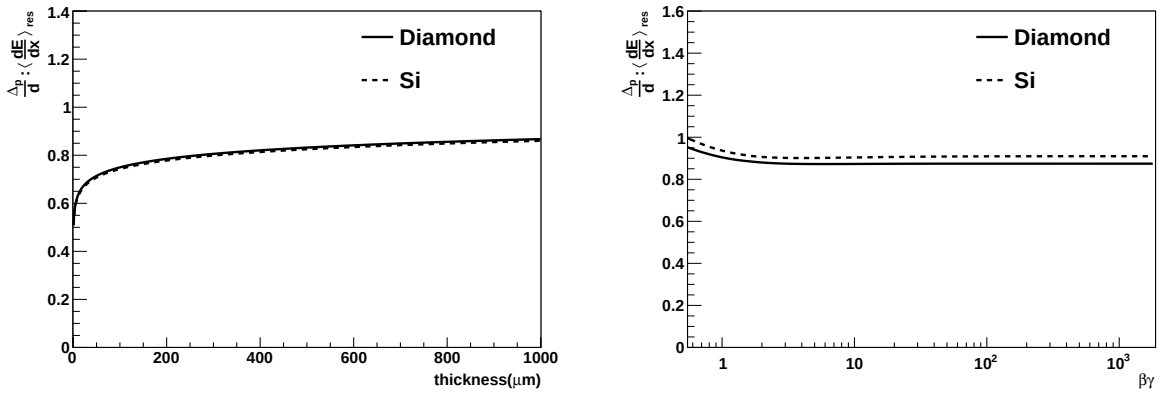

(a) (b)

Figure 5.5: Ratio between the Δ_p per unit path length (Δ_p/d) and the the restricted energy loss rate $-\langle dE/dx\rangle_{res}$ (a) As a function of detector thickness, calculated for incident particle with $\beta\gamma$=100. (b) As a function of $\beta\gamma$ of the incident particle, calculated for sensors with 200μm of thickness.

The Δ_p as a function of the detector thickness (see fig. 5.5(a)) shows that the Δ_p has a $a \ln d+b$ tendency, independent of material types. On the other hand, the ratio between the Δ_p/d and $\langle dE/dx\rangle_{res}$ remains 0.9 for both diamond and Si in the high energy regime (see fig. 5.5(b)). The result implies that both Δ_p and $\langle dE/dx\rangle_{res} \cdot d$ are applicable to represent the signal obtained from the sensor.

However, practically, the $\langle dE/dx\rangle_{res}$ and the FWHM of the energy loss distribution always differ from the theoretical predictions, because the electronic noise from the detector contributes to the width and changes $\langle dE/dx\rangle_{res}$, too. Instead, Δ_p can be measured precisely. Therefore, Δ_p is used to represent the signals in the following contexts.

For 1 GeV pion traversing diamond or Si ($\beta\gamma$=7.2), the ratio of Δ_p in 200 μm of diamond and silicon is

$$\frac{\Delta_p^{diamond}}{\Delta_p^{Si}} \approx 1.63 \tag{5.10}$$

5.1.3 Signals in diamond and silicon

The energy lost in the semiconductor sensor is transfered to the electrons of the atoms. In the energy band model, the electrons are raised from the valance band to the conduction band, such that the electron and hole pairs are generated. The signal is expressed in the number of electron and hole pairs:

$$N_{e/h} = \Delta_p \div \omega_{e/h} \tag{5.11}$$

Δ_p is given by eq.(5.9), the parameters of diamond and Si are listed in Table 5.1 and Table 5.5, and the signal created in a 200 μm sensor as a function of $\beta\gamma$ of the incident particle is shown in fig. 5.6.

Diamond has an advantage over Si in that its density is 1.5 times of Si (3.52 $\mathrm{g\,cm^{-3}}$ >

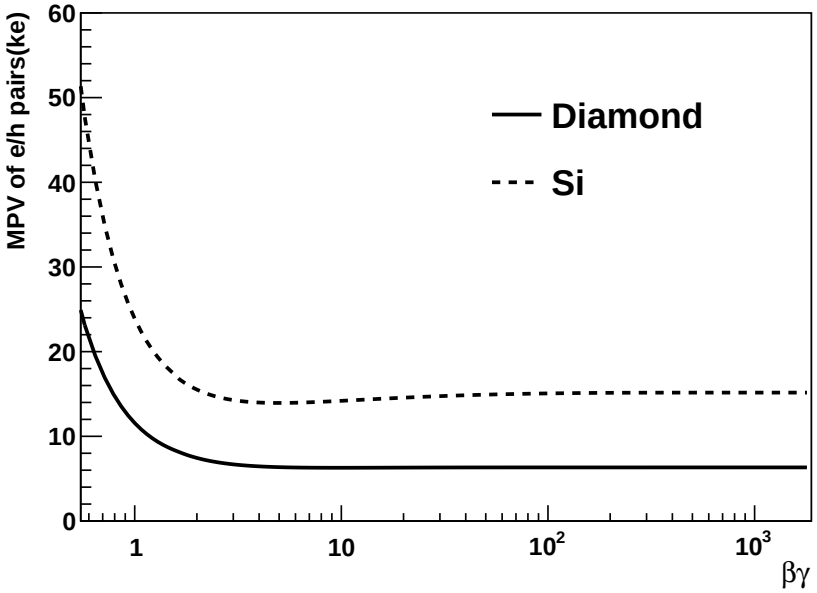

Figure 5.6: Most probable value of energy loss (MPV, Δ_p) versus $\beta\gamma$ of the charged particle in 200μm diamond and Si. The solid line is for diamond. The dashed line in for Si.

Table 5.6: Comparison of signal MPV in silicon and diamond. 0.1% X_0 is 121 μm in diamond, and 94 μm in Si.

	MIP		1 GeV pion	$\beta\gamma = 12.7$
sensor	diamond	Si	diamond	Si
200μm	6394	13949	6295	14031
$N_{e/h}$ per μm	32	70	31	70
0.1% X_0	3868	6556	3808	6595

2.33 g cm^{-3}), leading to more energy deposition. On the other hand, the drawback is that $E_{e/h}$ of diamond is 3.6 times of Si (13.1 eV > 3.61 eV), which means that large amount of energy deposition is required to generate signals.

The final results show that the 1 GeV pion can generate 6 300 electron and hole pairs in 200 μm of diamond, and 14 000 pairs in 200 μm of Si. The exact numbers for MIP and 1 GeV pion are summarized in Table 5.6.

Beside the expected sensor thickness 200 μm, thickness in unit of the radiation length X_0 must be considered, too, since the material budget of the pixel detector is characterized by the radiation length. The $0.1\%X_0$ is a common unit for estimations for pixel detector design. For diamond, $0.1\%X_0$ is 121 μm, for Si 94 μm. The signal created in $0.1\%X_0$ sensor is scaled from the data of 200 μm sensor thickness by:

$$N_{e/h,0.1\%X_0} = N_{e/h,200\mu m}\frac{0.1\%X_0}{200\mu m} \tag{5.12}$$

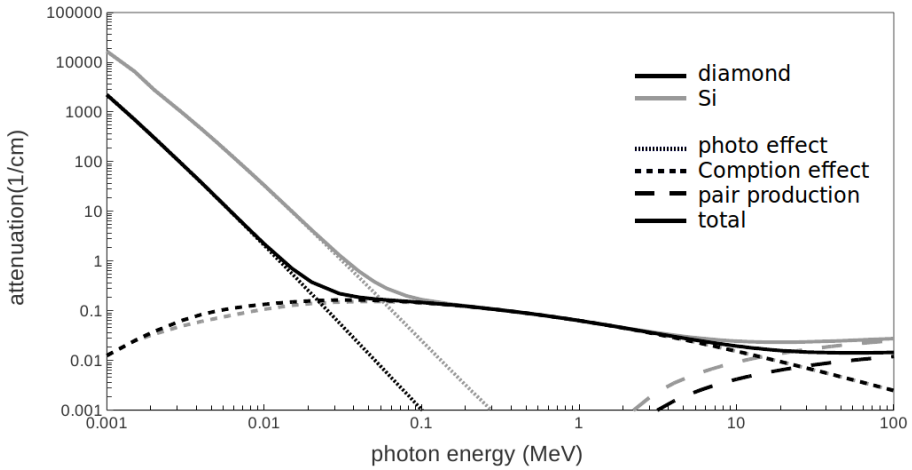

Figure 5.7: Attenuation coefficients for diamond and Si, shown by black lines and gray lines, respectively. The fine dot line shows the attenuation coefficient of photo effect. The coarse dot line is for Compton effect. The dashed line is for pair production. The solid line shows the total attenuation coefficient. The data are given by the NIST XCOM server [56].

The signal for $0.1\%X_0$ diamond is around 3800 e, for Si is around 6500 e. The diamond can benefit from its longer radiation length.

5.2 Energy loss by photons

Radioactive sources which emit γ-ray are often applied to calibrate the signals generated in the sensor. They are also applied to check the bump connections between the sensor and the readout pixel. Thus the interaction between photons and the material is reviewed below.

The difference between the traversing charged particles and the photons is that the energy of particles degrade while the number of particles remains the same, but the photons are absorbed and the intensity of the photon beam attenuates. The intensity I decreases exponentially with respect to the distance x, and is characterized by the attenuation coefficient μ:

$$I = I_0 e^{-\mu x} \tag{5.13}$$

The attenuation has three origins: photo effect, Compton effect, and pair production. The coefficient μ is proportional to the scattering cross sections σ of the various interactions:

$$\mu = \mu_{photo} + \mu_{compton} + \mu_{pair} = \frac{\rho}{uA}(\sigma_{photo} + \sigma_{compton} + \sigma_{pair}) \tag{5.14}$$

where u ($= 1.660 \cdot 10^{-24}$ g [55]) is the atomic mass unit, A is the relative atomic mass of the absorber material. The cross sections of various interactions strongly depends on the atomic number (Z) of the absorber and the photon energy (E_γ). Fig. 5.7 shows the attenuation coefficient of silicon and carbon. Each interaction between photon and material is explain below:

Photo effect The photo effect dominates for E_γ in the range of several 10 keV. The photon energy is transfered to the electron of the atom, raising the electron of the atom from the valence to the conduction band, so the electron-hole pairs for the signals are created.

The energy spectrum is a discrete peak, smeared with a Gaussianly distributed noise from the detector. Such a spectrum is useful for calibration of the pixel detector readout.

Compton effect At E_γ the MeV range, Compton scattering dominates the interaction between photon and material, as shown in fig. 5.7. Compton scattering is an inelastic scattering, which means that the photon transfers part of its energy to an electron while being deflected.

The possible energy transfer shows a continuous spectrum. It starts with zero and has a sharp maximum at the so called Compton edge:

$$E_{e,max} = \frac{h\nu^2}{m_e c^2 + h\nu} \tag{5.15}$$

The deflected photon can continue on several inelastic scattering, until its energy is low enough to be absorbed by photo effect. Hence, the spectrum of the Compton scattered photon requires subtle analysis. For calibration or tests of the pixel detector, the spectrum of photo effect is more useful than that of Compton effect. Note that the Z of diamond (Z=6) is less than that of Si (Z=14), meaning that the Compton scattering starts to dominate in diamond at the tens of keV range, which is the range of commonly used radioactive sources, e.g. ^{241}Am and ^{107}Cd. Therefore, the calibration of diamond sensor is more difficult than of silicon ones.

Pair production For high energy photons with E_γ more than 1 MeV, the pair production start to take place. The photon converts into electron and positron via the interaction with the nucleus of the traversed matter. Pair production completely dominate the interaction at the GeV range. Usually it is hard to be observed in the laboratory, but significant in the collider experiments.

Chapter 6

Radiation Damage

The signal generated in the sensor deteriorates because of the radiation damage. Other properties such as leakage current and doping concentration of silicon are also influenced by the radiation damage, resulting in increasing noise or difficulties of sensor operation. The mechanism of radiation damage and the impacts on the sensor properties are reviewed in section 6.1. Then the signal loss in diamond versus the radiation fluence is measured. The experimental methods and results are discussed in section 6.2. Based on the method developed in section 6.2, the signal loss in diamond and silicon are compared in section 6.3 and section 6.4.

6.1 Literature review

6.1.1 Mechanism, defects, and impacts

The radiation damage can be divided into two categories: bulk defects and surface defects. The former are caused by the displacement of the atoms in the lattice. The latter include all the defects at the dielectric covers and inter-surface region. The most relevant surface damage is the increase of charges at the oxide layer of the MOSFET readout electronics. However, in the high radiation environment, bulk damage dominates the electrical properties of the sensor, so the bulk damage is focused in the following contexts.

Mechanism

Bulk damage by energetic particles is caused mainly by displacing an atom out of the lattice, resulting in a interstitial and a left over, called vacancy. The first displacing atom is called the primary knock on atom (PKA).PKAs can and often will knock out other atoms, and an interstitial and a vacancy is called a Frenkel pair. Both interstitial and vacancy can migrate through the lattice, collide with atoms continuously, forming point and cluster defects (see fig. 6.1). The minimum energy to remove a silicon (Si) atom from the lattice is about 25 eV [27], for diamond is 43 eV [26]. Along the path of recoils, the energy of the atom is lost in 2 ways: one is by ionization as described in chapter 5.1, the other one is by further displacements. The latter one is the Non-Ionizing Energy Loss (NIEL). The ionization energy loss is fully reversible, but the damage by NIEL is not. For recoil energies more than 5 keV [57], a dense cluster of defects (disordered regions of defects) is formed at the end of the recoil path, as shown in fig. 6.1. Both point defects along the path and clustered defects at the end are responsible for the change of the electrical properties of the material.

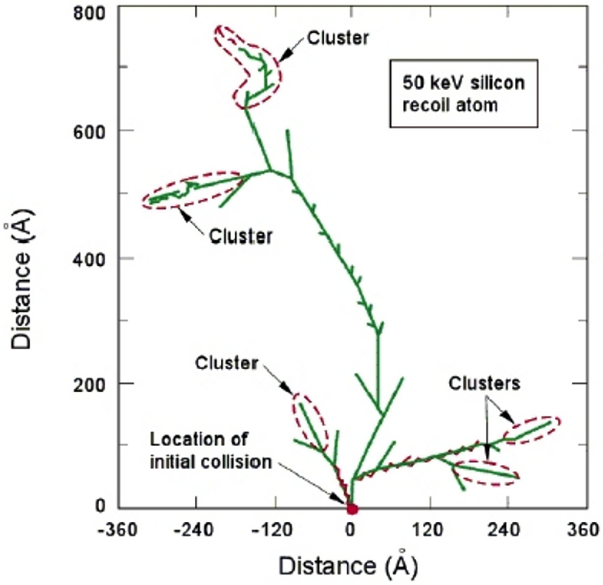

Figure 6.1: Monte Carlo simulation of a recoil-atom track [58].

Defects

Point defects are illustrated in fig. 6.2. The defects are combinations of interstitials (by either domestic or foreign atoms), replacements, and vacancies. The consequences can be divided into two categories: (a) change of the space charge concentration due to interstitials and vacancies, (b) formation of additional energy levels in the band gap. Consequence (a) has more severe impacts on devices with doping, e.g. Si diode. The influence from consequence (b) can happen to all kinds of materials, introducing effects related to the generation and annihilation of charge carriers, e.g. leakage current and trapping.

The defects with deep energy levels can act as generation/recombination centers (as shown in fig. 6.3 (a) and (b)). The electron and hole pairs can be created by thermal energy or light, so the leakage current increases. The additional level can also capture and emit charge carriers, affecting the number of signal charge carriers (as fig. 6.3(c)), or alter the effective doping concentration and space charge (as fig. 6.3(d)).

Most of the primary defects created by radiation are mobile, and the actual position of the defect states at the energy band evolves with time. Annealing was observed in Si devices, and is investigated thoroughly by the Si community [57][60]. The leakage current decreases with time [60]. The effective doping concentration first decreases, which indicates that the number of defects reduces, until a minimum (beneficial annealing). Then it rises again and saturates, which indicates that stable defects are formed (reverse annealing). Higher temperature speeds up the annealing. Therefore, irradiated Si sensors should be kept at low temperature environments to prevent reverse annealing. However, there was no systematic study on the trapping/charge collection effects with respect to annealing. The reason was that the charge collection can be easily increased by applying higher bias voltage on the sensor, so that the

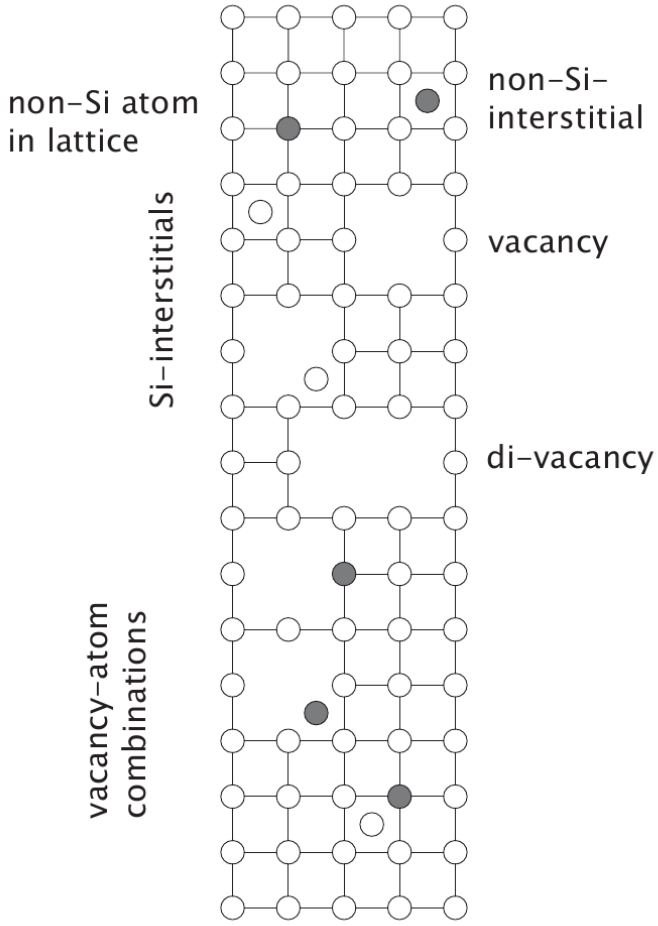

Figure 6.2: Illustration of defects [59].

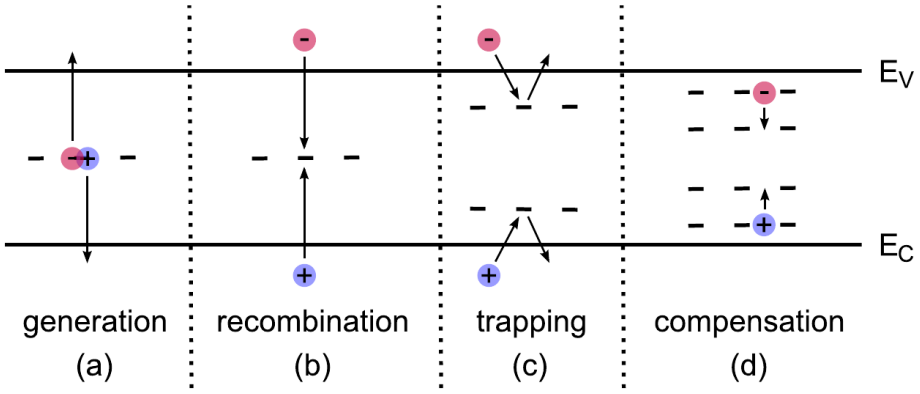

Figure 6.3: Intermediate energy levels induced by the dislodge of atoms can (a) help in the creation of thermal charge carriers, (b) act as recombination centers, (c) temporarily trap charges and (d) alter the effective doping concentration [42].

annealing effect on trapping/charge collection was not significant.

In case of diamond, the influence from annealing is rather irrelevant, since leakage current in diamond is tiny, and diamond sensor is not doped. The trapping/charge collection of irradiated diamond versus time was monitored by Zhao [61]. The result show that the performance remains stable for 5 years after irradiation. Therefore, while handling irradiated diamonds, annealing is not required to be considered.

Impacts

Finally, the defects and their impacts on macroscopic detector properties are summarized in Table 6.1 [60]. The review focus on the electrical properties which are directly related to the operation of the particle detectors, and the effects on diamond and Si are examined for each impact, too.

The structure of the diamond sensor is very simple, i.e. it does not have doping, and does not need junctions for depletion, so the impact of defects in diamond is rather simple compared to Si. The space charges in diamond can lead to polarization effects, suppressing the applied electric field, so the signal is reduced. The traps can catch the charge carriers, so the signal amplitude decreases as well. On the other hand, considering Si detectors, beside the space charge and trapping, they suffer from the increasing leakage currents and the change of doping concentration. The leakage current causes increasing electronic noise and power consumption, so the Si detector must be operated at low temperatures. The change of the doping concentration alters the electric field structure in the sensor, so higher bias is required to achieve full depletion after irradiation. To summarize, diamond is easier to operate in high radiation environment compared to Si.

To study the signal and noise of a pixel, the most important impacts are leakage current and trapping. They are reviewed in detail in the next two sections 6.1.3 and section 6.1.4.

6.1.2 Non-ionizing energy loss

The relation between the macroscopic properties of sensors and the irradiation fluence has been studied for Si in the past 20 years based on the Non-Ionizing Energy Loss (NIEL) hypothesis. The assumption of NIEL hypothesis is that the quantity of displacement damage is proportional to the NIEL, and the change of the electrical properties is proportional to the quantity of the displacement damage. The proportionality depends on the particle type and energy. The NIEL can be estimated analytically by calculating the displacement damage cross section $D(E)$ [62]:

$$D(E) = \sum_{\nu} \sigma_{\nu}(E) \cdot \int_{0}^{E_R^{max}} f_{\nu}(E, E_R) P(E_R) dE_R \tag{6.1}$$

Where the index ν indicates all possible interactions between the incident particle with energy E and the atom which leads to displacement of the lattice, σ_{ν} is the cross section corresponding to each interaction, $f_{\nu}(E, E_R)$ is the probability for generating a PKA with the recoil energy E_R by a particle with energy E. $P(E_R)$ is the portion of the recoil energy that turns into displacement damage (Lindhard partition function [63]). The displacement damage cross section $D(E)$ is proportional to the NIEL by the relation:

Table 6.1: Summary of point defects and their impacts on the detector properties [60].

defect	electrical property	Impact	diamond	Si
generation center	leakage current	Thermal runaway, higher noise	no	yes
shallow traps	space charge distribution	higher biasing electric field	no	yes
deep traps	resistivity	larger power consumption	no	yes
surface and bulk defects	space charge distribution	polarization	yes	no
shallow/deep traps	trapping	less charge collection efficiency	yes	yes
Donor/acceptor removal	effective doping concentration	depletion voltage must increase	no	yes
energy levels in the band gap	carrier freeze out	no depletion zone	no	yes

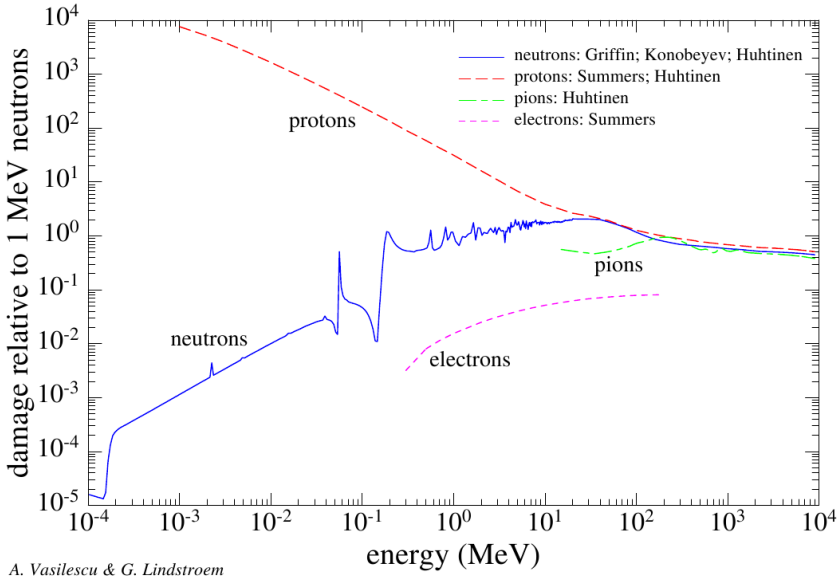

Figure 6.4: Damage cross section $D(E)$ in Si for various particles normalized to $D_n(1MeV)$=95 MeV mb [57]

$$D(E) = \frac{A}{N_A}\frac{dE}{dx}(E)\mid_{non-ionizing} \tag{6.2}$$

Where A is the atomic number, N_A is the Avogadro constant (6.02×10^{23} mol^{-1}). In case of Si with A=28 g mol^{-1}, the relation between $D(E)$ and NIEL is 100 MeV mb=2.144 keV cm^2 g^{-1} [64].

The displacement damage cross section $D(E)$ of Si by protons, pions, neutrons and electrons with energy from 10^{-4} to 10^4 MeV are shown in fig. 6.4. The damage is normalized to $D_n(1MeV)$=95 MeV mb. As shown in fig. 6.4, charged particles are more damaging than neutral ones at the low energy regime, because charge particles can scatter via electromagnetic interactions with atom nuclei that are partially screened by their electron clouds. They tend to produce more point defects and less clusters [65]. When the particle energy is more then 100 MeV, the damage by protons, neutrons, and pions is roughly the same.

To compare the amount of damage by different radiations with individual energy spectra $\phi(E)$, the hardness factor κ is defined by integrating the damage cross section $D(E)$ over the energy spectra, and normalize it with respect to the damage done by 1 MeV neutron:

$$\kappa = \frac{\int D(E)\phi(E)dE}{D(E_n = 1MeV)\int \phi(E)dE} \tag{6.3}$$

Here $D(E_n = 1MeV)$ is set to be 95 MeV mb [64]. Hence, the 1 MeV neutron equivalent fluence Φ_{eq} can be defined as:

$$\Phi_{eq} = \kappa\Phi = \kappa\int \phi(E)dE \tag{6.4}$$

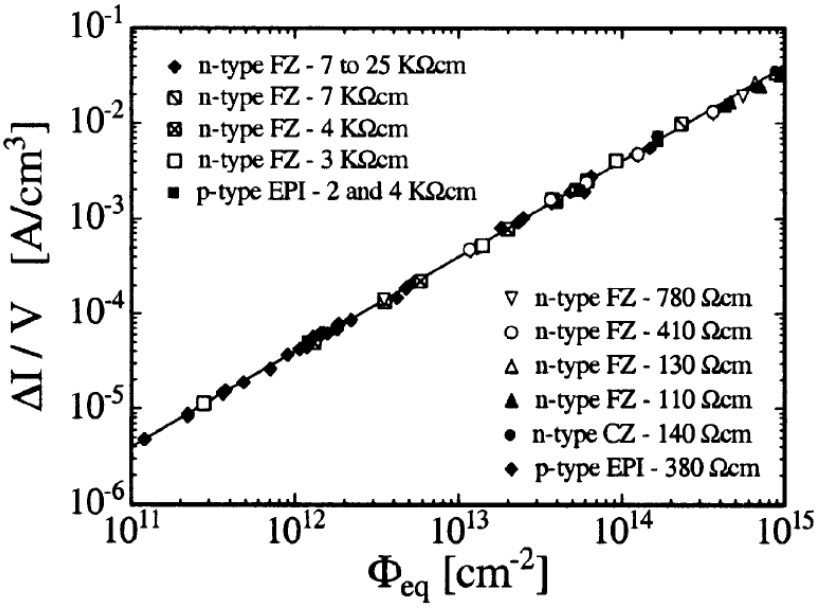

Figure 6.5: Fluence dependence of leakage current for various Si detectors. The current was measured in room temperature after annealing at 60°C for 80 minutes ($\alpha = (3.99 \pm 0.3) \times 10^{-17}$ A cm^{-1}) [66]

For monoenergetic irradiation sources, the damage factor can be found by scaling the damage cross section presented in fig. 6.4. For example, the κ of 24 GeV proton damage is 0.6 [57], for 25 MeV prton the κ is 1.85 [57].

Numerous experiments show that the leakage current versus irradiation agrees with the NIEL hypothesis (see fig. 6.5). The leakage current increases linearly as a function of the irradiation fluence. The amount of the measured leakage current lies on the same curve, if the fluence (Φ) is converted to the 1 MeV neutron equivalent fluence(Φ_{eq}) using eq. (6.4). Note that in these measurements, a standard annealing process was performed (heating at 60 °C for 80 minutes). The leakage current was measured at room temperature (20°C), and the bias on the sensor is large enough so that the volume leakage current saturates.

However, measurement of the effective doping (N_{eff}) concentration violates the NIEL hypothesis. Ruzin et al. [68] pointed out that charged particles (pions and protons) are less damaging than the prediction of $D(E)$ in oxygen rich FZ Si sensors, as shown in fig. 6.6. The simulation by Huhtinen [67] explained that the di-vacancy defect, which is the main contribution to leakage current generation centers, increases linearly with the NIEL. On the other hand, the generation of vacancy with oxygen atom, as well as other defects such as tri-vacancy and Phosphor interstitials, do not follow the NIEL hypothesis. The simulation result explains why the leakage current agrees with NIEL hypothesis, but the effective doping does not.

Although the experiments and simulation proved that the NIEL hypothesis is only applicable for the leakage current, the 1 MeV neutron equivalent fluence Φ_{eq} is still used as a standard unit to estimate the amount of radiation damage at the Large Hadron Collider. For Si sensors, the irradiation studies were focused on the leakage current and the effective doping concentration. The agreement between NIEL prediction and experimental results were carefully examined. On the other hand, the trapping or charge collection efficiency has not been systematically

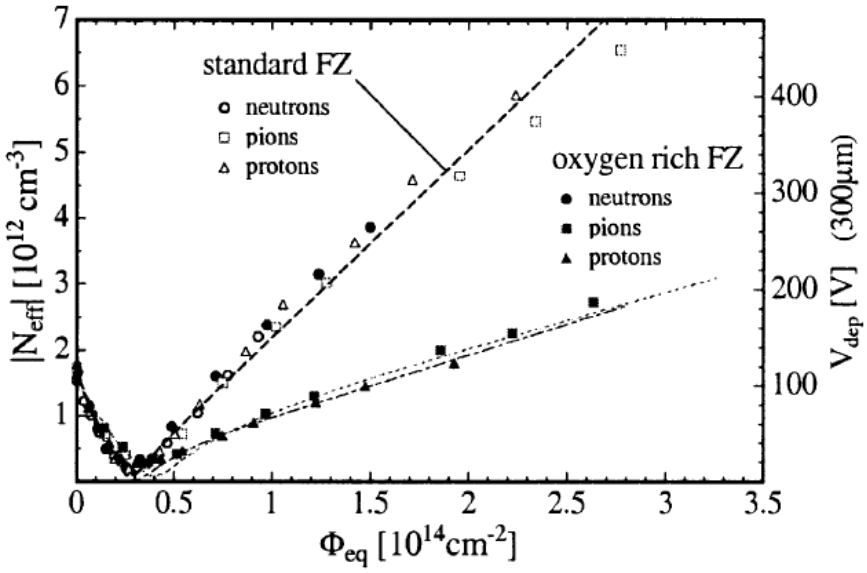

Figure 6.6: Particle dependence of the effective doping concentration $|N_{eff}|$ on standard Float Zone (FZ) and oxygen rich FZ Si detectors [67]. The protons and pions are more damaging in oxygen rich FZ Si than the prediction by NIEL hypothesis (the coarse dashed line), but the neutron damage on oxygen rich FZ Si and standard FZ Si agree with NIEL prediction instead.

investigated, since many parameters are involved, such as annealing, depletion, type inversion, so the experiment is rather complicated. Nevertheless, diamond does not have leakage current, does not need doping, meaning that the methodology to measure κ of NIEL hypothesis is not suitable for diamond. Besides, the functional behavior of trapping versus irradiation, which directly influences the signal charge collection, has never been systematically investigated with NIEL. To conclude, a general framework to describe the trapping as a function of radiation damage is required to compare the radiation-hardness of diamond and Si.

In the following formulation, the leakage current as a function of radiation fluence is calculated by the well-examined NIEL scaling principles, see section 6.1.3. The signal deterioration due to trapping is evaluated in terms of the mean free path of charge carriers in the sensor, see section 6.1.4.

6.1.3 Leakage current versus irradiation

The leakage current (I) per unit volume (V) can be described by the following formula, as indicated by fig. 6.5:

$$\frac{I}{V} = \frac{I_0}{V} + \alpha\Phi_{eq} \tag{6.5}$$

Where the constant α is equal to $\alpha = (3.99 \pm 0.3) \times 10^{-17}$ A cm^{-1} [66], if the current is measured at room temperature after annealing at 60°C for 80 minutes. Generally, I_0/V is tiny although it depends on the sensor quality.

Furthermore, the leakage current depends on the temperature, because the thermal energy

Table 6.2: Variables used in the derivations

variable	definition	units or value
sub index n	parameter of electrons	none
sub index p	parameter of positions	none
n	electron density	$\mathrm{C\,m^{-3}}$
p	position density	$\mathrm{C\,m^{-3}}$
x	drift distance	m
v	velocity	$\mathrm{m\,s^{-1}}$
τ	lifetime	s
λ	mean free path	m
λ_e	mean free path of electron	m
λ_h	mean free path of hole	m
$\vec{J}$	current density	$\mathrm{C\,m^{-3}\,s^{-1}}$
q	unit charge	1.602×10^{-19} C
$g(\vec{r}, t)$	generation term	$\mathrm{C\,m^{-3}\,s^{-1}}$
d	thickness of the detector	m

can excite electrons to create electron and hole pairs. The leakage current grows exponentially with respect to the increasing temperature, and their relation depends empirecally on the band gap (E_g). To scale the leakage current from a reference temperature T_{ref} to another temperature T (in the case of measurement presented in fig. 6.5, T_{ref} is 20°C), the following formula is applied :

$$I(T) = I(T_{ref}) \cdot R(T) \tag{6.6}$$

$$R(T) = \left(\frac{T}{T_{ref}}\right)^2 \cdot \exp\left[\frac{-E_g}{k_B}\left(\frac{1}{T} - \frac{1}{T_{ref}}\right)\right] \tag{6.7}$$

6.1.4 Collected charge versus irradiation

In this section, First, (a) the relation between the collected charge ($Q_{collected}$) and the mean free path (λ) will be derived. Then (b) the decrease of λ due to radiation damage will be described. Combining the theories of (a) and (b), the relation between the collected charge and the radiation damage is obtained. The symbols and definitions of all the used parameters are listed in Table 6.2.

Charge collection in sensors

The derivation for charge collection as a function of mean free path (λ) follows Zhao [61]. Mean free path λ is the average distance which an electron and and hole have drifted apart under an electric field E:

$$\lambda = \lambda_e + \lambda_h = v_n \tau_n + v_p \tau_p \tag{6.8}$$

$$v_n = -\frac{dx}{dt} \tag{6.9}$$

$$v_p = +\frac{dx}{dt} \tag{6.10}$$

The electrons and holes generated by the signal obey the charge conservation rule. The distribution of the charge versus space and time must fulfill the continuity equations [69]:

$$\frac{\partial n}{\partial t} = +\frac{1}{q} \nabla \cdot \vec{J}_n - \frac{n}{\tau_n} + g(\vec{r}, t) \tag{6.11}$$

$$\frac{\partial p}{\partial t} = -\frac{1}{q} \nabla \cdot \vec{J}_p - \frac{p}{\tau_p} + g(\vec{r}, t) \tag{6.12}$$

Assuming that the generated charge carriers are evenly distributed along the track, , so the generation term is independent of the position $\vec{r}$. If no spacial gradient is presented, $\nabla \cdot \vec{J}_n$ and $\nabla \cdot \vec{J}_p$ vanish. Hence, the rate equation reduces to:

$$\frac{\partial n}{\partial t} = -\frac{n}{\tau_n} + g(t) \tag{6.13}$$

$$\frac{\partial p}{\partial t} = -\frac{p}{\tau_p} + g(t) \tag{6.14}$$

The traversal time for a charged particle to pass a sensor is in the picosecond range, and the charge collection time is in the nanosecond range, which implies that $g(t)$ is approximately a $\delta(t)$ function. As the process for $t > 0$ is of concern, $g(t)$ can be set to 0.

Combining the definition of mean free path (eq.(6.8), eq.(6.9) and eq.(6.10)) and the continuity equations(eq.(6.13) and eq.(6.14)), the differential equations can be obtained:

$$\frac{dn}{n} = -\frac{dt}{\tau_n} = +\frac{dx}{v_n \tau_n} = +\frac{dx}{\lambda_e} \tag{6.15}$$

$$\frac{dp}{p} = -\frac{dt}{\tau_p} = +\frac{dx}{v_p \tau_p} = +\frac{dx}{\lambda_h} \tag{6.16}$$

The solution of eq.(6.15) and eq.(6.16) shows the decay of carrier density versus their drifting distance.

λ can be treated as a constant throughout the sample if (a) the material is a single crystal (b) the strength of the electric field $|\vec{E}|$ is large enough, so the velocity of the carrier saturates. For diamond the saturation field strength is $0.8\,\mathrm{V\,\mu m^{-1}}$ [31]. For Si the saturation field strength is $1.0\,\mathrm{V\,\mu m^{-1}}$ [34]. In this case, the solution of eq.(6.15) and eq.(6.16) are simple exponential decay.

As illustrated by fig. 6.7, electron and positron are generated at position x' at time $t = 0$, and they drift along the x direction. Using initial conditions: when $t = 0$ (or $x = x'$), $n(x') = n_{ionized}$ and $p(x') = p_{ionized}$. The solution of eq.(6.15) (eq.(6.16)) are:

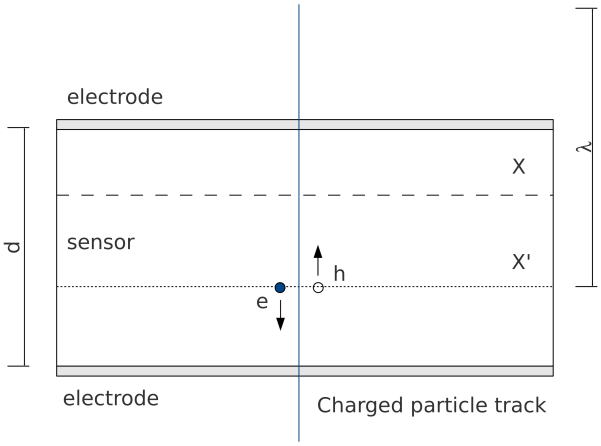

Figure 6.7: The charge collection process in a sensor. The schematic diagram shows the structure of the sensor and the charge carrier generated by the traversing track. d is the thickness of the sensor. x' is the position of charge carrier generation. The electron e and hole h drift apart towards the electrodes. x is the position of the drifting charge. λ is the mean free path of the carrier.

$$n(x, x') = n_{ionized} \exp\left(-\frac{x' - x}{\lambda_e}\right) \tag{6.17}$$

$$p(x, x') = p_{ionized} \exp\left(-\frac{x - x'}{\lambda_h}\right) \tag{6.18}$$

The motion of the charge carriers induces a current pulse on the electrode. The induced charge is called $Q_{collected}$. The sensor can be regarded as a parallel plate capacitor with thickness d. The induced charge from detector with such a geometry can be described by Ramo's Theorem [70]:

$$dQ_{induced} = dQ_{ionized} \vec{\nabla}\phi_w \cdot d\vec{r} \tag{6.19}$$

For a one-dimensional parallel plate, the weighting field $\vec{\nabla}\phi_w$ is $1/d$, and the $d\vec{r}$ reduces to dx. When $t = 0$ ($x = x'$), $dQ_{ionized}$ can be given by $n_{ionized}\, dv'$ (or $p_{ionized}\, dv'$), where dv' can be considered as a cylindrical volume $S\,dx'$ with S is the surface and dx' is the height. The charges in dv' drift a distance of dx, and the concentration of the charge changes to $n(x, x')$ ($p(x, x')$) at the position x, so that the $dQ_{ionized}$ at the position x becomes $n(x, x')dv'$ or $p(x, x')dv'$.

When the carriers drift a distance dx under $\vec{E}$, the induced charge on the electrode are:

$$dQ_{collected,n} = -[qn(x, x')dv']\frac{1}{d}dx \tag{6.20}$$

$$dQ_{collected,p} = +[qp(x, x')dv']\frac{1}{d}dx \tag{6.21}$$

Integration of $dQ_{collected}$ gives the total signal charge:

$$Q_{collected,n} = \int dQ_{collected,n} = -\int_v dv' \int_{x'}^{0} qn(x,x') \cdot \frac{dx}{d} \tag{6.22}$$

$$Q_{collected,p} = \int dQ_{collected,p} = +\int_v dv' \int_{x'}^{d} qp(x,x') \cdot \frac{dx}{d} \tag{6.23}$$

Using $dv' = S\,dx'$, since the total volume of the snesor is $V = S \times d$, thus:

$$Q_{collected,n} = -S \int_0^d dx' \int_{x'}^{0} qn(x,x') \cdot \frac{dx}{d} \tag{6.24}$$

$$Q_{collected,p} = +S \int_0^d dx' \int_{x'}^{d} qp(x,x') \cdot \frac{dx}{d} \tag{6.25}$$

Substituting the spatial distribution of charge carriers given in eq.(6.17) and eq.(6.18) into eq.(6.24) and eq.(6.25):

$$Q_{collected,n} = -S \int_0^d dx' \int_{x'}^{0} qn_{ionized} \exp\left(-\frac{x'-x}{\lambda_e}\right) \cdot \frac{dx}{d} \tag{6.26}$$

$$Q_{collected,p} = +S \int_0^d dx' \int_{x'}^{d} qp_{ionized} \exp\left(-\frac{x-x'}{\lambda_h}\right) \cdot \frac{dx}{d} \tag{6.27}$$

The results of the integration are:

$$Q_{collected,n} = Q_{ionized} \frac{\lambda_e}{d}\left[1 - \frac{\lambda_e}{d}\left(1 - e^{-\frac{d}{\lambda_e}}\right)\right] \tag{6.28}$$

$$Q_{collected,p} = Q_{ionized} \frac{\lambda_h}{d}\left[1 - \frac{\lambda_h}{d}\left(1 - e^{-\frac{d}{\lambda_h}}\right)\right] \tag{6.29}$$

Where $Q_{ionized}$ is defined as the total number of electron and hole pairs generated by the high energy particle:

$$Q_{ionized} \stackrel{\text{def}}{=} n_{ionized} \times (S \cdot d) = p_{ionized} \times (S \cdot d) \tag{6.30}$$

The total induced charge is the superposition of the positive and negative charge carriers:

$$Q_{collected} = Q_{collected,n} + Q_{collected,p} \tag{6.31}$$

$$\frac{Q_{collected}}{Q_{ionized}} = \sum_{i=e,h} \frac{\lambda_i}{d}\left[1 - \frac{\lambda_i}{d}\left(1 - e^{-\frac{d}{\lambda_i}}\right)\right] \tag{6.32}$$

$Q_{collected}/Q_{ionized}$ is plotted as a function of λ/d in fig. 6.8. The $Q_{collected}$ increases rapidly when λ is much shorter than the thickness of the detector d, and then the $Q_{collected}$ slowly saturates when λ is longer than d. If λ is much longer than d, the $Q_{induced}$ is nearly fully collected. This describes the charge collection in unirradiated sCVD diamond. On the other hand, in pCVD or irradiated diamond, λ is shorter than d, which means that the density of the charge carriers decays faster in space (see eq.(6.17) and eq.(6.18)), the average travel range

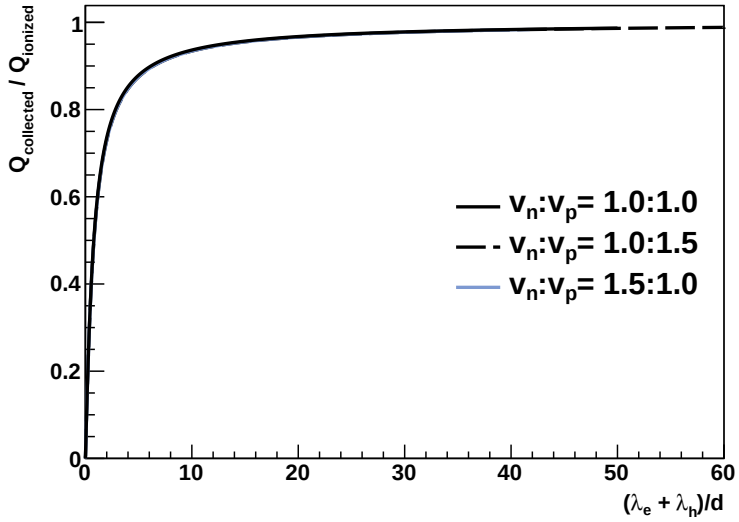

Figure 6.8: $Q_{collected}/Q_{ionized}$ with respect to λ/d. The v_n and v_p are the saturation velocities of electrons and holes, respectively. Three cases, v_n:v_p = 1.0:1.0 (black), v_n:v_p = 1.0:1.5 (dahed), and v_n:v_p = 1.5:1.0 (gray) are applied in eq.(6.32) to calculated the $Q_{collected}/Q_{ionized}$. The three lines show that the $Q_{collected}/Q_{ionized}$ is not sensitive to the ratio between v_n and v_p. Therefore, the $v_n = v_p$ condition is always used in the following calculations.

Table 6.3: Saturation electric field strength and the corresponding saturation velocity of charge carriers in diamond [31] and Si [34].

		diamond		Si		
symbol	definition	electron	hole	electron	hole	unit
$\lvert\vec{E}_{sat}\rvert$	saturation field strength	0.8	0.8	1.0	1.0	$\mathrm{V\,\mu m^{-1}}$
v_{sat}	saturation velocity	9.6×10^6	14.1×10^6	$\sim 10^7$	$\sim 10^7$	$\mathrm{m\,s^{-1}}$

of the charge carriers is shorter, so the amount of the collected charge is less than the ionized charge.

The $\lambda_e = v_n\tau_n$ and $\lambda_h = v_p\tau_p$ might be different for electrons and holes. For detector biased at high voltage, the saturation velocity of holes in diamond is 1.5 times that of the electron velocity (see Table 6.3), and in Si the saturation of electrons and holes are the same. The curves for both cases are plotted in fig. 6.8 to test the sensitivity of $Q_{collected}$ with respect to different v_n and v_p. The result shows that the discrepancy between $Q_{collected}/Q_{ionized}$ plotted using $v_n = v_p$ or $1.5 \cdot v_n = v_p$ is negligible. Therefore, the $v_n = v_p$ condition is always used in the following calculations.

Damage curve: mean free path versus irradiation

The drifting charge can be captured by the deep crystal defects. If the shaping time of the readout circuit is shorter than the time for carrier re-emission, the signal is lost.

According to the Matthiessen's scaling rule, the inverse of the carrier life time ($1/\tau$) is proportional to the number of defects (N) [71]. The more defects the lattice has, the smaller the survival time of charge carriers. By assuming the number of defects increases linearly with the particle fluence, the inverse of τ is proportional to the radiation fluence (Φ), too. The relation between τ and Φ can be written as [72]:

$$\frac{1}{\tau} = \frac{1}{\tau_0} + \beta \cdot \Phi \tag{6.33}$$

β is the damage coefficient. Since the mean free path λ is $\tau \cdot v_{sat}$, the damage curve based on λ is defined as [72]:

$$\frac{1}{\lambda} = \frac{1}{\lambda_0} + k \cdot \Phi \tag{6.34}$$

where k is the damage constant. k is the characterizing parameter for radiation-hardness. It depends on the particle type, the energy of the irradiation, and the material. Smaller k means that λ decays slower with increasing Φ, and thus, better radiation tolerance is given.

Unlike the NIEL hypothesis, which only works for material with leakage current, the damage curve is universal to describe the trapping effect in all kinds of material. Besides, the trapping is directly related to the signal from a sensor. Therefore, the damage constant is the figure-of-merit to compare radiation-hardness of diamond and Si in this thesis.

6.2 Radiation damage on diamond

The damage constant k should be measured experimentally. In this section, the experimental method and analysis to find k is presented.

6.2.1 Experimental methods and instruments

The measurement of the change in signal charge before and after irradiation should not depend on the type of readout used. Therefore, the following measurements were performed using detectors equipped with a single channel charge sensitive readout connected to a readout pad on the diamond sensor, see fig. 6.9.

Three diamonds were made into pad detectors: one sCVD diamond provided by the manufacturer "Diamond Detectors Limited[1]", and two pCVD diamonds provided by "elementsix[2]". The diamond sensor is thinned to the desired thickness and cut using laser by the manufacturer. To eliminate the surface defects, the diamond is polished and cleaned to remove the residual chemicals on the surface. The pad electrode is metalized by Institut zür Zuverlaesigkeit und Microintegration in Berlin, Germany, using the Ar Re-sputtering Technique. Then the diamond pad detectors are irradiated using the 25 MeV proton beam offered by the Karlsruhe Irradiation Center. See section 4.1 for the detailed process of metalization and irradiation.

The signal has been measured before and after the irradiation to assess the relative signal loss. The measurement is done with the setup shown in fig. 6.10. The radioactive source ^{90}Sr is used to generate signal in the diamonds. To select straight, high energy tracks, the

[1] http://www.diamonddetectors.com/
[2] http://www.e6.com

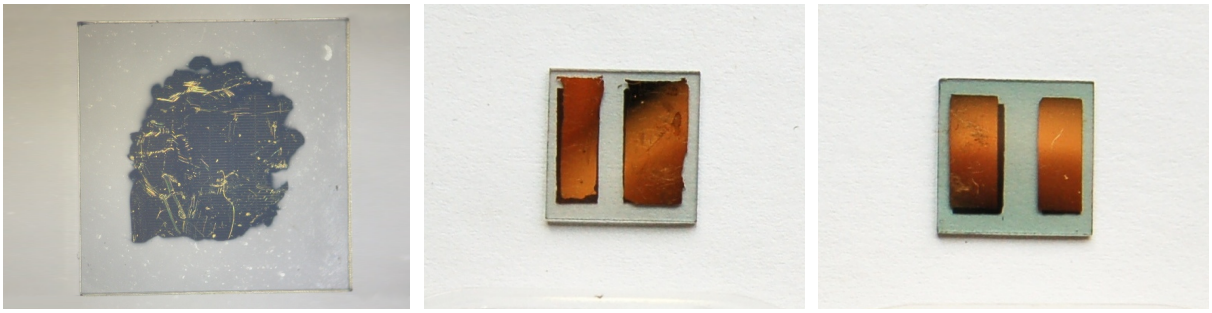

(a) (b) (c)

Figure 6.9: Diamonds for the radiation hardness experiment. (a) sCVD diamond (DDL4) 5 mm × 5 mm × 542 µm (b) pCVD diamond (UT21) 10 mm × 10 mm × 520 µm(c) pCVD diamond (UT29) 10 mm × 10mm × 449 µm

electrons need to pass a collimator and reach a scintillator behind the diamond pad detector for triggering. Range calculation for electrons using the NIST ESTAR calculator [46] shows that the minimum required kinetic energy ($T_{e,min}$) to pass all the material is 1.05 MeV. Therefore, the energy range of detected electron is from 1.05 MeV to 2.28 MeV, corresponding to $\beta\gamma$=2.05 to $\beta\gamma$=4.46, which gives the stopping power close to that of a MIP.

The diamond is biased with at least1.8 V µm^{-1}, and the induced signal current is fed into a charge sensitive amplifier [73], and then to a CR-RC shaper with a time constant 2.5 µs [74]. The pulse height is proportional to the amount of signal charge, the calibration is 1.0 mV = 54 electron-hole pairs with a 5% error.

The irradiation by 25 MeV proton on diamonds was repeated several times, and the average collected charge was measured versus the increasing proton fluence. The diamonds must be pumped for 12 hours before performing the measurement to achieve the maximum charge collection(see section 4.3). The analysis method and results are presented in the next section.

6.2.2 Results

From collected charge to mean free path

Once the signal charge $Q_{collected}$ is measured, the mean free path λ can be deduced using fig. 6.8. $Q_{collected}$ is measured, $Q_{ionized}$ is calculated by eq.(5.5). The thickness of the detector d is known. From the ratio $Q_{collected}/Q_{ionized}$, the corresponding λ/d is obtained, and thus the λ. The error on the λ represents the interval of possible λ range due to the 5% uncertainty of the $Q_{collected}$ measurement. The error on the λ is asymmetric because the relation shown in fig. 6.8 is not linear. The larger $Q_{collected}$ has the bigger error on λ, since the $Q_{collected}/Q_{ionized}$ saturates to 1 when λ approaches to infinity. The $Q_{collected}/Q_{ionized}$ versus the 25 MeV proton fluence is shown in fig. 6.11(a), and the corresponding mean free path λ is in fig. 6.11(b).

The shift of the pCVD diamond data

The irregular grain structures of the pCVD diamond results in trapping, too. The pCVD diamond can be treated as if a previously irradiated sCVD diamond. The sCVD and pCVD diamonds must have the same damage constant if they are damaged by the same irradiation.

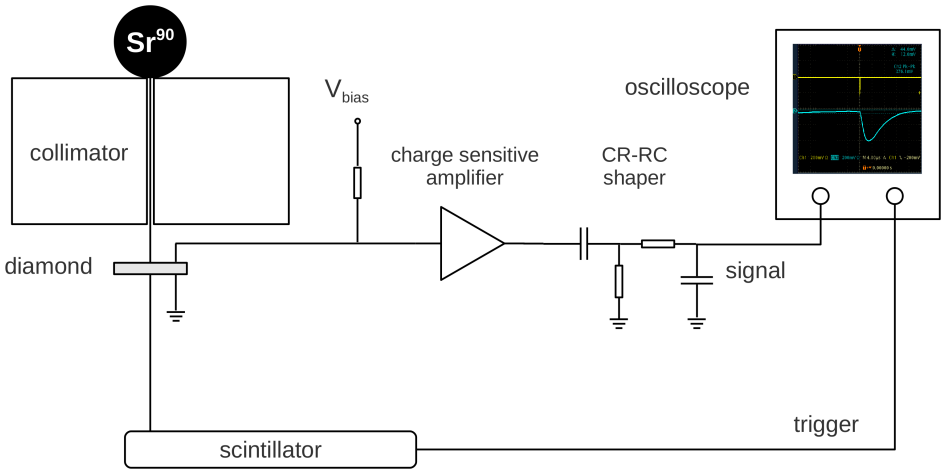

Figure 6.10: ^{90}Sr source test setup. The electrons are collimated to penetrate the diamond, and hit the scintillator behind the diamond. The signal current in the diamond is amplified by the charge sensitive amplifier and the shaper, and then detected by the oscilloscope. The oscilloscope is triggered by the signal from the scintillator.

The only difference is the starting mean free path (λ_0). Every pCVD diamonds can have different λ_0, since λ_0 depends on the quality of the crystal. As shown in fig. 6.11(b), if the λ data points of pCVD diamonds (UT29 ad UT21) are shifted properly to the right side along the proton fluence axis, all the λ data can lie on the same damage curve.

The most proper shift is determined using the minimum χ^2 method, see fig. 6.12. The pCVD diamond data are shifted with respect to the sCVD diamond data, and all the data point are fit together using the damage curve eq.(6.34) to get the parameter k. The fit of each shift gives a quality factor of the fit, $\frac{\chi^2}{NDF}$, where χ^2 is the variation of the fit due to the variation of the fit parameter, NDF is the number of degrees of freedom. The $\frac{\chi^2}{NDF}$ approaches to 1 for a good fit. The shift which gives the minimum $\frac{\chi^2}{NDF}$ ($\frac{\chi^2}{NDF\,min}$) is the most proper one, see the gray dotted arrow in fig. 6.12.

The variation of the shift leads to the variation of k. The uncertainty of k due to the shift is defined as the range of k, which gives $\frac{\chi^2}{NDF} \leq \frac{\chi^2}{NDF\,min} + 1$ (see the intervals σ^+_{shift} and σ^-_{shift} in fig. 6.12). The error on k from the fit (σ_{fit}) is smaller than 10% of σ_{shift}, so their correlation can be neglected. The shift is applied to every pCVD diamond data set. σ_{shift} is asymmetric, so the positive (σ^+_{shift}) and negative(σ^-_{shift}) components should be treated separately. The total error on the k is defined as following:

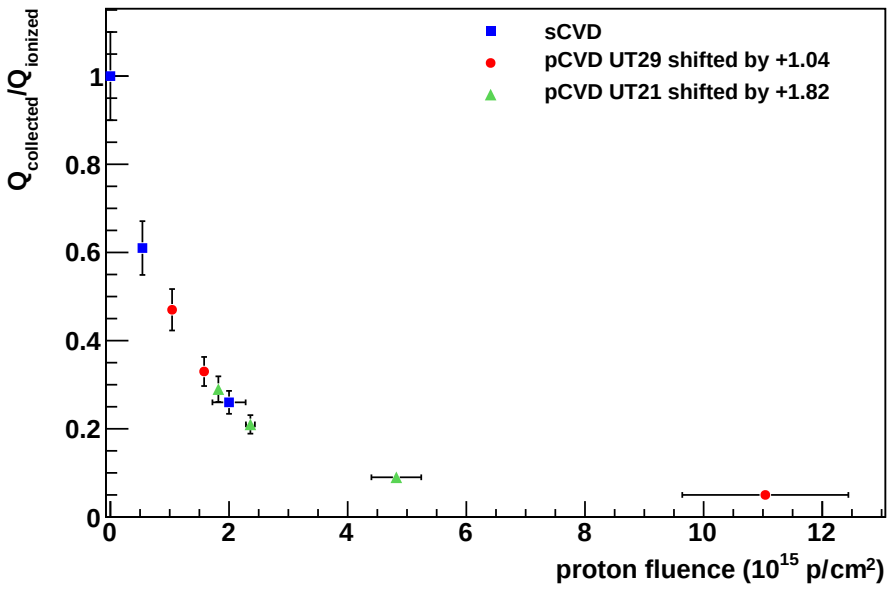

(a)

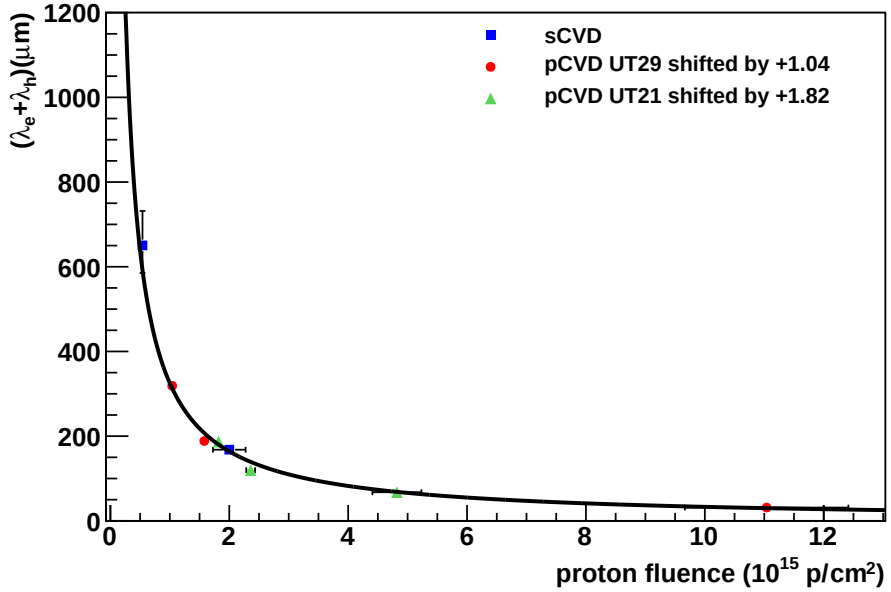

(b)

Figure 6.11: Decay of the signal and the mean free path of diamond damaged by 25 MeV protons. (a) $Q_{collected}/Q_{ionized}$ as a function of the proton fluence. (b) Mean free path ($\lambda_e + \lambda_h$) with respect to the proton fluence, fit by the damage curve eq.(6.34). The square, circle, and triangle markers represent the data of sCVD diamond DDL4, pCVD diamond UT29, and pCVD diamond UT21, respectively. The data points of UT29 is shifted to the right by 1.04×10^{15} p/cm^2, and of UT21 by 1.82×10^{15} p/cm^2. The shift implies that the grain structure in the pCVD diamonds can trap the charge carriers, as if they are previously irradiated by fluence of 1.04×10^{15} p/cm^2 (in case of UT29) or 1.82×10^{15} p/cm^2 (in case of UT21). The results show that sCVD and pCVD diamonds have the same damage curve, and the shift is determined by minimizing the χ^2 of the combined fit.

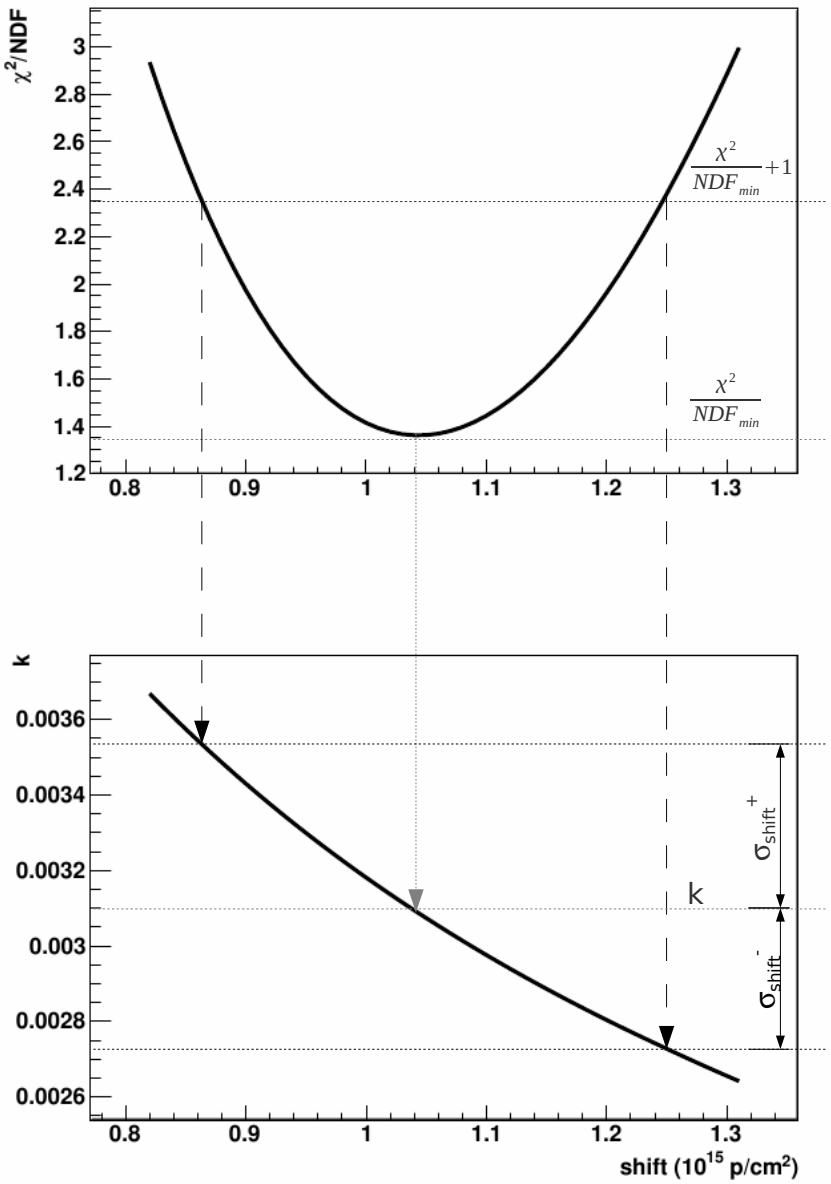

Figure 6.12: Determination of the uncertainty on damage constant k due to the shifting of pCVD diamond data. The upper plot shows the $\frac{\chi^2}{NDF}$ of the damage curve fit with respect to the shift of proton fluence. The bottom plot shows the damage constant k with respect to the amount of shift. The dotted arrow shows the minimum $\frac{\chi^2}{NDF}$ given by 1.04 p/cm^2 of shift, and its corresponding k. The dashed arrows shows the position of $\frac{\chi^2}{NDF}$ + 1. The interval between the dashed lines (σ^+_{shift} and σ^-_{shift}) are the uncertainty on k from the shifting.

$$\sigma^{+}_{tot} = \sqrt{{\sigma_{fit}}^2 + {\sigma^{+}_{shift,1}}^2 + {\sigma^{+}_{shift,2}}^2 \ldots}$$

$$\sigma^{-}_{tot} = \sqrt{{\sigma_{fit}}^2 + {\sigma^{-}_{shift,1}}^2 + {\sigma^{-}_{shift,2}}^2 \ldots}$$

The fit of all data from sCVD and pCVD diamonds together is shown in fig. 6.11(b). The damage constant of 25 MeV proton on diamond is

$$k_{25MeV} = \left(3.02^{+0.36}_{-0.42}\right) \times 10^{-18} \ \frac{cm^2}{\mu m}$$

6.3 Comparison of radiation damage on diamond and silicon

The analysis method described in section 6.2.2 can be applied to not only diamond but also Si. The trapping in diamond and Si damaged by 25 MeV and 24 GeV protons are compared below.

Irradiations of sCVD and pCVD diamond sensors have been performed by the RD42 collaboration [75] for protons at various energies between 25 MeV and 24 GeV. Since there is no generally accepted NIEL damage normalization for diamond, the 25 MeV and 24 GeV proton irradiation are chosen to be compared because they correspond well to the high and low energy extremes of the particle energy spectrum at the LHC. For the diamond data, the 25 MeV proton radiation damage is measured using the diamond pad detector and ^{90}Sr source, as described in section 6.2.1. The 24 MeV proton damage was measured by the RD42 Collaboration using the strip readout and the 120 GeV pion beam at the CERN.

For Si, the published data of irradiated planar Si n-in-p FZ strip detectors are used [76][77]. To compare diamond and Si at the same operation condition, the planar-Si was chosen because its geometry is similar to the diamond ones, and the bias should generate similar electric field strength at the both sensors (for diamond ~ 1.8 V/μm, for Si ~ 1.8-2.2 V/μm) before irradiation. This corresponds to 900 V on 500 μm thick diamond sensors and 600 V for 310 μm [76][77] thick Si sensors operated in over-depletion. The signal charge of 310 μm Si sensors biased by 600V is extrapolated by averaging the measurements for 500 V and 700 V [76][77].

While for irradiated diamond the signals are lost due to trapping, for Si additional effects must be taken into account. With increasing radiation the effective doping concentration changes, the sensor can no longer be fully depleted. The shortening of the distance to collect contributes to the decrease of λ, too. Furthermore, charge multiplication effects have been reported for thin Si sensor heavily irradiated by 25 MeV proton [76]. To extract the charge-loss due to trapping from the Si measurement, a special parameterization of the damage curve is applied to fit all the data for k :

$$\lambda = \lambda_e + \lambda_h = \frac{\lambda_0}{1 + \lambda_0 k \Phi} + \alpha \Phi^{\beta} \tag{6.35}$$

Table 6.4: Measured damage constants for diamond and Si for 25 MeV and 24 GeV proton irradiation.

	25 MeV proton	24 GeV proton	unit
$k_{diamond}$	$3.02^{+0.42}_{-0.36}$	$0.69^{+0.14}_{-0.17}$	$10^{-18}\text{cm}^2\,\mu\text{m}^{-1}$
$\alpha_{diamond}$	-3.83 ± 7.81	4.71 ± 14.8	μm
k_{Si}	$10.89^{+1.79}_{-1.79}$	$1.60^{+0.38}_{-0.38}$	$10^{-18}\text{cm}^2\,\mu\text{m}^{-1}$
α_{Si}	50.86 ± 9.83	14.18 ± 19.8	μm

Fig. 6.13 shows damage curve fits for irradiations with 24 MeV and 24 GeV protons, respectively, and Table 6.4 shows the k and the α from the fit. The β comes out to be about 0 for all diamond and Si data. The α is (50.86 ± 9.83) μm for Si damaged by 25 MeV protons, while for the diamond and the 24 GeV damage on Si α is negligible, which confirms the observation in [76] that the charge collection is enhanced in Si heavily irradiated by 25 MeV protons . The damage constants k for diamond are generally smaller than those for Si by a factor of about 3, indicating that diamond is radiation harder than Si in terms of trapping and signal loss.

6.4 Signal versus irradiation

The signal before irradiation has been discussed in chapter 5. The $Q_{ionized}$ is the most probable value of the signal, which is calculated by eq.(5.9) and eq.(5.11). With the help of the measured k and the eq.(6.34) and eq.(6.32), the $Q_{collected}$ for 200 μm sensors traversed by 1 GeV pions are evaluated as a function of the proton fluence, see fig. 6.14.

The curves indicates that although the Si can start with a much higher signal because of the small energy needed to create electron and hole pairs, the harder radiation tolerance of diamond renders similar signal levels for both materials when the proton fluence is in the order of 10^{16} p/cm^2.

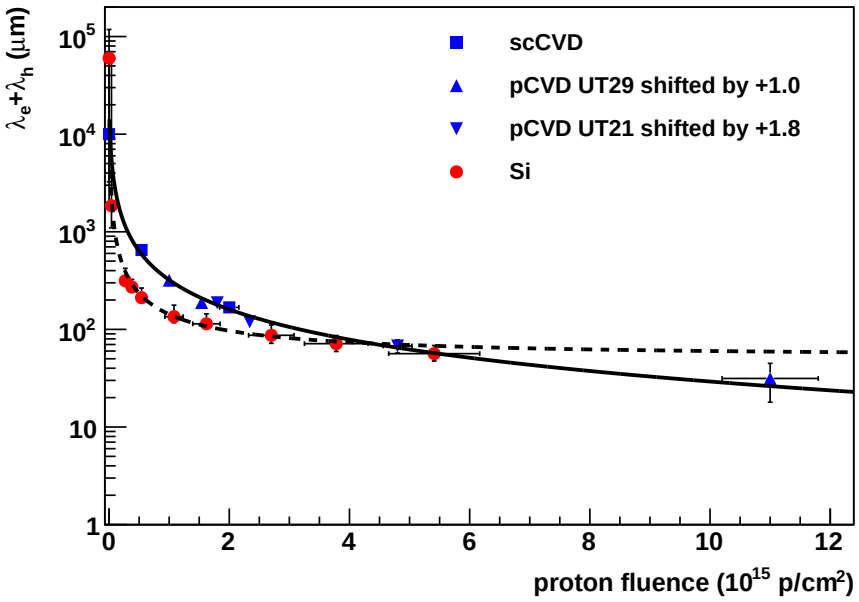

(a)

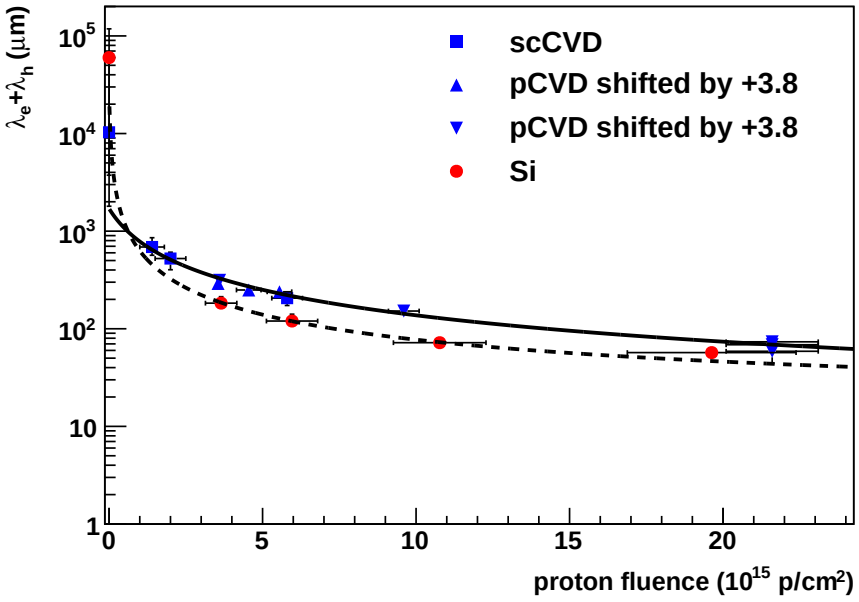

(b)

Figure 6.13: Damage curves for diamond and Si irradiated by (a) 25 MeV protons and (b) 24 GeV protons. ($\lambda_e+\lambda_h$) is the mean free path. The square markers are for sCVD diamond, triangles for pCVD diamond, and circles are for Si. The solid line and dashed line are the damage curve fits (eq.(6.35)) for diamond and Si data, respectively. The pCVD diamond data are shifted by the amount of fluence indicated in the legend, and the amount of shift are determined by the method explained in section 6.2.2.

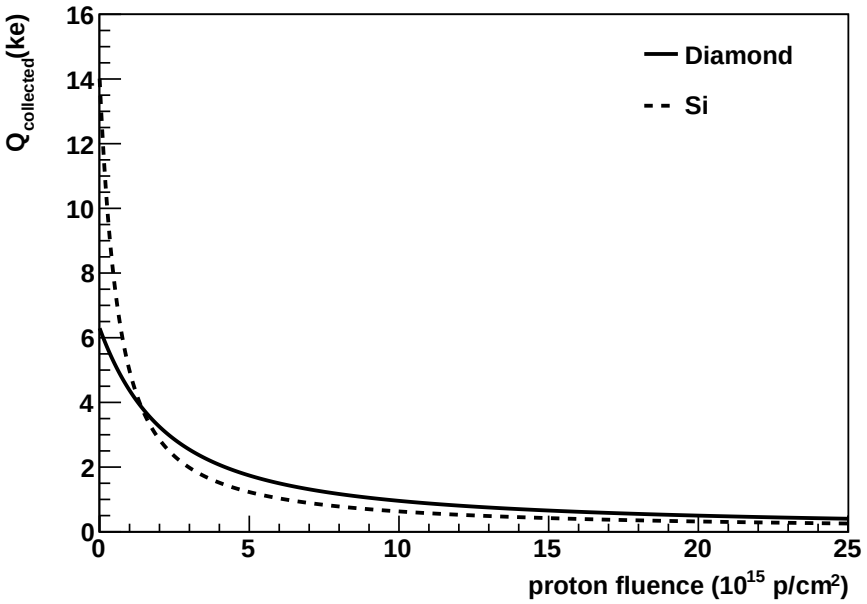

(a)

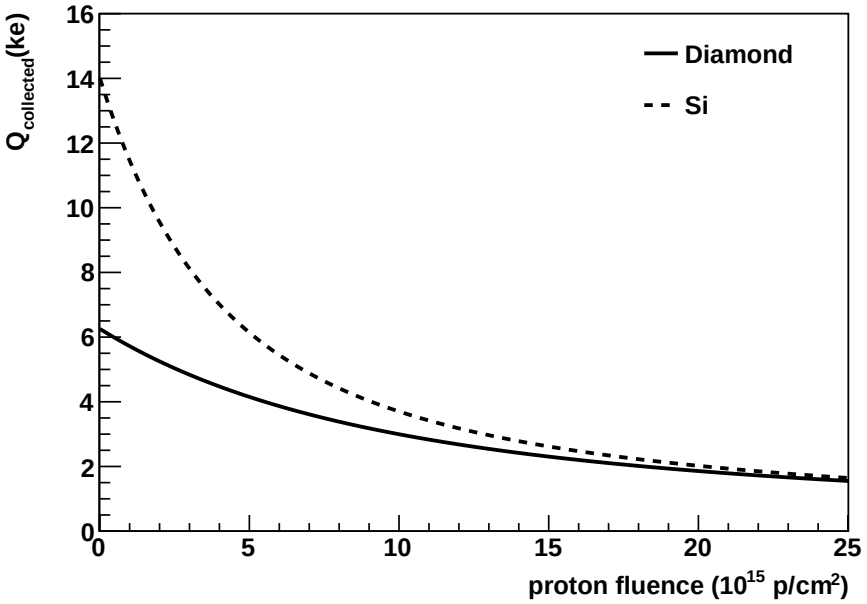

(b)

Figure 6.14: Expected most probable value of the signal ($Q_{collected}$) in units of 1000 electrons for 1 GeV pion traversing 200 μm thick diamond and Si sensors damaged by (a) 25 MeV protons and (b) 24 GeV protons. The solid line and dashed line are for diamond and Si, respectively.

Chapter 7

Noise

The generation and deterioration of the signals has been characterized using pad detectors, and are presented in chapter 5 and chater 6, respectively. In this chapter, the electronic noise from the pixel readout is discussed. By combining the results in chapter 5, chapter 6 and this chapter, the SNR of a pixel detector can be estimated as a function of the radiation fluence.

The structure of the FE-I4 hybrid pixel detector has been introduced in section 3.3. Three methods are applied to estimate the electronic noise from a hybrid pixel:

- An analytical model with the dominant noise sources.
- The transient noise simulation on the original FE-I4 chip layout using the SPECTRE simulation package in CADENCE.
- The AC simulation on the original FE-I4 chip layout using the same simulation package as the transient noise simulation.

Once the input capacitance to the preamplifier and the development of leakage current of the sensor are determined, the increase of the noise with respect to the radiation damage can be predicted for any sensor type based on the three estimation methods.

7.1 Noise sources

Electronic noise is the random fluctuation of voltage or current in the circuit. The amplitude of the fluctuation is Gaussian distributed, and the average of the amplitude is 0. Usually noise is described by the variance of current $\langle i^2 \rangle$ or voltage $\langle v^2 \rangle$. Consider n carriers of charge e moving with a velocity v through a sample of length l, the current i is

$$i = \frac{nev}{l} \tag{7.1}$$

The fluctuation of i is given by

$$\langle di \rangle^2 = \left(\frac{ne}{l} \langle dv \rangle \right)^2 + \left(\frac{ev}{l} \langle dn \rangle \right)^2 \tag{7.2}$$

This relation shows that there are two mechanisms contributing to the total noise:

- velocity fluctuations, e.g. thermal noise
- number fluctuations, e.g. shot noise and $\frac{1}{f}$ noise

The three noise sources are the following:

Shot noise

Shot noise is the fluctuation in the number of charges, while the current is flowing through a junction, where the charge carriers must overcome an energy barrier introduced by the contact between different materials. The shot noise is "white noise", which means that its power density spectrum is flat. The power spectral density (PSD) of shot noise is proportional to the average flowing current $\langle i \rangle$:

$$d\langle i^2_{shot} \rangle = 2q\langle i \rangle \, df \tag{7.3}$$

In the pixel detector, the main shot noise source is the reverse biased sensor, where the leakage current is flowing though the p-n junction. The leakage current increases with radiation damage, so the shot noise is a significant source of noise in high radiation environments.

Thermal noise

The velocity of individual charge carriers can fluctuate due to random thermal motions. Thermal noise is also white noise, and the PSD is proportional to the temperature and the resistance of the conductor:

$$d\langle v^2_{therm} \rangle = 4kTR \, df \tag{7.4}$$

$$d\langle i^2_{therm} \rangle = 4kT \frac{1}{R} \, df \tag{7.5}$$

Flicker noise

Flicker noise ($\frac{1}{f}$ noise) has a large variety of sources which are not fully random in time, so the noise spectrum becomes non-uniform and depends on the frequency of the fluctuation. For example when the charge carriers are trapped in the defects of the crystal, and then are released with a time constant τ. With an infinite number of uniformly distributed time constants in the time domain, the spectral power density approaches a $\frac{1}{f}$-dependent distribution in the frequency domain.

The PSD of $\frac{1}{f}$ noise can be written as

$$d\langle v^2_{\frac{1}{f}} \rangle = \widetilde{K}_F \frac{1}{f^\alpha} \, df \tag{7.6}$$

where α is typically between 0.5 and 2.0. $\widetilde{K}_F$ is the $\frac{1}{f}$ noise coefficient, which depends on the electronic component and is usually measured experimentally.

Noise from a metal-oxide-semiconductor field-effect transistor

In the FE-I4 pixel readout, the main noise source is the current flowing through the channel of the n-channel metal-oxide-semiconductor field-effect transistor (n-channel MOSFET, or NMOS) amplification transistor. The shot noise from the interface of oxide and substrate can be neglected since the input impedance is very large and thus the current is negligible.

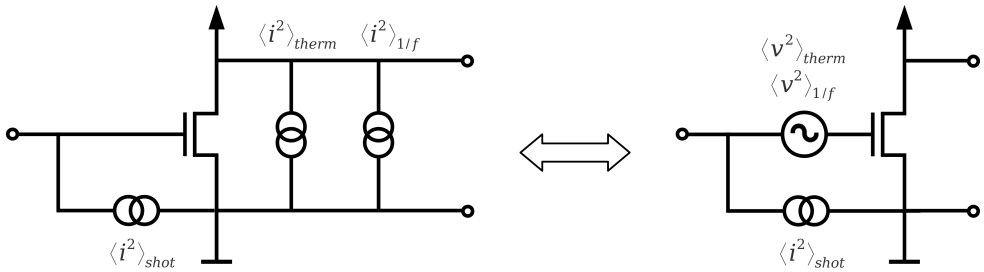

Figure 7.1: schematic diagram of the noise current source of a MOSFET.

The fluctuation of the drain-source current of a MOSFET is

$$d\langle i^2_{therm} \rangle = 4kT\gamma g_m \, df \tag{7.7}$$

where the $\gamma = \frac{2}{3}$ for the MOSFET operated in strong inversion, and $\gamma = \frac{1}{2}$ for those operated in weak inversion [78][79]. The fluctuation of the drain-source current can be expressed as if it is induced by the fluctuation of the voltage at the gate $\langle v^2_{therm} \rangle$, see fig. 7.1. Using the relation $i_{ds} = v_{gs} g_m$, the input-referred thermal noise formula becomes

$$d\langle v^2_{therm} \rangle = 4kT\gamma \frac{1}{g_m} \, df \tag{7.8}$$

For the MOSFET operated in weak inversion, the transconductance g_m can be calculated from the drain-source current (i_{ds}) [80]:

$$g_m = \frac{q i_{ds}}{nkT} \tag{7.9}$$

The simulation of the original FE-I4 layout shows that the ideality factor n is 1.41 for the 130 nm MOSFET of the preamplifier transistor. Substituting eq.(7.9) in to the thermal noise equation eq.(7.7), $d\langle i^2_{therm} \rangle = 2qI_d(1/n) \, df$, so the thermal noise can be modeled as the shot noise for a MOSFET operated in weak inversion.

The $\frac{1}{f}$ noise from the channel of the MOSFET can be written as

$$d\langle v^2_{\frac{1}{f}} \rangle = \widetilde{K}_F \frac{1}{f^\alpha} \, df = \frac{K_F}{C_{ox} W L} \frac{1}{f^\alpha} \, df \tag{7.10}$$

Where K_F is the coefficient depending on the technology and transistor types, C_{ox} is the capacitance per unit area of the oxide layer, W and L are the width and length of the channel, and the coefficient α is 1 [79][81] .

The noise power density expressions are applied to model the noise in the following section.

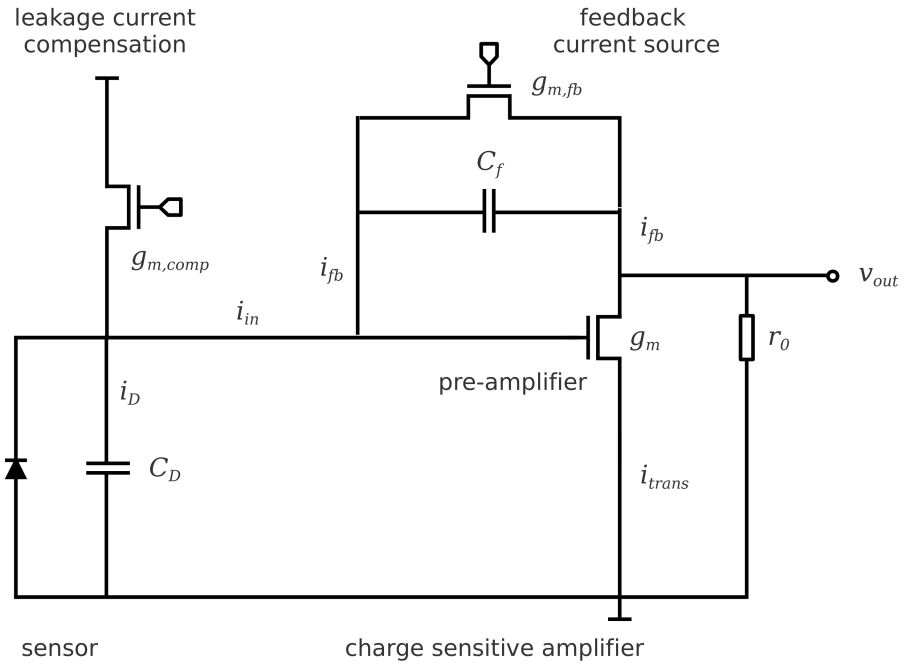

Figure 7.2: Schematic diagram of the model of a pixel readout circuit. The model is composed of the sensor, the leakage current compensation circuit, the feedback current source, and the charge sensitive pre-amplifier. Definition of the symbols are summarized in Table 7.1.

7.2 Analytical Model

The noise can be calculated analytically if the PSD of the noise at the input $i_{in}(j\omega)$ and the transfer function of the circuit $|H(\omega)|$ are known.

The voltage fluctuation at the output in the time domain is the inverse Laplace transform of the input signal $i_{in}(j\omega)$ multiplied by the tranfer function $|H(j\omega)|$:

$$v_{out}(t) = L^{-1}\{i_{in}(j\omega) \cdot H(j\omega)\} \tag{7.11}$$
$$v_{out}(t) = L^{-1}\{i_{in}(s) \cdot H(s)\} \tag{7.12}$$

where $s = j\omega$.

For the variance of the output voltage $\langle v_{out}^2 \rangle$, i_{in} and the transfer function must be integrated over all the frequencies and $\langle v_{out}^2 \rangle$ becomes:

$$\langle v_{out}^2 \rangle = \int_0^\infty \langle i_{in}(\omega)^2 \rangle \, |H(\omega)| \, d\omega \tag{7.13}$$

A model which contains the most essential units of the FE-I4 pixel circuit is shown in fig. 7.2. It is composed of the following units:

1. The charge sensitive amplifier (CSA) with the transistor preamplifier(preamp) and the feedback capacitance C_f

2. The constant current source to discharge C_f

3. The sensor which is an ideal diode with the input capacitance C_D

4. The current source for leakage current compensation

The second stage of the amplifier is neglected since its band width is broad, so the noise spectrum should not be influenced [37].

All the symbols used in the following derivations are listed in Table 7.1.

7.2.1 Transfer function

The transfer function of the FE-I4 pixel readout can be derived using nodal analysis [37][82]. Note that the transistor as the feedback current source is operated in weak inversion, and for signals smaller than 4000 electrons, the voltage across the drain and source of the transistor for the constant current source is small. Thus the transistor is operated in linear region [37]. Hence, the behavior of the current source is like a resistor, with $R_f = g_{ds,fb}^{-1}$.

For the input node:

$$\begin{aligned} -i_{in} + i_D + i_{fb} &= 0 \\ -i_{in} + v_{in} j\omega C_D + (v_{in} - v_{out}) \cdot (g_{ds,fb} + j\omega C_f) &= 0 \\ \Rightarrow v_{out}(g_{ds,fb} + j\omega C_f) - v_{in}(g_{ds,fb} + j\omega C_f + j\omega C_D) &= -i_{in} \end{aligned} \tag{7.14}$$

For the output node:

$$\begin{aligned} i_{fb} + i_{trans} + i_{load} &= 0 \\ (v_{out} - v_{in}) \cdot (g_{ds,fb} + j\omega C_f) + g_m v_{in} + \tfrac{v_{out}}{r_0} &= 0 \\ \Rightarrow v_{in} = v_{out} \frac{g_{ds,fb} + j\omega C_f + \frac{1}{r_0}}{g_{ds,fb} + j\omega C_f - g_m} & \end{aligned} \tag{7.15}$$

By inserting eq.(7.15) into eq.(7.14), and arranging the formula, the relation between i_{in} and v_{out} is found to be:

$$\frac{v_{out}}{i_{in}} = \frac{g_{ds,fb} + j\omega C_f - g_m}{\left(g_{ds,fb} + j\omega C_f + \frac{1}{r_0}\right)\left[g_{ds,fb} + j\omega(C_f + C_D)\right] - \left(g_{ds,fb} + j\omega C_f\right)\left(g_{ds,fb} + j\omega C_f - g_m\right)} \tag{7.16}$$

Since $r_0 >> 1$, $\frac{1}{r_0}$ is negligible, eq.(7.16) can be simplified as followings :

Table 7.1: Variables used in the noise calculation

variable	definition	units or value
i_D	signal current from the sensor	nA
i_{in}	current at the input of the pre-amplifier	nA
i_{leak}	leakage current from the sensor	nA
i_{comp}	current for leakage current compensation	nA
i_{fb}	feedback current	µA
i_{trans}	drain-source current of the pre-amplifier	7.5 µA
i_{load}	current through the load r_0	µA
g_m	transconductance of the pre-amplifier	225 µS
$g_{m,fb}$	transconductance of of i_{fb} current source	µS
$g_{m,comp}$	transconductance of current source for leakage current compensation	µS
$g_{ds,fb}$	drain-source conductance of i_{fb} source	800 nS
C_f	feedback capacitance	17 fF
C_i	capacitance from the pre-amplifier	32.1 fF
C_D	input capacitance	fF
r_0	load	Ω
τ_a	time constant C_f/g_m	ns
τ_b	time constant $C_f/g_{ds,fb}$	ns
τ_c	time constant C_d/g_m	ns
K_F	$\frac{1}{f}$ noise coefficient	13.5×10^{-25} J
C_{ox}	capacitance of the gate oxide of the pre-amplifier NMOS per unit area	$\varepsilon_0 \varepsilon_r \frac{1}{T_{ox}} = 0.0157\ \mathrm{F\,m^{-2}}$
ε_0	vacuum permittivity	$8.85 \times 10^{-12}\ \mathrm{F\,m^{-1}}$
ε_r	relative permittivity of SiO_2	3.9
T_{ox}	thickness of the oxide layer	2.2 nm
W	width of the MOS channel	15.5 µm
L	length of the MOS channel	320 nm
k	Boltzmann Constant	$1.38 \times 10^{-23}\ \mathrm{J\,K^{-1}}$
T	temperature	K
n	ideality factor	1.4

$$\begin{aligned}\frac{v_{out}}{i_{in}} &= \frac{g_{ds,fb} + j\omega C_f - g_m}{\left(g_{ds,fb} + j\omega C_f\right)(g_m + j\omega C_D)} \\ &= \frac{\left(\frac{g_{ds,fb}}{g_m} + j\omega C_f - 1\right) g_m}{\left(1 + j\omega\frac{C_f}{g_{ds,fb}}\right)\left(1 + j\omega\frac{C_D}{g_m}\right) g_{ds,fb} g_m} \\ &= \frac{-\frac{1}{g_{ds,fb}}\left(1 - j\omega C_f - \frac{g_{ds,fb}}{g_m}\right)}{\left(1 + j\omega\frac{C_f}{g_{ds,fb}}\right)\left(1 + j\omega\frac{C_D}{g_m}\right)}\end{aligned} \tag{7.17}$$

For small signals just above the threshold of the discriminator, that is set to be 2000 electrons, circuit simulation shows that the i_{fb} of the CSA is 4.5 nA, the $g_{ds,fb}$ of the feedback current source is 800 nS, and the g_m of the NMOS preamp transistor is 225 µS. Thus the fraction $\frac{g_{ds,fb}}{g_m} << 1$ and can be neglected. Define the time constants:

$$\tau_a = \frac{C_f}{g_m} \tag{7.18}$$

$$\tau_b = \frac{C_f}{g_{ds,fb}} \tag{7.19}$$

$$\tau_c = \frac{C_D}{g_m} \tag{7.20}$$

then the transfer function is obtained:

$$H(j\omega) = -\frac{1}{g_{ds,fb}} \frac{(1 - j\omega\tau_a)}{(1 + j\omega\tau_b)(1 + j\omega\tau_c)} \tag{7.21}$$

The signal at the output of the CSA is calculated by inserting eq.(7.21) into eq.(7.11). The input signal i_{in} is a δ-function $Q_{in}(t) = \delta(t)$ in the time domain, so in the s-domain $i_{in}(s)$ is a constant Q_{in}, therefore:

$$v_{out}(t) = L^{-1}\left\{-\frac{Q_{in}}{g_{ds,fb}} \cdot \frac{(1 - s\tau_a)}{(1 + s\tau_b)(1 + s\tau_c)}\right\} \tag{7.22}$$

$$v_{out}(t) = -\frac{Q_{in}}{g_{ds,fb}}\left[\frac{(\tau_a + \tau_b)e^{\frac{-t}{\tau_b}}}{\tau_b(\tau_b - \tau_c)} + \frac{(\tau_a + \tau_c)e^{\frac{-t}{\tau_c}}}{\tau_c(\tau_c - \tau_b)}\right] \tag{7.23}$$

The signal shape of an injected pulse corresponding to 3000 electrons is shown in fig. 7.3.

7.2.2 Equivalent noise charge

The dominant noise sources are illustrated in fig. 7.4. They are divided into two categories: the ones that are in serial to the gate of the preamp, and the ones that are in parallel. Their PSD are derived as following:

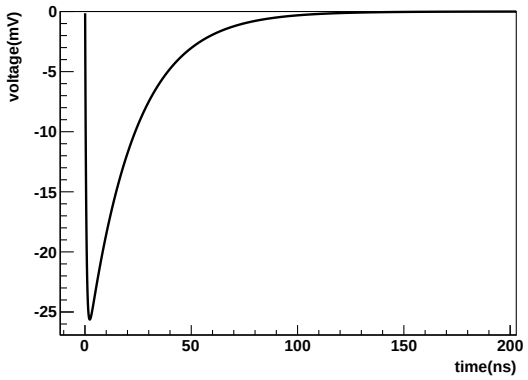

Figure 7.3: Signal at the output of the preamplifier corresponding to 3000 electrons of injected charge.

Serial noise

- Thermal noise from the preamp

  The transistor for the of the CSA is operated with $v_{gs} \approx v_{th}$, which means that its operation mode is just at the boarder between weak and strong inversion, in order to save power consumption [37]. The weak inversion form of the input-referred thermal noise PSD with $\gamma = 1/2$ is applied for the modelling:

$$d\langle v^2_{therm}\rangle = 4kT\frac{1}{2}\frac{1}{g_m}\,df \tag{7.24}$$

- $\frac{1}{f}$ noise from the preamp

  The input-referred $\frac{1}{f}$ noise PSD (eq.(7.10)) is used:

$$d\langle v^2_{\frac{1}{f}}\rangle = \frac{K_F}{C_{OX}WL}\frac{1}{f}\,df \tag{7.25}$$

The serial voltage fluctuation is equivalent to the voltage across the detector capacitance C_D, that is generated by a current fluctuation $\langle i^2\rangle = \frac{\langle v^2\rangle}{Z_D^2} = \langle v^2\rangle\omega^2 C_D^2$. By using this conversion all the serial noise sources can be treated as parallel noise, and the model circuit can be simplified as shown in fig. 7.5.

Parallel noise

- Shot noise

  The leakage current from the sensor contributes to the shot noise:

$$d\langle i^2_{shot}\rangle = 2qi_{leak}\,df \tag{7.26}$$

- Thermal noise from the feedback transistor

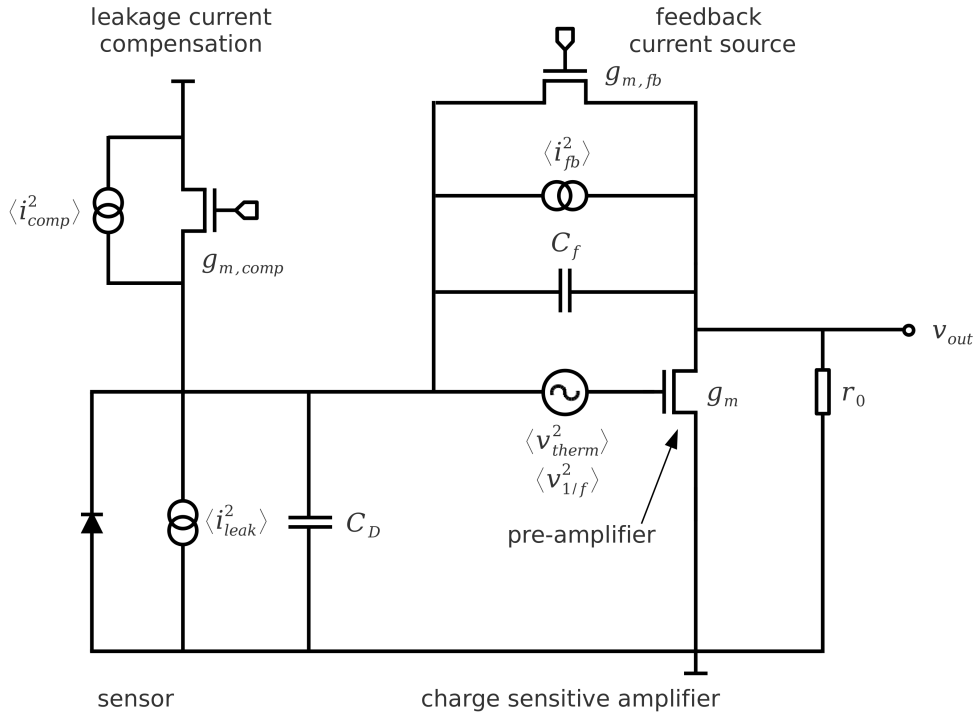

Figure 7.4: Dominant noise sources in a FE-I4 pixel readout. The circuit is based on the noise calculation model, fig. 7.2, and the dominant noise sources are marked on the circuit. $\langle i^2_{leak} \rangle$ represents the shot noise due to leakage current of the sensor. $\langle i^2_{comp} \rangle$ is the thermal noise from the transistor of the leakage current compensation circuit. $\langle i^2_{fb} \rangle$ is the thermal noise from the feedback current source. $\langle v^2_{therm} \rangle$ and $\langle v^2_{1/f} \rangle$ are the thermal and flicker noise of the NMOS of the preamp, respectively. Other symbols are defined in Table 7.1.

The transistor of the feedback current source is operated in weak inversion. When the signal is around the threshold of 2000e, the v_{ds}-i_{ds} relation is in the linear region. Hence the thermal noise PSD is

$$d\langle i^2_{fb} \rangle = 4kT \frac{1}{2} g_{m,fb}\, df \tag{7.27}$$

Using the equation for g_m (eq.(7.9)), the thermal noise formula is similar to the shot noise expression:

$$d\langle i^2_{fb} \rangle = 2qi_{fb} \frac{1}{n}\, df \tag{7.28}$$

here n is 1.4, obtained by the circuit simulation.

- Thermal noise from the leakage current compensation circuit

  The transistor of the leakage current compensation circuit is also operated in weak inversion, so the thermal noise PSD is

$$d\langle i^2_{comp} \rangle = 4kT \frac{1}{2} g_{m,comp}\, df \tag{7.29}$$

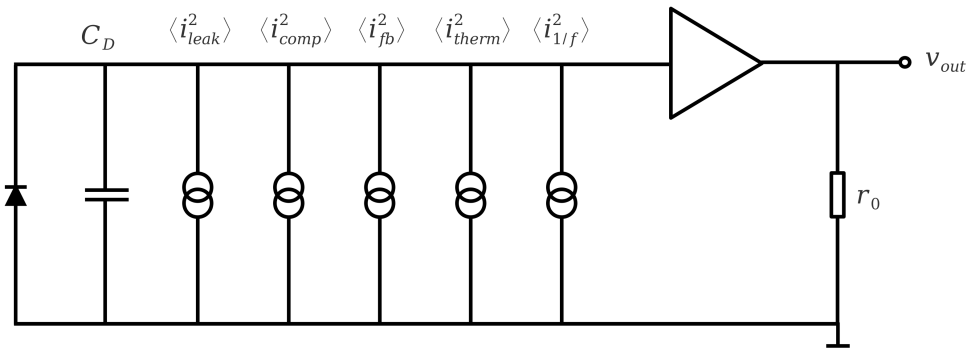

Figure 7.5: Simplified noise sources in a FE-I4 pixel readout. C_D is the capacitance of the sensor. $\langle i^2_{leak}\rangle$ is the shot noise from leakage current of the sensor. $\langle i^2_{comp}\rangle$ is the thermal noise from the leakage current compensation circuit. $\langle i^2_{fb}\rangle$ is the thermal noise from the feedback current source. $\langle i^2_{therm}\rangle$ and $\langle i^2_{1/f}\rangle$ are equivalent thermal and flicker noise sources from the NMOS of the preamp, respectively.

The compensating current $\langle i^2_{comp}\rangle$ is supposed to be the same as the leakage current $\langle i^2_{leak}\rangle$, therefore:

$$d\langle i^2_{comp}\rangle = 2qI_{leak}\frac{1}{n}\,df \tag{7.30}$$

Using the circuit in fig. 7.5 and the relation $\omega = 2\pi f$ to transform the frequency f into angular frequency ω, all the noise sources can be summarized in the following expression:

$$\langle i^2_{in}\rangle(\omega) = \frac{q(2i_{leak} + i_{fb})}{\pi}d\omega + \frac{K_F}{C_{OX}WL}C_D^2\omega d\omega + \frac{kT}{g_m\pi}C_D^2\omega^2 d\omega \tag{7.31}$$

Define the parameters:

$$C_{parallel} = \frac{q(2i_{leak} + i_{fb})}{\pi} \tag{7.32}$$

$$C_{1/f} = \frac{K_F}{C_{OX}WL}C_D^2 \tag{7.33}$$

$$C_{thermal} = \frac{kT}{g_m\pi}C_D^2 \tag{7.34}$$

The eq.(7.31) becomes

$$\langle i^2_{in}\rangle(\omega) = C_{parallel}d\omega + C_{1/f}\omega d\omega + C_{thermal}\omega^2 d\omega \tag{7.35}$$

By substituting $\langle i_{in}^2 \rangle$ (eq.(7.35)) and $H(j\omega)$ (eq.(7.21)) into eq.(7.13), the variance of the voltage at the output of the CSA is

$$\begin{aligned}
\langle v_{out}^2 \rangle &= \int_0^\infty \langle i_{in}(\omega)^2 \rangle \, |H(\omega)| \, d\omega \\
&= C_{parallel} \frac{\pi}{g_{ds,fb}^2} \frac{2\tau_b\tau_c(\tau_b+\tau_c)^2 + \tau_a^2(\tau_b^2+\tau_b\tau_c+\tau_c^2)}{4\tau_b\tau_c(\tau_b+\tau_c)^3} \\
&+ C_{1/f} \frac{1}{g_{ds,fb}^2} \frac{\tau_a^2(\tau_b-\tau_c)(\tau_b+\tau_c)(\tau_b^4+\tau_c^4)}{2\tau_b^2\tau_c^2(\tau_b^2-\tau_c^2)^3} \\
&+ C_{1/f} \frac{1}{g_{ds,fb}^2} \frac{\tau_b^2\tau_c^2\left[(\tau_b^2-\tau_c^2)^2 - \tau_a^2(\tau_b^2+\tau_c^2)\right]\left[ln(\tau_b^2/\tau_c^2)\right]}{2\tau_b^2\tau_c^2(\tau_b^2-\tau_c^2)^3} \\
&+ C_{thermal} \frac{\pi}{g_{ds,fb}^2} \frac{2\tau_b^2\tau_c^2(\tau_b+\tau_c)^2 + \tau_a^2(\tau_b^4+3\tau_b^3\tau_c+3\tau_b^2\tau_c^2+3\tau_b\tau_c^3+\tau_c^4)}{4\tau_b^3\tau_c^3(\tau_b+\tau_c)^3}
\end{aligned} \tag{7.36}$$

The time constants are calculated from the parameters listed in Table 7.1:

$$\tau_a = \frac{C_f}{g_m} \approx 0.075ns \tag{7.37}$$

$$\tau_b = \frac{C_f}{g_{ds,fb}} \approx 21.25ns \tag{7.38}$$

$$\tau_c = \frac{C_D}{g_m} \approx 0.15ns \text{ for diamond} \tag{7.39}$$

$$= \frac{C_D}{g_m} \approx 0.53ns \text{ for Si} \tag{7.40}$$

Since $\tau_b \gg \tau_c \approx \tau_a$, by comparing the orders of magnitude of the terms in eq.(7.36) and eliminating the negligible terms , eq.(7.36) is approximated to a simpler form:

$$\begin{aligned}
\langle v_{out}^2 \rangle &\approx C_{parallel} \frac{\pi}{g_{ds,fb}^2} \frac{1}{2(\tau_b+\tau_c)} \\
&+ C_{1/f} \frac{1}{g_{ds,fb}^2} \left(\frac{\tau_a^2}{2\tau_b^2\tau_c^2} + \frac{ln(\tau_b/\tau_c)}{\tau_b^2} \right) \\
&+ C_{thermal} \frac{\pi}{g_{ds,fb}^2} \left(\frac{1}{2\tau_b^2\tau_c} + \frac{\tau_a^2}{4\tau_b^2\tau_c^3} \right)
\end{aligned} \tag{7.41}$$

The $\langle v_{out}^2 \rangle$ is converted to Equivalent-Noise-Charge (ENC) by dividing the $\langle v_{out}^2 \rangle$ by the signal voltage corresponding to 1 electron, $V_q = \frac{q}{C_f}$:

$$ENC^2 = \frac{\langle v_{out}^2 \rangle}{V_q^2} = \frac{C_f^2}{q^2} \langle v_{out}^2 \rangle \tag{7.42}$$

The noise in units of ENC then yields the following expression:

$$ENC = \sqrt{\frac{(2i_{leak} + i_{fb})}{2q} \cdot \frac{\tau_b^2}{\tau_b + \tau_c} + \frac{C_D^2}{q^2}\frac{kT}{2g_m} \cdot \left[\frac{1}{\tau_c} + \frac{\tau_a^2}{2\tau_c^3}\right] + \frac{C_D^2}{q^2}\frac{K_F}{C_{OX}WL} \cdot \left[\frac{\tau_a^2}{2\tau_c^2} + \ln\left(\frac{\tau_b}{\tau_c}\right)\right]} \tag{7.43}$$

The ENC is plotted as a function of the determining parameters, C_D, i_{leak}, and τ_b. The C_D is determined by the sensor type, the i_{leak} increases with radiation damage, and the τ_b corresponds to the feedback current i_{fb} and therefore the signal shape.

Fig. 7.6(a) shows the noise contributions with respect to C_D. The dominant noise before irradiation is the thermal noise from the preamp, and is proportional to $\sqrt{C_D}$, indicating that the Si sensor will have higher noise than diamond.

After radiation damage, the shot noise from i_{leak} and the thermal noise from the i_{leak} compensation circuit increases with $\sqrt{i_{leak}}$ and their level is similar to the thermal noise from preamp when i_{leak} is around 100 nA (fig. 7.6(b)).

The parallel noise source is proportional to τ_b. In case of diamond, since it has tiny i_{leak}, the variation due to τ_b is negligible. However, in case of silicon after irradiation, longer shaping time leads to higher ENC, as shown in fig. 7.6(c).

However, beside the thermal noise considered in the analytical model, according to the AC simulation (see section 7.3) other thermal noise sources at the second stage amplifier, the biasing transistor, and the transistor for the Digital-to-Analog Converters (DACs)...etc. contribute 23% to 28% of the total noise, linearly dependent on the input capacitance C_D. This "baseline noise" contribution is added in the results in fig. 7.6(b).

7.3 Transient and AC simulations

The noise of the FE-I4 pixel readout is also estimated by simulations on the complete chip layout. Two kinds of simulations were performed: AC simulation and transient noise simulation. The software SPECTRE [83] was applied for the following simulations.

AC simulations

AC simulation is the most common approach for small signal, time invariant systems, of which the response of the circuit can be linearized around the DC operating point of the MOSFET. The signal and the noise are treated separately, assuming that they do not influence each other. The noise PSD is simulated in the frequency domain, and the noise PSD from each circuit units is simulated separately. By integrating the PSD and the transfer function over the full bandwidth of the circuit, the total voltage fluctuation at the output is obtained.

Transient noise simulations

In case of the charge sensitive amplifier of the FE-I4 pixel circuit, the transient noise simulation is more suitable, because the voltage across the drain and the source of the transistor as the feedback current source is varying with the time during the signal processing, so its DC operating point changes accordingly, too. Since the ENC of interest is the signal fluctuation about

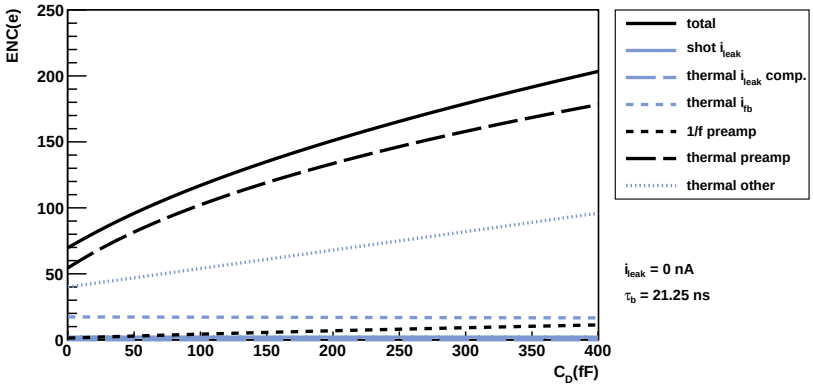

(a)

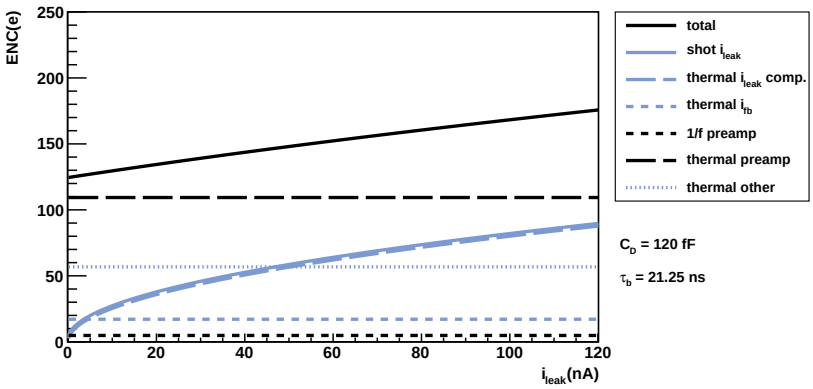

(b)

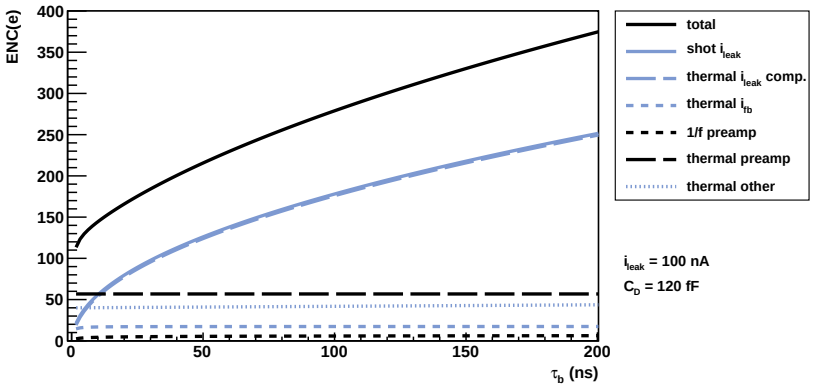

(c)

Figure 7.6: Equivalent noise charge (ENC) calculated by the analytical model versus (a) input capacitance C_D (b) leakage current i_{leak} (b) shaping time constant τ_b. The black solid line is the total ENC. The gray solid line is the shot noise from the sensor leakage current i_{leak}. The gray long dashed line is the thermal noise from the i_{leak} compensation circuit. The gray short dashed line is the thermal noise from the feedback current source i_{fb}. The black short dashed line is the 1/f noise of the preamp. The black long dashed line is the thermal noise of the preamp. The gray dotted line is the thermal noise from other components, obtained by the AC simulation. The i_{leak}, C_D, τ_b applied in the calculation are annotated beside the plots.

the applied threshold voltage, the transient noise simulation, which allows to simulate noise in the time domain as a part of the signal fluctuation must be applied. This method provides more realistic noise studies of non-linear and non-time-invariant systems.

In transient noise simulations, each component of the circuit contains noise sources generating random fluctuations in the time domain with the appropriate PSD. The circuit voltage and the current are then computed solving differential equations by effective Monte-Carlo methods. The result is the signal with random fluctuations at the output of the circuit. By repeating the signal simulation many times, the variance of the voltage $\langle v_{out}^2 \rangle(t)$ at a certain time t can be measured, and $\langle v_{out}^2 \rangle(t)$ can be converted to ENC. The circuit voltages and currents are then computed solving differential equations by effective Monte Carlo methods. This method allows more realistic noise studies of non-linear and non-time invariant systems, covering the noise frequency band from 10 kHz to 1 GHz.

The results of the simulations are plotted in fig. 7.7(a), fig. 7.7(b), fig. 7.7(c). The AC simulation shows the contribution from each components in the circuit, but it underestimated the noise. Comparing the simulation (fig. 7.7(a)) and calculation (fig. 7.6(a)), the most obvious difference is that the thermal noise from other components that are missing in the calculation model contribute 23% to 28% depending on C_D when i_{leak} is 0. Therefore the relation between the ENC and the C_D tends to be linear in AC and transient noise simulation. When the i_{leak} increases and the shot noise becomes the dominant noise, then the discrepancy due to the other components is not significant.

The thermal noise from the i_{leak} compensation circuit saturates when i_{leak} increases, because the limit of the compensation was designed to be 100 nA.

The calculation, AC simulation, and transient noise simulation are compared in the next section.

7.4 Comparison of models and simulations

The results of ENC from the calculation, AC simulation, and transient noise simulation are summarized in fig. 7.8. The measurements from FE-I4 modules are compared to the calculation and simulation, too. The methods of noise measurement are described in section 4.3.

The ENC versus C_D is shown in fig. 7.8(a), versus i_{leak} is shown in fig. 7.8(b). The transient simulation agrees with the real measurement in the 1-σ range. The AC simulation tends to underestimate the ENC. The calculation shows a $\sqrt{C_D}$ dependence, but the transient shows a linear rise with respect to C_D. The main reason might be that calculation picks the most essential components of the pixel readout circuit, however when the C_D is small and the serial noise is not dominating, the noises from the missing components, such as the the transistor for the DACs, discriminators, biasing current sources, and the components in the second stage amplifier can contribute significantly to the ENC, too. The difference between the noise ENC of diamond and silicon pixels is not significant before the irradiation (see fig. 7.8(b)). While i_{leak} increases after irradiation, the noise of diamond remains unchanged because of its tiny i_{leak}. On the other hand, the ENC of Si is doubled when $i_{leak} \approx 100$ nA, due to the shot noise from i_{leak}.

Because the transient noise includes the noise from all the noise contributions from all components, and considers the non-linear and time-variant behavior of the circuit, it is supposed to be the most reliable estimation. Therefore it will be applied in the following SNR estimations.

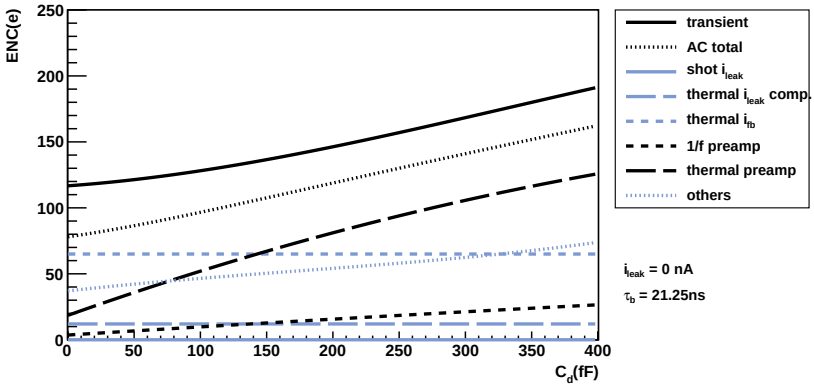

(a)

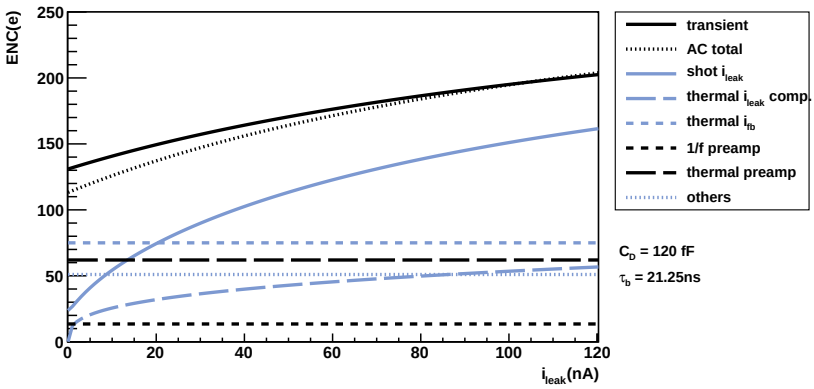

(b)

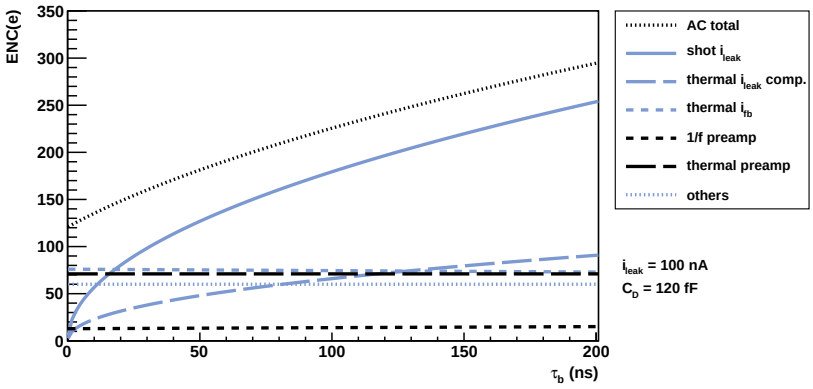

(c)

Figure 7.7: Equivalent noise charge (ENC) obtained by transient simulation and AC simulation versus (a) input capacitance C_D (b) leakage current i_{leak} (b) shaping time constant τ_b. The black solid line is the total ENC of transient simulation. The black dotted line is the total ENC of AC simulation. The gray solid line is the shot noise from the sensor leakage current i_{leak}. The gray long dashed line is the thermal noise from the i_{leak} compensation circuit. The gray short dashed line is the thermal noise from the feedback current source i_{fb}. The black short dashed line is the 1/f noise of the preamp. The black long dashed line is the thermal noise of the preamp. The gray dotted line is the thermal noise from other components, obtained by the AC simulation. The i_{leak}, C_D, τ_b applied in the calculation are annotated beside the plots.

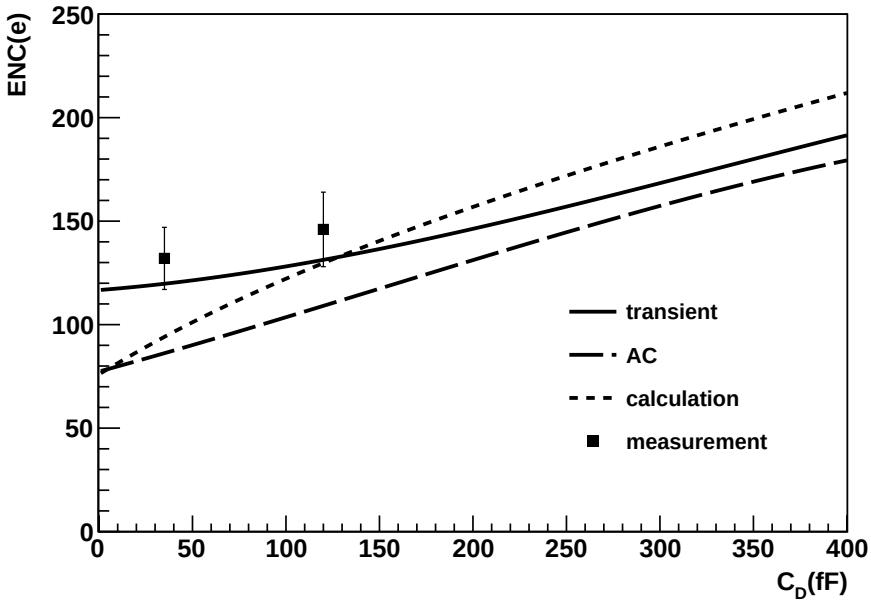

(a)

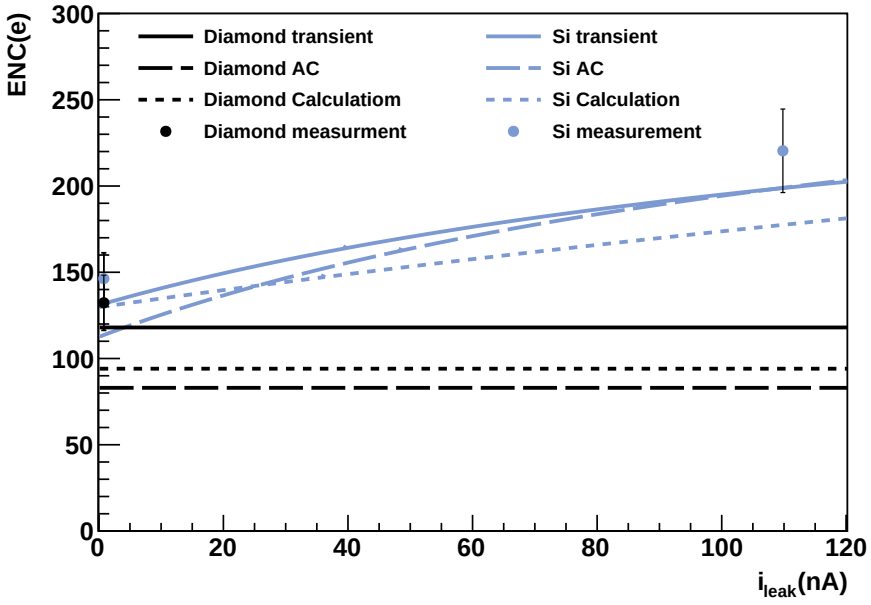

(b)

Figure 7.8: Comparison of Equivalent Noise Charge (ENC) obtained by transient noise simulation, AC simulation, and calculation (a) versus input capacitance C_D (b) versus leakage current i_{leak} of Si sensors, not that i_{leak} in diamond is negligible. The solid lines, long dashed lines, and dotted lines are the results of transient noise simulation, AC simulation, and calculation, respectively. The markers show measurements form pixel detectors with FE-I4 readout. The error bars show the uncertainty of the measurement, which is calculated by $\left(\sigma_{pix}^2 + \sigma_{calib}^2\right)^{\frac{1}{2}}$, where σ_{pix} and σ_{calib} are the pixel-to-pixel variation and uncertainty from the calibration, respectively. In (b), the gray lines and markers are for Si, and the black are for diamond.

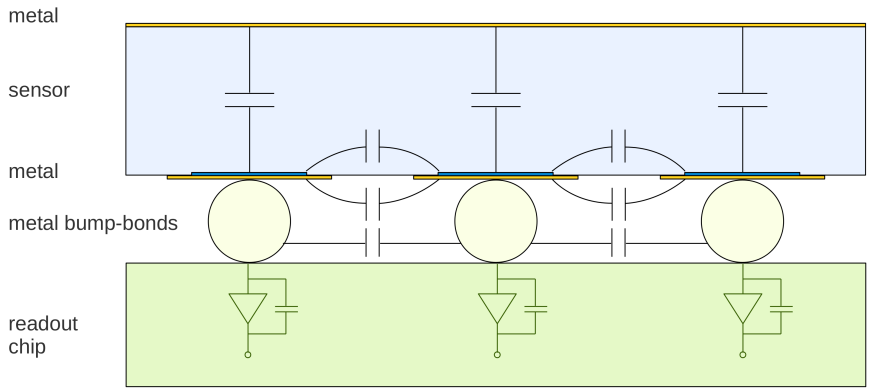

Figure 7.9: Contributions of input capacitances.

7.5 Noise versus irradiation

To estimate the development of ENC of the pixel detectors with respect to the increasing irradiation, the input capacitance C_D and the leakage current i_{leak} should be determined. The measurement of C_D is presented in section 7.5.1, and i_{leak} as a function of irradiation in section 7.5.2. Then they are plugged in the model and the simulations to get the ENC as a function of irradiation, as shown in section 7.5.3.

7.5.1 Determination of input capacitance

The input capacitance to the preamplifier (C_D) is a sum of many contributions, as illustrated in fig. 7.9. The dominating one is the inter-pixel capacitance, and the minor contributions are form the pixel-to-backside capacitance, the stray capacitance through the air between the sensor and the chip, the metal pads, bump-bonds, and even the capacitance from the transistor in the CSA in the chip.

In case of diamond pixels , the capacitance is geometrically defined by the pixel metallization and its dielectric constant. However, in case of Si, besides the pixel geometry and dielectrics, the implants, biasing grid, and guard rings influence the inter-pixel capacitance, too.

The C_D of a FE-I4 pixel has never been exactly measured in the past. Therefore, the FE-I4 was designed for a range of input capacitance from 0 to 400 fF. In order to obtain reliable numbers for C_D of diamond and Si pixels with FE-I4 pixel size and pitch, a capacitance measurement chip (PixCap) has been developed by M. Havranek [84]. The chip is bonded to the sensors with FE-I4 metalization by bump-bonds, and all the contribution to the input capacitance can be individually determined.

The essential design of PixCap is a switching circuit (fig. 7.10(a)) with two switches charges and discharges the capacitance with a chosen frequency f. By measuring the average current

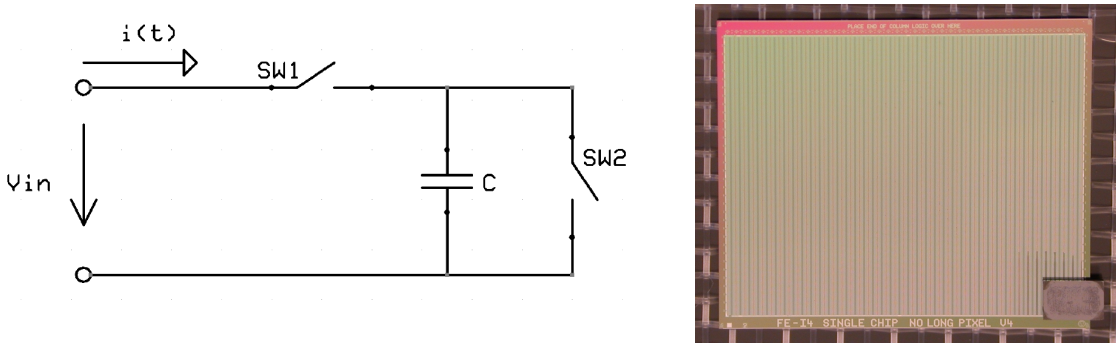

(a) (b)

Figure 7.10: (a) Circuit principle of the PixCap chip. (b) Picture of the PixCap chip (the small chip at the bottom right corner of the picture) bonded to a Si sensor.

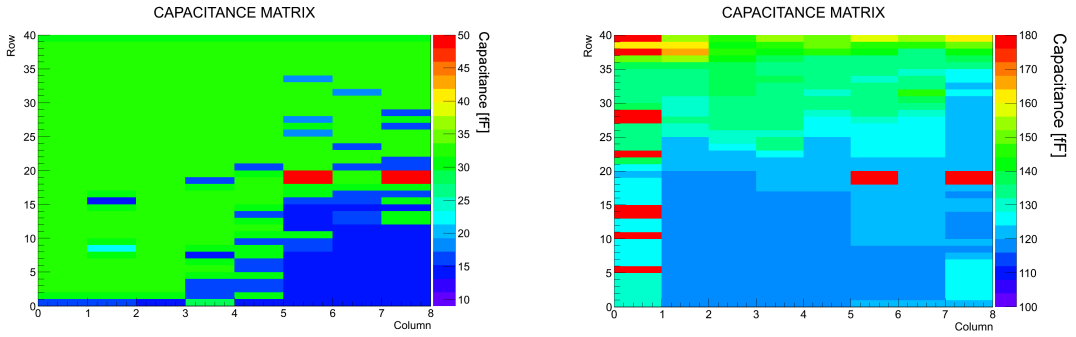

(a) (b)

Figure 7.11: Capacitance maps of (a) a 450 μm thick diamond pixel sensor (60V) and (b) a 250 μm thick planar silicon pixel sensor (60V, fully depleted) measured with the PixCap chip. The sensors are unirradiated. Two pixels are marked red as test pixels. The area with low capacitance measurements in (a) is due to bonding problems.

and the frequency the capacitance is extracted:

$$C = \frac{Q}{V_{in}} = \frac{\int Idt}{V_{in}} = \frac{\langle I \rangle - \langle i_{leak} \rangle}{V_{in} \times f} \tag{7.44}$$

where V_{in} is the input voltage and f the switching frequency.

The measurements yield the following results. Without any sensor bonded, the capacitance is 11 fF, which is the capacitance through the air, the metal pad, and the bump-bonds on the PixCap chip. Bonded to a diamond sensor the map of measured pixel capacitances is shown in fig. 7.11(a). The sensor was biased with 60V, although no dependence of the bias voltage is observed. The average pixel capacitance measured for diamond is

$$\langle C_D^{diamond} \rangle = 35 \text{ fF}$$

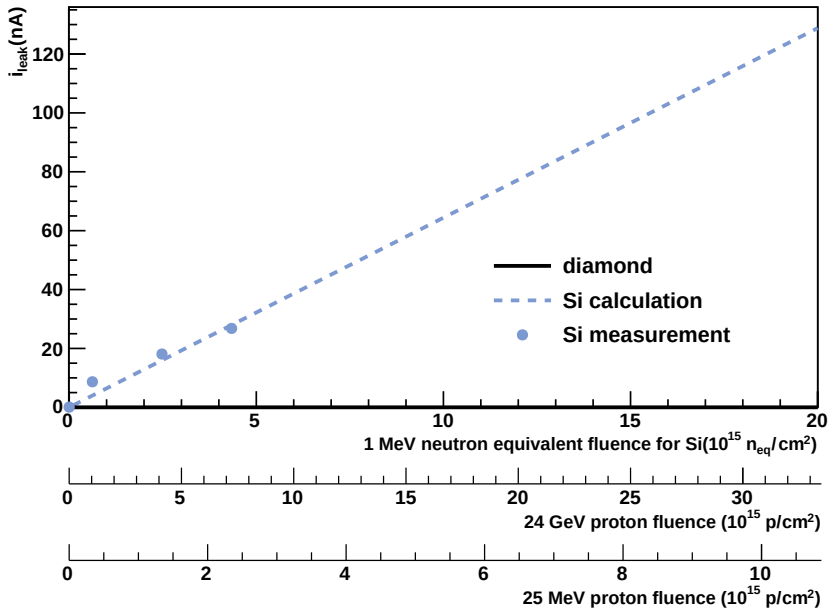

Figure 7.12: Leakage current in a FE-I4 pixel cell -10°C with respect to the radiation fluence. The black solid line is for diamond. The gray dashed line is for Si by calculation, assuming the sensors are annealed at 60°C for 80 minutes. The gray circles are the measurement on planar-Si [85], scaled from the measurement on FE-I3 pixel cell by the volume of the sensor bulk. The fluence of 25 MeV protons, 24 GeV protons, and the 1 MeV neutron equivalent fluence for Si are displayed by the multiple axes.

For silicon there is a dependence on the applied bias voltage until the sensor is fully depleted and neighboring pixels are isolated. For unirradiated sensors this is the case for voltages above 60 V. The measured capacitance map is shown in fig. 7.11(b). The average value for silicon is

$$\langle C_D^{Si} \rangle = 120 \text{ fF}$$

7.5.2 Determination of leakage current

While the leakage current (i_{leak}) grows with the radiation damage, the shot noise becomes the dominating noise source. The i_{leak} in diamond is negligible because of its large band gap, but in Si the i_{leak} follows the NIEL scaling hypothesis (see section 6.1.3):

$$i_{leak} = i_{leak,0} + \alpha_i \Phi_{eq} \cdot V \tag{7.45}$$

where α_i is the damage factor known for silicon to be $\alpha = (3.99 \pm 0.3) \times 10^{-17} \frac{A}{cm}$ [57] if the sensors are annealed at 60°C for 80 minutes and thus i_{leak} can be calculated. The Φ_{eq} is the neutron equivalent fluence, which is defined by $\Phi_{eq} = \kappa\Phi$. For 24 GeV proton irradiation, κ is 0.6. For 25 MeV proton, κ is 1.85. V is the volume of the sensor bulk.

Furthermore, a temperature correction has been applied using eq.(6.6) and eq.(6.7), because the typical operation temperature (T) at LHC is -10°C. The calculated i_{leak} versus the irradiation dose is show in fig. 7.12. The numbers care calculated for a FE-I4 pixel with sensor bulk

250 µm × 50 µm × 200 µm. The fluence of 25 MeV and 24 GeV protons are displayed by the multiple axes.

The calculated i_{leak} is compared to the measurement done by P. Weigell et al. [85], which is measured using planar-Si sensors bump-bonded to FE-I3 chip with the volume 400 µm × 50 µm × 300 µm, biased by 750 V voltage. To be compared to the calculation for FE-I4 sensors, whose volume is smaller than the FE-I3 pixels, the measured i_{leak} is scaled by the ratio between the volume of FE-I4 and FE-I3 pixels. The comparison shows that the estimation agrees with the measurements.

Even if assumed to be zero before irradiation, i_{leak} of Si can become fairly large (O(100 nA)) for large fluence as expected at the LHC. On the other hand, the i_{leak} of diamond remains negligible versus the radiation damage.

7.5.3 Noise versus irradiation

With the ingredients from the previous sections, the model and the simulation can be applied to estimate the ENC for diamond and Si pixels. The final results are the prediction of ENC as a function of proton radiation fluence, see fig. 7.13.

Before irradiation, the noise of diamond and Si are similar. While the radiation fluence increases, the noise of diamond remains the same, but the noise of Si increases due to the shot noise from the leakage current. Protons with lower energy is more damaging than high energy ones, so the noise increases faster as well. When the proton fluence exceeds 10^{16} p/cm^2, the noise of Si pixel detector is 2 times that of the diamond ones.

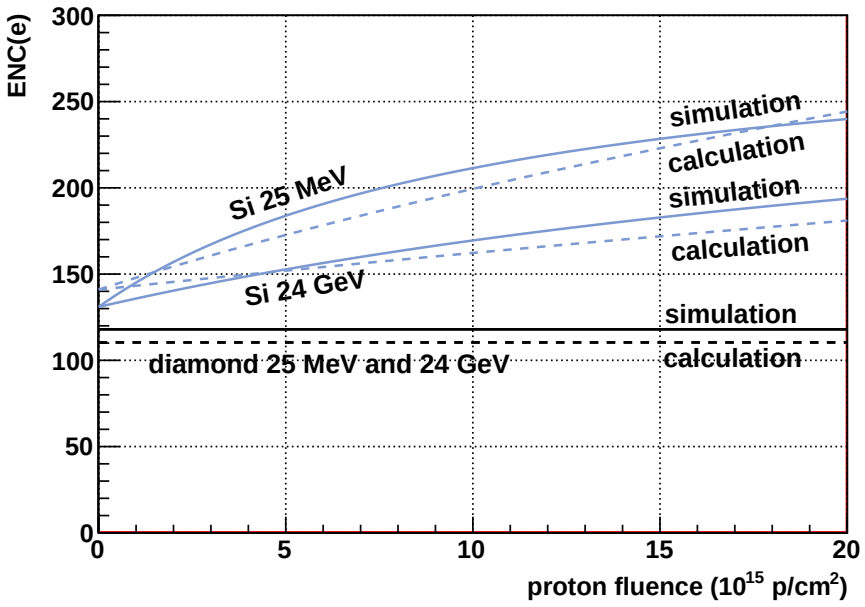

Figure 7.13: ENC with respect to the proton irradiation fluence. The black lines are for diamond, and the gray lines are for Si. The solid and dashed lines shows the estimation by transient simulation and analytical calculation, respectively. The results of 25 MeV and 24 GeV proton irradiation are annotated on the plot.

Chapter 8

Signal-to-Noise Ratio

By combining the investigations on signal and noise in the previous chapters, the Signal-to-Noise Ratio (SNR) of diamond and silicon pixel detector is estimated as a function of radiation fluence, and summarized in this chapter. Besides SNR, which represents the sensitivity to the charged particles passing through the pixel detector, efficiency and fake probability are also important indices to qualify the accuracy of detection. The estimation of efficiency and fake probability are presented in this chapter, too.

8.1 SNR comparison for sensors of 200 μm thickness

The SNR calculation is done for a given pixel sensor thickness of 200 µm , which is the designed thickness of the ATLAS inner pixel detectors. Protons of 25 MeV and 24 GeV energy are chosen as the damaging radiation, since they represent the low and high ends of the energy spectrum of the particles at the LHC, and also because for diamond a universal scaling hypothesis for radiation damage, e.g. NIEL hypothesis, is still unavailable.

The signal is calculated by the following equation:

$$S(\Phi) = Q_{collected} = Q_{ionized} \times \sum_{i=e,h} \frac{\lambda_i(\Phi)}{d} \left[1 - \frac{\lambda_i(\Phi)}{d} \left(1 - e^{\frac{d}{\lambda_i(\Phi)}} \right) \right] \tag{8.1}$$

The $Q_{ionized}$ is calculated by the restricted energy loss calculation, eq.(5.5). The mean free path $\lambda(\Phi)$ as a function of fluence Φ is described by the damage curve eq.(6.34) and the damage constants in Table 6.4. The noise used in the SNR calculation is the simulated transient noise, as show in fig. 7.13.

The results are plotted in fig. 8.1. It shows that for a 200 µm thick sensor, the sensitivity of diamond pixel sensors in terms of SNR exceeds the Si one above fluence of about 7×10^{15} p/cm^2 (24 GeV proton) or 1×10^{15} p/cm^2 (25 MeV proton). The results interpret that the diamond is more prevailing than Si in low energetic radiation environments.

8.2 SNR comparison for sensors with the same radiation length

The material budget, i.e. how much material a pixel detector constitutes is crucial in design considerations for collider experiments. The material budget is characterized by the radiation length, X_0, the mean distance over which a high-energy electron loses all but $1/e$ of its energy in the material. Longer radiation length is favorable for the inner detectors, because it means less conversion of electrons into photons and less multiple scattering of particles in the detector,

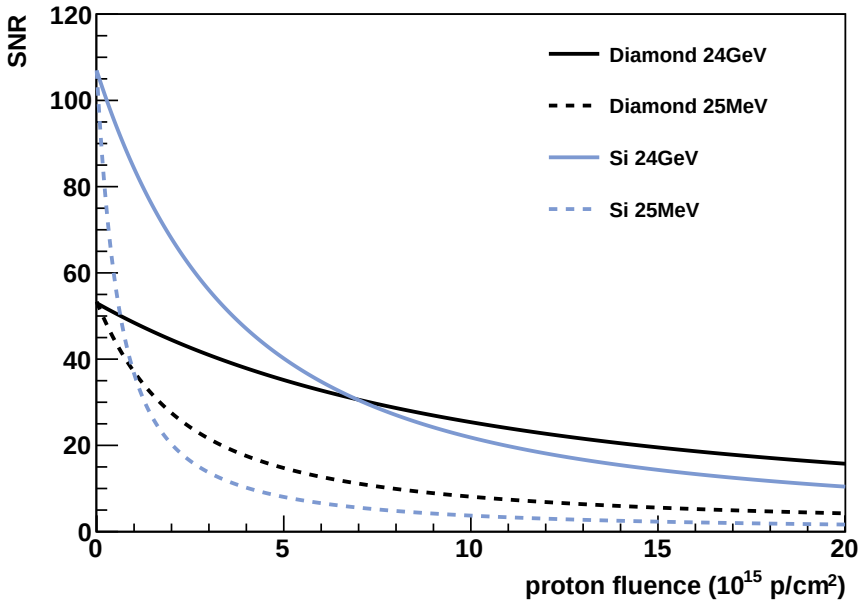

Figure 8.1: SNR for sensors of 200 μm thickness with respect to the proton radiation fluence. The black lines show the SNR of diamond pixel detector, and the gray ones are of Si. The solid and dashed lines are for the SNR versus 24 GeV proton and 25 MeV fluences, respectively.

so that the tracking is more precise. Therefore a comparison between the diamond and Si at the same radiation length (here $0.1\%X_0$) is appropriate.

Fig. 8.2 shows the same dependence as fig. 8.1, but for sensors with the same thickness of $0.1\%X_0$. The signal in a sensor of $0.1\%X_0$ thickness is normalized from the signal in 200 µm thick sensor. $0.1\%X_0$ is 121 µm for diamond and 94 µm for Si. The noise is again the ENC from transient noise simulation. Due to the longer radiation length of diamond, the turn-over in the diamond - silicon comparison moves to lower radiation fluence, namely to about 3.8×10^{15} p/cm^2 (24 GeV proton) or 0.8×10^{15} p/cm^2 (25 MeV proton).

The measured SNR of diamond pixel detectors before and after irradiation by 25 MeV protons have been presented in section 4.4. To compare the measured SNR to the estimation shown in fig. 8.2, the signal in the diamond sensors of $0.1\%X_0$ thickness are normalized from the measured signal in 507 µm (DDL7, the unirradiated one) or 542 µm (DDL4, the irradiated one) thick sensors. The numbers of the measured and calculated/simulated signal, noise, and SNR are summarized in Table 8.1. The normalized SNR of an unirradiated sensors is (30.5±4.9). In case of the diamond irradiated by 25 MeV protons with 5×10^{15} p/cm^2 of fluence, the normalized SNR is (8.57±1.28). As shown in fig. 8.2, the measured SNR agree with the estimation with in the 1 σ range, which means that the prediction is precise and the diamond pixel detector has great radiation tolerance.

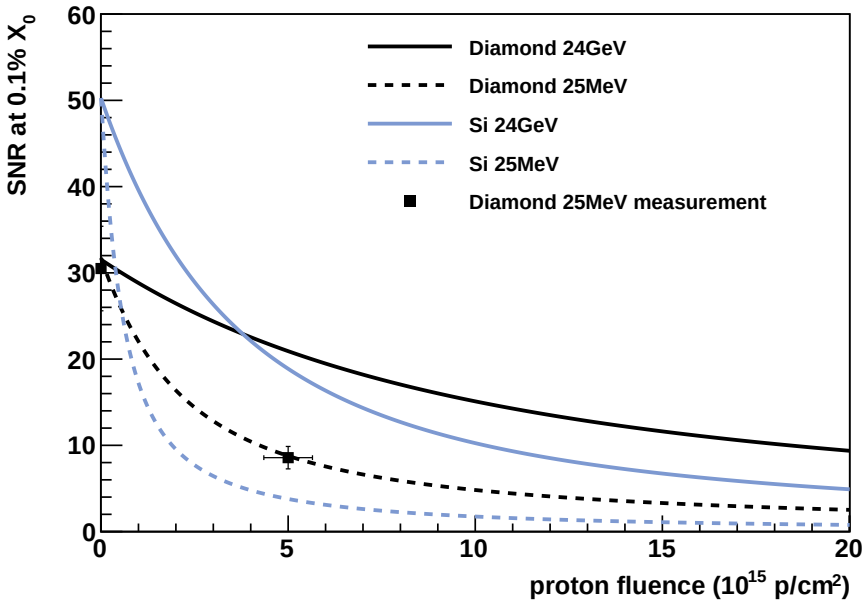

Figure 8.2: SNR for sensors with $0.1\%X_0$ thickness with respect to the proton radiation fluence. $0.1\%X_0$ is 121 µm for diamond and 94 µm for Si. The black lines show the SNR of diamond pixel detector, and the gray ones are of Si. The solid and dashed lines are for the SNR versus 24 GeV proton and 25 MeV fluences, respectively. The square markers show the measured SNR of sCVD diamond pixel detectors irradiated by 25 MeV protons.

Table 8.1: Comparison of measured and eastimated signals, noise, and SNR for sensors of $0.1\%X_0$ thickness for the unirradiated (DDL7) and the irradiated diamond (DDL4). The calculation is done by eq.(5.9) for MPV and eq.(6.32) for the charge-loss with respect to the irradiation. The noise is from the transient noise simulation presented in chapter 7.3. $0.1\%X_0$ of diamond is 121 μm.

diamond	DDL7	DDL4
thickness	507 µm	542 µm
irradiation	0	5×10^{15} p/cm^2
MPV by calculation	17228 e	4994 e
MPV by measurement	(17200±1720) e	(4848e±485) e
noise by simulation	120 e	120e
noise by measurement	(135±17) e	(135±15) e
SNR for sensors with $0.1\%X_0$ of thickness by estimation	31.8	8.75
SNR for sensors with $0.1\%X_0$ of thickness by measurement	30.5±4.9	8.57±1.28

8.3 Efficiency and fake probability

In a pixel detector the signal must exceed a threshold to be recorded, so the efficiency and fake probability of the detection are interesting for system optimization. The definition of the efficiency is

$$\text{efficiency} = \frac{\text{number of accepted signal pulses}}{\text{total number of signal pulses}} \tag{8.2}$$

The actual signal from the sensor is nearly Gaussianly distributed, of which the mean is the average signal ($Q_{collected}$), and the sigma of the Gaussian distribution is the total fluctuation:

$$\sigma(\Phi) = \sqrt{\sigma_{noise}(\Phi)^2 + \sigma_{signal}(\Phi)^2 + \sigma_{threshold}^2} \tag{8.3}$$

where the $\sigma_{noise}(\Phi)$ is the electronic noise of a pixel, $\sigma_{signal}(\Phi)$ is the variation (width) of the signal spectrum. Both $\sigma_{noise}(\Phi)$ and $\sigma_{signal}(\Phi)$ can be estimated as functions of radiation fluence Φ. The $\sigma_{threshold}$ is the threshold dispersion of all the pixels. It should be a constant at all radiation fluences.

The probability of such a signal to be below the threshold is expressed by the cumulated distribution function $F(z)$, which is the integral of a Gaussian distribution from negative infinity to a certain number z:

$$F(z) = P(Z \leq z) = \int_{-\infty}^{z} \frac{1}{\sqrt{2\pi}} e^{-\frac{(x-\mu)^2}{2\sigma^2}} dx \tag{8.4}$$

the μ is the mean of the Gaussian distribution, and σ is the sigma.

The integral is formulated by the error function, erf, therefore

$$F(z) = \frac{1}{2}\left[1 + erf\left(\frac{z-\mu}{\sqrt{2\sigma^2}}\right)\right] \tag{8.5}$$

and the probability of a signal to exceed the threshold is $1 - F(z)$.

For the calculation of efficiency, the following parameters are used: The threshold z is between 1000 and 2000 electrons. The average signal μ is calculated using eq.(8.1). The charge loss due to charge sharing between pixels are not considered. The total fluctuation $\sigma(\Phi)$ is calculated by eq.(8.3), where $\sigma_{noise}(\Phi)$ is the electronic noise given by transient simulation, $\sigma_{threshold}$ is the threshold dispersion with a typical number of 30 electrons, $\sigma_{signal}(\Phi)$ is the width of the energy loss spectrum of the signal, which depends on the thickness of the sensor and the uncertainty from the cluster reconstruction. It should be measured using the 200 µm sensor with FE-I4. 25% of the MPV is assumed based on the measurement result shown in the previous section.

The efficiency with respect to the proton irradiation and the threshold is then plotted in fig. 8.3. The fluence and the threshold are the two axes, and the efficiency is indicated by the color code. In case of 25 MeV proton irradiations on diamonds with 2000e threshold, the efficiency starts to decrease at 2.5×10^{15} p/cm^2, and the signal spectrum is completely below the threshold when the proton fluence is more than 7×10^{15} p/cm^2. Decreasing the threshold helps to gain more efficiency. In contrast the noise increases, and the result of the combined effect is that the efficiency remains 100% up to 3.8×10^{15} p/cm^2. The signal is completely gone when the fluence is mare than 10^{16} p/cm^2. For Si the efficiency decreases faster than for

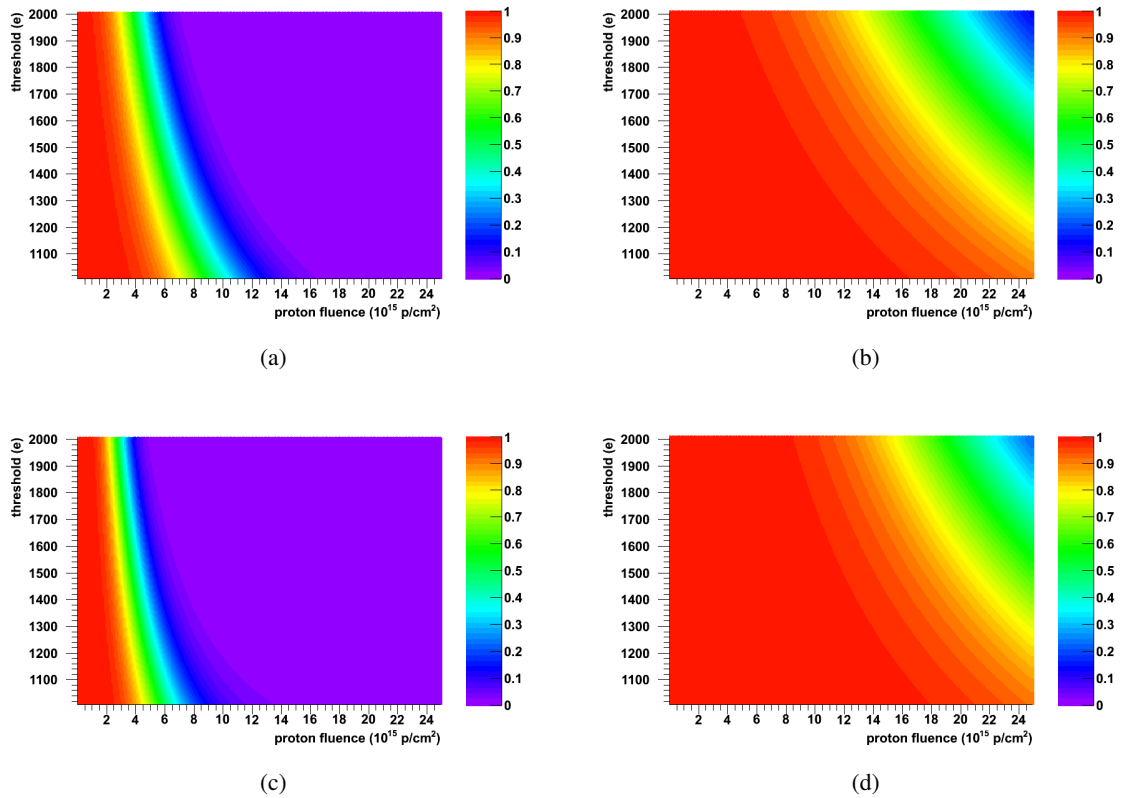

Figure 8.3: Efficiency of FE-I4 pixel detectors with respect to radiation fluence and threshold configuration. The sensor thickness is assumed to be 200 µm. The color code indicates the efficiency. Four combinations of sensors and radiation types are shown : (a) Diamond irradiated by 25 MeV protons, (b) Diamond irradiated by 24 GeV protons, (c) Si irradiated by 25 MeV protons, (d) Si irradiated by 24 GeV protons.

diamond, mainly due to its weaker radiation tolerance comparing to diamond, which means that the signal in Si decreases faster than in diamond as a function of the proton fluence.

In case of 24 GeV proton irradiations with threshold of 2000 electrons, the efficiency remains 1.0 until the proton fluence is 4.0×10^{15} p/cm^2 for diamond and 8.0×10^{15} p/cm^2 for Si. If the threshold descents to 1000 electrons, the efficiency can remain 100% up to 1.6×10^{16} p/cm^2. The efficiency of diamond pixels is lower than of Si ones for high energy radiation damage, again mainly because the 24 GeV protons are less damaging than the 25 MeV protons. Therefore the influence of the charge loss is less significant.

The definition of fake probability is as following:

$$\text{fake probability} = \frac{\text{number of noise hits accepted as signal}}{\text{total number of noise hits}} \tag{8.6}$$

The average noise amplitude is 0, so in case of fake probability the mean μ is 0, and the fluctua-

tion σ_{fake} is the quadrature addition of noise $\sigma_{noise}(\Phi)$ and the threshold dispersion $\sigma_{threshold}(\Phi)$:

$$\sigma_{fake} = \sqrt{\sigma_{noise}(\Phi)^2 + \sigma^2_{threshold}} \tag{8.7}$$

Therefore, the fraction of noise hit under the threshold is

$$F(z) = \frac{1}{2}\left[1 + erf\left(\frac{z-0}{\sqrt{2\sigma^2_{fake}}}\right)\right] \tag{8.8}$$

and the fake probability is $1 - F(z)$.

The result is presented in fig. 8.4. The fake probability of diamond is quasi 0 at all radiation fluence. It keeps unchanged versus irradiation because the noise is constant around 135 electrons, which shows the advantage of tiny leakage current. Only if the threshold is as low as 1000 electrons, the fake probability is in the order of 10^{-14} since the threshold is only 7.4σ away from mean (1000/135=7.4). Si pixels suffer from the increasing noise with respect to the fluence, and the fake probability becomes significant while the damaging fluence is in the order of 10^{16} p/cm^2, especially with low thresholds. The fake probability is in the order of 10^{-5} and 10^{-6} for 25 MeV and 24 GeV protons, respectively. The fake probability can be kept quasi 0 if the threshold is higher than 1200 electrons.

To summarize, in high radiation environments the fake probability due to the noise is not a problematic issue compared to the rapid decrease of the efficiency due to charge loss. To remain at the 100% efficiency level of detection during the whole period of HL-LHC operation, diamond pixel detectors with sensors thicker than 200 μm is suggested.

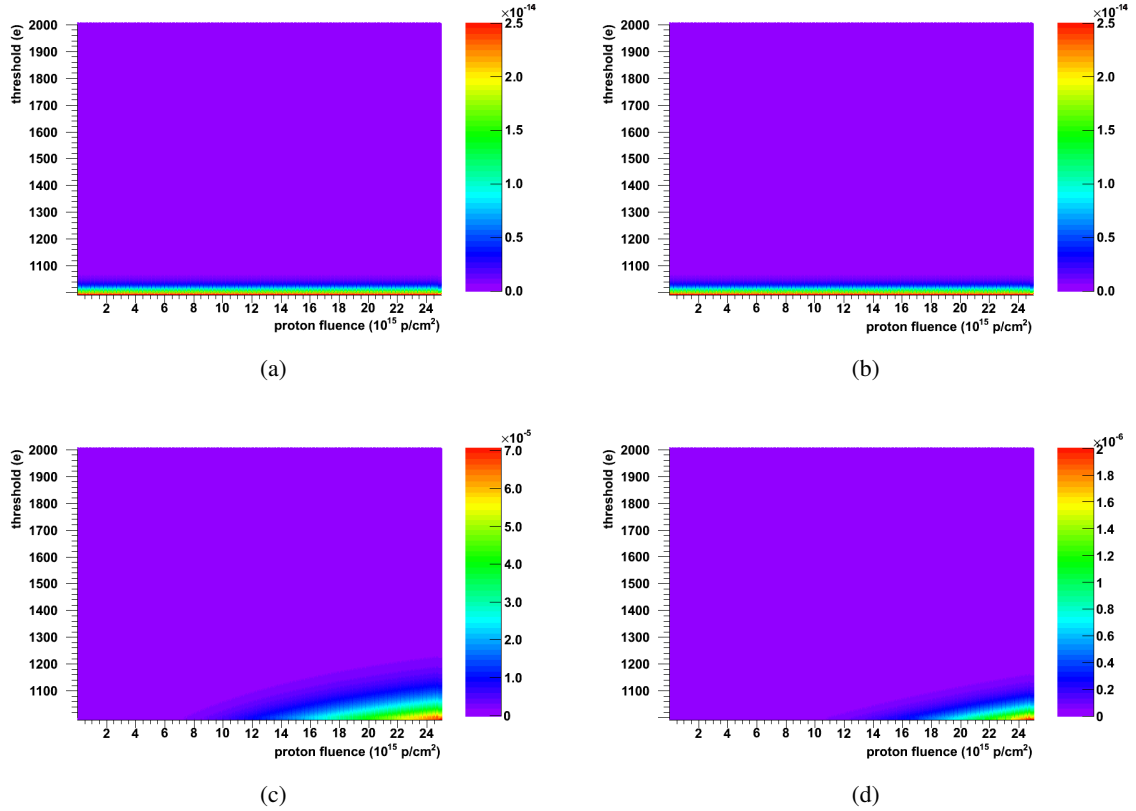

(a) (b)

(c) (d)

Figure 8.4: Fake probability of FE-I4 pixel detectors with respect to radiation fluence and threshold configuration. The sensor thickness is assumed to be 200 µm. The color code indicates the fake probability. Four combinations of sensors and radiation types are shown :(a) Diamond irradiated by 25 MeV protons (b) Diamond irradiated by 24 GeV protons (c) Si irradiated by 25 MeV protons (d) Si irradiated by 24 GeV protons.

Chapter 9

Conclusions

In 2020 the High-Luminosity Large Hadron Collider (HL-LHC) will open a new luminosity domain for collider experiments. Particle fluence of 2 to 3×10^{16} p/cm^2 is expected in 10 to 12 years of HL-LHC operation. This radiation level is far beyond the limits of the current design for vertex detectors, so new radiation hard sensor and readout electronics must be developed for the coming upgrade. Diamond is a promising choice for sensor material mainly because of its great radiation tolerance and negligible leakage current. Whether the diamond pixel detector is applicable in the HL-LHC is very interesting for the future technology of vertex detection. In this thesis, the performance of the state-of-the-art diamond pixel detector is compared to the well-understood Si ones. The assessment has been achieved by comparing their SNR with respect to the radiation damage.

For the first time, sCVD diamonds were bump-bonded to the most recent ATLAS pixel readout chips FE-I4, and the signal and noise of the sCVD diamond pixel detectors were measured before and after irradiation (chapter 4). The pixel modules were characterized in the laboratory using the radioactive sources. Full signal charge collection is observed before irradiation, in our case it was 17200 electrons collected in 507 μm of diamond. After being damaged by 25 MeV protons with the fluence of 5×10^{15} p/cm^2, the irradiated diamond pixel detector can still collect 26% of signal charges. The electronic noise is measured by the S-curve method. For the diamond pixel detector the noise is 135 electrons, not affected by the irradiation. These measurements on signal and noise provide the references for further evaluation of SNR using calculations and simulations.

Investigations for the signal in diamond and Si are divided into 2 parts. The first part is the generation of signals in the sensor by ionizing energy loss of the traversing high energy particle (chapter 5). Theories of the energy loss with respect to the $\beta\gamma$ of the traversing particle was applied to diamond and Si to calculate the number of signal charges. The dominating parameters for signal generation are (1) the density of the material (2) the energy required to generate an electron-hole pair in the material. Diamond has the advantage over Si in its density (3.52 g cm^{-3} of diamond > 2.33 g cm^{-3} of Si) leading to more energy deposition by the particle. However the energy required to generate an electron-hole pair in diamond is 3.6 times of Si (13.1 eV > 3.61 eV), which means that the signal generated in diamond is eventually smaller than in Si before irradiation. Calculation results show that in 200 μm of sensors, 1 GeV pion can generate 6300 electron-hole pairs in diamond, and 14000 pairs in Si.

The second part of signal studies focuses on the signal loss due to radiation damage (chapter 6). The formulation of signal loss due to trapping as a function of radiation fluence has been developed in terms of the mean free path of charge carriers. Diamond pad detectors were used to measure the signal loss with respect to proton irradiation, and the results were compared to the published Si data, showing that diamond is about 3 times radiation harder than Si in the

scope of trapping. Because of the great radiation hardness, although the signals in diamond is much smaller than in Si before irradiation, their signal levels become similar after damaged by 10^{16} p/cm^2 of proton fluence.

Investigations for the electronic noise from a pixel readout circuit were performed by analytical calculation and simulations (chapter 7). With the key parameters, leakage current and input capacitance to the preamplifier, the noise can be estimated for planar sensors with pixel readout at any radiation fluence. PixCap chip has been developed and bump-bonded to diamond and planar-Si pixel sensors to measured the input capacitance. The measured input capacitances is 35 fF for diamond and 120 fF for Si with the FE-I4 pixel readout metalization. The dominating contribution of noise is the shot noise from the leakage current in the sensor, so the noise of Si pixels increases in radiation environments, while the noise of diamond remains the same. When the radiation fluence in the order of 10^{16} p/cm^2, the simulated noise of diamond pixel is around 110 electrons, and of Si around 200 electrons.

With all the ingredients from chapter 5 to chapter 7, the SNR was evaluated as a function of radiation fluence, and the result reveals that the SNR of diamond pixels can exceed that of planar-Si when the radiation fluence is above 10^{15} p/cm^2. The prediction by the evaluation agrees with the results of measurement in chapter 4.

Diamond pixel detectors showed great radiation tolerance in this study. Further characterization such as high energy beam tests with precise tracking to measure the position resolution or detection efficiency are anticipated to prove the applicability in the collider experiments.

Bibliography

[1] **ATLAS** Collaboration, "The ATLAS Official Website." http://www.atlas.ch/, 2012.

[2] L. Evans and P. Bryant, *LHC Machine*, *JINST* **3** (2008), no. 08 S08001.

[3] **ATLAS** Collaboration, *The ATLAS Experiment at the CERN Large Hadron Collider*, *JINST* **3** (2008), no. 08 S08003.

[4] **CMS** Collaboration, *The CMS experiment at the CERN LHC*, *JINST* **3** (2008), no. 08 S08004.

[5] **LHCb** Collaboration, *The LHCb Detector at the LHC*, *JINST* **3** (2008), no. 08 S08005.

[6] **ALICE** Collaboration, *The ALICE experiment at the CERN LHC*, *JINST* **3** (2008), no. 08 S08002.

[7] G. Aad et al., *ATLAS pixel detector electronics and sensors*, *JINST* **3** (2008), no. 07 P07007.

[8] **ATLAS** Collaboration, *ATLAS inner detector : Technical Design Report, 1*, Tech. Rep. CERN-LHCC-97-016, CERN, 1997.

[9] **ATLAS** Collaboration, *ATLAS inner detector : Technical Design Report 2*, Tech. Rep. CERN-LHCC-97-017, CERN, 1997.

[10] **ATLAS** Collaboration, *ATLAS pixel detector: Technical Design Report*, Tech. Rep. CERN-LHCC-98-013, CERN, 1998.

[11] A. Abdesselam et al., *The ATLAS semiconductor tracker end-cap module*, *Nucl. Instrum. and Meth.* **A575** (2007), no. 3 353–389.

[12] A. Abdesselam et al., *The barrel modules of the ATLAS semiconductor tracker*, *Nucl. Instrum. and Meth.* **A568** (2006), no. 2 642–671.

[13] **ATLAS** Collaboration, *The ATLAS Transition Radiation Tracker (TRT) proportional drift tube: design and performance*, *JINST* **3** (2008), no. 02 P02013.

[14] **ATLAS** Collaboration, *ATLAS liquid-argon calorimeter : Technical Design Report*, Tech. Rep. CERN-LHCC-96-041, CERN, 1996.

[15] **ATLAS** Collaboration, *ATLAS tile calorimeter : Technical Design Report*, Tech. Rep. CERN-LHCC-96-042, CERN, 1996.

[16] **ATLAS** Collaboration, *ATLAS muon spectrometer : Technical Design Report*, Tech. Rep. CERN-LHCC-97-022, CERN, 1997.

[17] C. Padilla, *The ATLAS Trigger System*, *IEEE Trans. Nucl. Sci.* **57** (April, 2010) 650 –657.

[18] C. Gabaldon, *Performance of the ATLAS Trigger System*, *JINST* **7** (2012), no. 01 C01092.

[19] "The High Luminosity Large Hadron Collider Official Website." http://hilumilhc.web.cern.ch/HiLumiLHC/about/, 2012.

[20] M. Capeans, G. Darbo, K. Einsweiller, M. Elsing, T. Flick, M. Garcia-Sciveres, C. Gemme, H. Pernegger, O. Rohne, and R. Vuillermet, *ATLAS Insertable B-Layer Technical Design Report*, Tech. Rep. CERN-LHCC-2010-013, CERN, Geneva, 2010.

[21] P. Miyagawa, "Simulating LHC Fluence for the ATLAS Inner Detector." Slides for Second Inter-Experiment on Radiation Damage in Silicon Detectors at CERN, 2012.

[22] C. Buttar and D. della Volpe, "Letter of Intent for the Phase II Upgrade." https://twiki.cern.ch/twiki/bin/viewauth/Atlas/UpgradeLOIPhase2, 2012.

[23] L. Rossi and R. De Maria, *Summary of Session 8 High Luminosity (HL-LHC)*, in *Proceedings of the Chamonix 2011 workshop on LHC Performance*, pp. 28–30, 2011.

[24] F. Hügging, *The atlas pixel insertable b-layer (ibl)*, *Nuclear Instruments and Methods in Physics Research Section A: Accelerators, Spectrometers, Detectors and Associated Equipment* **650** (2011), no. 1 45–49.

[25] F. Hügging, *Der ATLAS Pixelsensor- Der state-of-the-art Pixelsensor für Teilchenphysikalische Anwendung mit extern hohen Strahlungsfelden*. Universität Dortmund PhD Thesis, Dortmund, Germany, 2001.

[26] J. Koike, D. M. Parkin, and T. E. Mitchell, *Displacement threshold energy for type IIa diamond*, *Applied Physics Letters* **60** (1992), no. 12 1450 –1452.

[27] V. A. J. Van Lint, T. M. Flanagan, R. E. Leadon, J. A. Naber, and V. C. Rogers, *Mechanisms of Radiation Effects in Electronic Materials*. Wiley, New York, 1 ed., 1980.

[28] R. C. Alig, S. Bloom, and C. W. Struck, *Scattering by ionization and phonon emission in semiconductors*, *Phys. Rev. B* **22** (Dec, 1980) 5565–5582.

[29] R. C. Alig, *Scattering by ionization and phonon emission in semiconductors. ii. monte carlo calculations*, *Phys. Rev. B* **27** (Jan, 1983) 968–977.

[30] K. N. et al. (Particle Data Group), *Review of particle physics: Passage of particles through matter*, *J. Phys. G: Nucl. Part. Phys.* **37** (2010) 4.

[31] H. Pernegger et al., *Charge-carrier properties in synthetic single-crystal diamond measured with the transient-current technique* , *J. Appl. Phys.* **97** (2005) 073704–1.

[32] J. Isberg et al., *High Carrier Mobility in Single-Crystal Plasma-Deposited Diamond*, *Science* **297** (2002), no. 5587 1670–1672.

[33] S. M. Sze, *Semiconductor Device Physics and Technology*. John Wiley and Sons, Singapore, 1 ed., 1985.

[34] C. Jacoboni, C. Canali, G. Ottaviani, and A. A. Quaranta, *A review of some charge transport properties of silicon*, *Solid-State Electronics* **20** (1977), no. 2 77–89.

[35] M. Barbero, D. Arutinov, R. Beccherle, G. Darbo, R. Ely, et al., *A new ATLAS pixel front-end IC for upgraded LHC luminosity*, *Nucl. Instrum. and Meth.* **A604** (2009) 397–399.

[36] M. Garcia-Sciveres, D. Arutinov, M. Barbero, R. Beccherle, S. Dube, et al., *The FE-I4 pixel readout integrated circuit*, *Nucl. Instrum. and Meth.* **A636** (2011) S155–S159.

[37] M. Karagounis, *Analog Integrated CMOS Circuits for the Readout and Powering of Highly Segmented Detectors in Particle Physics Applications*. Fernuniversität Hagen PhD Thesis, Hagen, Germany, 2010.

[38] F. Hügging, "Variation of the Injection Capacitance of FE-I4 Measured during Wafer Test." Private Commission, 2012.

[39] J. Wolf, G. Chmiel, and H. Reichl, *Lead/Tin (95/5%) solder bumps for flip chip applications based on Ti:W(N)/Au/Cu underbump metallization* , in *Proceedings of 5th Intl. TAB/Advanced Packaging Symposium ITAP, San Jose, USA*, pp. 141–152, 1993.

[40] J. Wolf, *Solder bumping by electroplating*, in *Pixel 2000 Conference, Genova, Italy*, 2000.

[41] M. Werner and R. Locher, *Growth and application of undoped and doped diamond films*, *Reports on Progress in Physics* **61** (1998), no. 12 1665.

[42] M. Mathes, *Development and Characterization of Diamond and 3D-Silicon Pixel Detectors with ATLAS Pixel Readout Electronics*. Universität Bonn PhD Thesis, Bonn, Germany, 2008.

[43] **RD42** Collaboration, D. Asner et al., *Diamond pixel modules*, *Nucl. Instrum. and Meth.* **A636** (2011) S125–S129.

[44] A. Dierlamm, "Irradiations in karlsruhe." Slides for the 16th RD50 workshop, 2010.

[45] R. Firestone1 and L. Ekström, " WWW Table of Radioactive Isotopes : LBNL Isotopes Project - LUNDS Universitet." http://ie.lbl.gov/toi/, 2004.

[46] H. H. Anderson et al., "ESTAR, Stopping Power and Range Tables for Electrons." http://physics.nist.gov/PhysRefData/Star/Text/ESTAR.html.

[47] M. Marinelli, E. Milani, M. E. Morgada, G. Pucella, G. Rodriguez, A. Tucciarone, G. Verona-Rinati, M. Angelone, and M. Pillon, *Thermal detrapping analysis of pumping-related defects in diamond*, *Applied Physics Letters* **83** (2003) 3707.

[48] H. Bethe, *Zur theorie des durchgangs schneller korpuskularstrahlen durch materie*, *Annalen der Physik* **397** (1930), no. 3 325–400.

[49] R. M. Sternheimer, *General expression for the density effect for the ionization loss of charged particles*, *Phys. Rev. B* **24** (1981) 6288–6291.

[50] R. M. Sternheimer, S. M. Seltzer, and M. Berger, *The density effect for the ionization loss of charged particles in various substances*, *Atomic Data and Nuclear Data Tables* **30** (1984) 261.

[51] M. Mathes, M. Cristinziani, H. Kagan, S. Smith, W. Trischuk, J. Velthuis, and N. Wermes, *Characterization of a single crystal diamond pixel detector in a high energy particle beam*, *JINST* **3** (2008), no. 12 P12002.

[52] J. Bak, A. Burenkov, J. Petersen, E. Uggerhøj, S. Møller, and P. Siffert, *Large departures from landau distributions for high-energy particles traversing thin si and ge targets*, *Nuclear Physics B* **288** (1987), no. 0 681–716.

[53] A. Landau, *On the energy loss of fast particles by ionization*, *J. Phys. (USSR)* **8** (1944) 201.

[54] H. Bichsel, *Straggling in thin silicon detectors*, *Rev. Mod. Phys.* **60** (07, 1988) 663–699.

[55] E. Cohen and B. Taylor, *The 1986 adjustment of the fundamental physical constants*, *Physics Today* **BG7-BG11** (1997) 1121–1148.

[56] M. Berger, J. Hubbell, S. Seltzer, J. Chang, J. Coursey, R. Sukumar, D. Zucker, and K. Olsen, "XCOM: Photon Cross Sections Database." http://www.nist.gov/pml/data/xcom/index.cfm.

[57] G. Lindström, *Radiation damage in silicon detectors*, *Nucl. Instrum. and Meth.* **A512** (2003), no. 1-2 30–43.

[58] V. van Lint, T. Flanagan, R. Leadon, J. Naber, and V. Rogers, *Mechenism of Radiation Effects in Electronic Materials*. John Wiley and Sons, 1 ed., 1980.

[59] R. Wunstorf, *Systematische Untersuchung zur Stahlungresistenz von Si-Detectoren für die Vervendung von HEP-Experimenten*. Universität Dortmund PhD Thesis, Dortmund, Germany, 1992.

[60] M. Moll, *Radiation Damage in Silicon Particle detectors*. Universität Hamburg PhD Thesis, 1999.

[61] S. Zhao, *Characterization of the Electrical Properties of Polycrystalline Diamond Films*. The Ohio State University PhD Thesis, Columbus, Ohio, U.S.A, 1994.

[62] **ROSE** Collaboration, A. Vasilescu and G. Lindström, *Notes on the fluence normalisation based on the NIEL scaling hypothesis*, Tech. Rep. ROSE/TN/2000-02, CERN, 2000.

[63] J. Lindhard, V. Nielsen, M. Scharff, and P. Thomsen, *Integral equations governing radiation effects*, *Kongelige Danske Videnskabernes Selskab, Matematisk-Fysiske Meddelelser* **33** (1963) 1–42.

[64] American Society for Testing and Materials, “Astm e722-93.” " Standard practice for characterizing neutron fluence spectra in terms of an equivalent monoenergetic neutron fluence for radiation hardness testing of electronics", 1993.

[65] R. Rossi, P. Fisher, T. Rohe, and N. Wermes, *Pixel Detectors: From fundamentals to Applications*. Springer, 1 ed., 2006.

[66] M. Moll, E. Fretwurst, and G. Lindström, *Leakage current of hadron irradiated silicon detectors - material dependence*, *Nucl. Instrum. and Meth.* **A426** (1999), no. 1 87–93.

[67] M. Huhtinen, *Simulation of non-ionising energy loss and defect formation in silicon*, *Nucl. Instrum. and Meth.* **A491** (2002), no. 1-2 194 – 215.

[68] A. Ruzin, G. Casse, M. Glaser, F. Lemeilleur, J. Matheson, S. Watts, and A. Zanet, *Radiation effects in silicon detectors processed on carbon and oxygen-rich substrates*, *Materials Science in Semiconductor Processing* **3** (2000), no. 4 257–261.

[69] S. M. Sze, *Physics of Semiconductor Device*. Wiley Interscience, New York, 1 ed., 1969.

[70] S. Ramo, *Currents induced by electron motion*, *Proceedings of the IR* **27** (1939), no. 9 584–585.

[71] S. Müller, *The Beam Condition Monitor 2 and the Radiation Environment of the CMS Detector at the LHC*. Universität Karlsruhe, Karlsruhe, Germany, 2011.

[72] R. Sussmann et al., *CVD Diamond for Electronic Devices and Sensors*. " John Wiley and Sons ", Chichester, United Kingdom, 1 ed., 2009.

[73] T. Taniguchi, Y. Fukushima, and Y. Yoribayashi, *New electronics system for silicon strip readout for 18 kev electrons*, *IEEE Trans. Nucl. Sci.* **36** (1989) 657–661.

[74] **CLEO Collaboration** Collaboration, Y. Kubota et al., *The CLEO-II detector*, *Nucl. Instrum. and Meth.* **A320** (1992) 66–113.

[75] **RD42 Collaboration** Collaboration, D. Asner et al., *Diamond pixel modules*, *Nucl. Instrum. and Meth.* **A636** (2011) S125–S129.

[76] G. Casse, A. Affolder, P. Allport, H. Brown, and M. Wormald, *Enhanced efficiency of segmented silicon detectors of different thicknesses after proton irradiations up to 1* $\times$ 10^{16} n_{eq}/cm^2, *Nucl. Instrum. and Meth.* **A624** (2010) 401–404.

[77] A. Affolder, P. Allport, and G. Casse, *Charge collection efficiency measurements of heavily irradiated segmented n-in-p and p-in-n silicon detectors for use at the super-LHC*, *IEEE Trans. Nucl. Sci.* **56** (2009) 765–770.

[78] S. Tedja, J. V. der Spiegel, and H. Williams, *Analytical and experimental studies of thermal noise in mosfets*, *IEEE Trans. on Electron Devices* **41** (1994) 2069 – 2075.

[79] G. Anelli, M. Campbell, M. Delmastro, F. Faccio, S. Floria, A. Giraldo, E. Heijne, P. Jarron, K. Kloukinas, A. Marchioro, P. Moreira, and W. Snoeys, *Radiation tolerant vlsi circuits in standard deep submicron cmos technologies for the lhc experiments: practical design aspects*, *IEEE Trans. Nucl. Sci.* **46** (dec., 1999) 1690 –1696.

[80] R. J. Baker, *CMOS: Circuit Design, Layout, and Simulation*. Wiley-IEEE Press, New York, 3 ed., 2010.

[81] P. O'Connor and G. De Geronimo, *Prospects for charge sensitive amplifiers in scaled cmos*, in *Conference Record of the IEEE Nuclear Science Symposium*, vol. 1, pp. 88–93, 1999.

[82] K. C. A. Smith and R. E. Alley, *Electrical Circuits: An Introduction*. Cambridge University Press, Cambridge, United Kingdom, 1 ed., 1992.

[83] Virtuoso Spectre Circuit Simulator. http://www.cadence.com/products/rf/spectre_circuit/pages/default.aspx.

[84] M. Harvanek et al., "Pixcap Chip." to be submitted to Nucl. Instrum. Meth., 2012.

[85] P. Weigell, M. Beimforde, C. Gallrapp, A. L. Rosa, A. Macchiolo, R. Nisius, H. Pernegger, and R. H. Richter, *Characterization and performance of silicon n-in-p pixel detectors for the atlas upgrades*, *Nucl. Instrum. and Meth.* **A658** (2011), no. 1 36–40.

Acknowledgements

《 消音 - 過高屏溪 》　陳雋弘

鐵塔漸漸消失了
霧以其温柔的手指
輕輕
將世界消音

搭乘普通號列車南下
有著優美弧度的
高壓電纜漂浮如軌道
我們正行駛於其中一條

灰暗已經過去，剛剛下了一場雨
綠色的
座椅猶不斷向前延伸
我們也加入了
水面上暴漲的布袋蓮行列

窗外飛鳥，陸續
將沿途風景都叼走了
我們因為小睡
完全沒有察覺

This thesis would not be completed without the support and guidance from many people. I would like to use this opportunity to express my gratitude to all of the people whom I was able to work with. Special thanks to:

- Prof. Norbert Wermes for giving me the chance to work on this thesis, and for his patient guidance, fruitful discussions about the science and methods of research.
- Prof. Harris Kagan for the knowledge and experiences on diamond, and beside the works, showing me how to enjoy and explore the life with full heart.
- Dr. Fabian Hüugging for technical supports, and prove-reading this thesis.
- All of my colleagues in Silab and at CERN for technical supports and discussions.
- Feng-i Tai, Veronika Chuang, Terri He, Tai-Hsiang Ho for psychological therapies.
- My parents for unconditional help and regards.

This thesis is dedicated to Chang-Hung Lee. Without his encouragement and acceptance, I would not have the strength to finish this work.